

Dipl.-Ing. Peter Parz

Vacancy-type and interface related defects in ultra fine grained alloys and oxides

DOCTORAL THESIS

For obtaining the academic degree of
Doktor der technischen Wissenschaften

Doctoral Programme of Technical Sciences
Technical Physics



Graz University of Technology

Supervisor:

Ao. Univ.-Prof. Dipl.-Ing. Dr.techn. Werner Puff
Institute of Materials Physics

Graz, April 2013

Deutsche Fassung:
Beschluss der Curricula-Kommission für Bachelor-, Master- und Diplomstudien vom 10.11.2008
Genehmigung des Senates am 1.12.2008

EIDESSTÄTTLICHE ERKLÄRUNG

Ich erkläre an Eides statt, dass ich die vorliegende Arbeit selbstständig verfasst, andere als die angegebenen Quellen/Hilfsmittel nicht benutzt, und die den benutzten Quellen wörtlich und inhaltlich entnommenen Stellen als solche kenntlich gemacht habe.

Graz, am

.....
(Unterschrift)

Englische Fassung:

STATUTORY DECLARATION

I declare that I have authored this thesis independently, that I have not used other than the declared sources / resources, and that I have explicitly marked all material which has been quoted either literally or by content from the used sources.

.....
date

.....
(signature)

Abstract

Atomic free volume is a key parameter in various materials, influencing the structural and mechanical properties. To investigate these open volumes, the sensitive methods of positron annihilation lifetime spectroscopy and Doppler broadening spectroscopy were utilised. These methods allow determining types, concentrations and the chemical environment of the open volume defects of the atomic structure.

Iron samples with different purity and an aluminium-copper alloy were deformed by means of high pressure torsion to investigate the defect formation, annealing behaviour and the role of defects on precipitation phenomena. While in pure samples the formation of vacancy-clusters is observed, alloying components lead to the formation of vacancy-impurity complexes. A significant change in the precipitation process on an aluminium-copper alloy could be determined as well. As open volumes are not only relevant in metals and alloys, oxide materials were investigated as well. Due to the increased demand on portable energy storage materials, electrodes for lithium-ion batteries were chosen. Secondary lithium-ion battery cathode materials, LiCoO_2 , LiMn_2O_4 and $\text{LiNi}_{1/3}\text{Mn}_{1/3}\text{Co}_{1/3}\text{O}_2$ at different lithium-ion contents were investigated. For all the investigated cathode materials a lithium-vacancy ordering process could be observed. The direct observations of these ordering processes give hints on the structural stability of the materials and improve the understanding of the lithium-ion extraction process. The results clearly reveal that positron annihilation methods are capable to investigate this kind of materials and opens up a new approach to investigate degradation mechanisms, reducing the lifetime of lithium-ion batteries.

Contents

Abstract	v
1 Introduction	1
2 Basics	5
2.1 State of research	5
2.1.1 Nanocrystalline metals	5
2.1.2 Lithium-ion battery electrodes	7
2.2 Positron annihilation in condensed matter	8
3 Methods & Materials	13
3.1 Methods	13
3.1.1 Positron annihilation lifetime spectroscopy	13
3.1.2 Positron annihilation Doppler broadening spectroscopy	16
3.2 Materials preparation	22
3.2.1 Nanostructured metals and alloys by high pressure torsion	22
3.2.2 Electrochemical defect introduction in functional oxides	23
4 Results and Discussion	29
4.1 Open volume defects in nanoscale alloys	29
4.1.1 Iron	30
4.1.2 Al-3wt%Cu	44
4.1.3 Iron-Nickel meteorite	68
4.1.4 Discussion	79

4.2	Open volume defects in oxides	81
4.2.1	Sample preparation	81
4.2.2	LiCoO ₂	82
4.2.3	LiMn ₂ O ₄	93
4.2.4	Li(Co _{1/3} Mn _{1/3} Ni _{1/3})O ₂	98
4.2.5	Comparison and Summary	103
5	Summary and Conclusion	107
	Bibliography	111

CHAPTER 1

Introduction

Atomic defects are known to significantly modify materials characteristics. Vacancy concentrations, dislocation densities and grain boundaries have significant influence on macroscopic materials properties, such as, for example, hardness, electrical resistivity, ductility and optical properties. Therefore, the investigation of these defects and how they influence the materials characteristics are of fundamental interest in materials research. In consequence of the basic understanding, materials properties may be tuned by defect introduction.

Various ways to investigate open volumes and their annealing characteristics, such as differential scanning calorimetry [1–3], differential dilatometry [4, 5], transmission electron microscopy [6–8] and positron annihilation lifetime spectroscopy [9–11] exist. All of the afore mentioned methods give insight into the defect annealing characteristics, but the chemical environment of open volumes can not be investigated by these methods. Only positron annihilation Doppler broadening spectroscopy is capable to distinguish the chemical environment of open volume defects [9, 12, 13]. This method can give additional insights into the effect of alloying components to defect stability.

Over the last decade, bulk nanocrystalline materials have drawn increasing attention, due to their improved material properties and the associated potential for applications. High pressure torsion (HPT) exhibits an excellent route to produce bulk nanostructured metals. Due to the continued severe plastic deformation very high strains may be introduced and lead to a fine grained microstructure, free of pores and cracks. In general, nanocrystalline materials are characterised by a high concentration of atomic defects. These atomic defects, such as vacancies, dislocations and grain boundaries, exhibit an additional free volume compared to the perfect crystalline structure.

In this work, open volume defects in metals and alloys introduced by high pressure torsion and precipitation phenomena were investigated. In the first part, the effects of sample purity on the defect generation by HPT and their annealing characteristics were explored on iron samples. Further on, the effect of HPT deformation on the precipitation processes on an Al-Cu alloy was examined. In the last section of the first part, defects in an iron-nickel meteorite in perfect thermal equilibrium were explored.

As there is a fast growing demand for high efficient, lightweight and durable energy storages, increased research interest in lithium-ion battery systems has evolved. With X-ray [14–16] and neutron diffraction [17, 18] studies, the structural stability of electrode materials for battery application are investigated upon lithium extraction. Detailed atomistic changes can not be determined from these measurements. Therefore, in the second part of this work, the electrochemical removal of lithium and the connected defect introduction on structural and electrical properties of functional oxides, were studied by the atomistic sensitive method of positron lifetime spectroscopy and Doppler broadening spectroscopy.

This work was realised in cooperation with:

- The Erich Schmid Institute of Materials Science, Austrian Academia of Sciences, Leoben, Austria.
- VARTA Micro Innovations GmbH, Graz, Austria.

At the following conferences presentations of parts of this thesis in the form of talks and posters were given:

- Frühjahrestagung der Deutschen Physikalischen Gesellschaft 2011, Berlin (oral presentation)
- Positron Studies of Defects - 11, 2011, Delft (oral presentation)
- International Conference on Positron Annihilation 16, 2012, Bristol (oral and poster presentation)
- Jahrestagung der Österreichischen Physikalischen Gesellschaft 2012, Graz (oral and poster presentation)

Parts of this thesis have already been published in or submitted to the following journals:

- P. Parz, M.J. Faller, R. Pippan, W. Puff, and R. Würschum, *Defects in Al-3wt%Cu after high-pressure torsion studied by two-dimensional Doppler broadening spectroscopy*, Physics Procedia 35, 10-15, (2012)
- P. Parz, M.J. Faller, R. Pippan, H. Reingruber, W. Puff, and R. Würschum, *Microstructure and vacancy-type defects of high-pressure torsion deformed Al-3wt%Cu alloy*, Journal of Applied Physics 112, 103506, (2012)
- P. Parz, M. Leitner, W. Sprengel, H. Reingruber, and W. Puff, *Defect investigations of an iron-nickel meteorite*, Physics Procedia, accepted (February 2013)
- W. Puff, X. Zhou, B. Oberdorfer, B. Scherwitzl, P. Parz, W. Sprengel, and R. Würschum, *Comprehensive defect characterization of different iron samples after severe plastic deformation*, Physics Procedia, accepted (February 2013)
- P. Parz, B. Fuchsbichler, S. Koller, B. Bitschnau, F.A. Mautner, W. Puff, and R. Würschum, *Charging-induced defect formation in Li_xCoO_2 battery cathodes studied by positron annihilation spectroscopy*, Applied Physics Letters 102, 151901, (2013)

CHAPTER 2

Basics

2.1 State of research

In this section a brief review on the state of research is given, concerning nanocrystalline materials produced by high-pressure torsion (HPT) and Lithium-ion battery electrodes.

2.1.1 Nanocrystalline metals

In the last decades, interest in bulk nanostructured materials increased, due to their extraordinary properties. It is, therefore, absolutely essential to understand the basic mechanisms, leading to these unique properties. Various investigation methods have been applied to increase the basic understanding of the deformation processes leading to bulk nanostructured materials.

Free volumes and defect concentrations are investigated by means of differential dilatometry [4, 5], differential scanning calorimetry [1–3] and electron microscopy [6–8]. These methods are applied to deduce the defect concentrations, migration enthalpies, grain boundary excess volumes and the thermal stability of the nano-structures.

Differential dilatometry, already used by Simmons and Baluffi in the 1960s [19], exhibits

an elegant way to determine open volumes. By comparing the relative change of lattice parameter a (determined from X-ray diffraction) upon temperature treatment to the relative length change of the sample the formation of vacancies and their additional volume can be determined. The vacancy concentration for cubic crystals can be determined by $C_V = 3 \times (\frac{\Delta l}{l} - \frac{\Delta a}{a})$, assuming an isotropic distribution of vacancy sources and sinks. Recently, time dependent dilatometry has been imposed to investigate the defect annealing and defect kinetics [4]. The irreversible length change of HPT deformed samples upon linear heating, by simultaneous measurement of the thermal expansion of a reference sample, enables the determination of all free volume associated defects. Kinetics can be studied by varying the thermal heating rate and the grain boundary excess volume can be determined [4, 5].

Differential scanning calorimetry [1–3], electrical resistivity measurements [2], X-ray line profile analysis [20, 21] are used to determine the concentration and nature of vacancy-type defects in nanometals obtained by severe plastic deformation. Dislocation densities and activation enthalpies for migration were obtained for different metals [2].

Positron annihilation lifetime spectroscopy is used since the 1980s, when Schaefer et al. [22] investigated nano-crystalline iron. Positrons, trapped at open volume defects, give a comprehensive picture on grain boundaries, vacancy concentrations and the existence of different defect types present within the sample [23]. Since then, various studies on structural open volumes have been performed on nanocrystalline metals produced by inert gas condensation [24], ball milling [25, 26] and severe plastic deformation [9, 11, 27–31]. Different groups investigated the types and annealing characteristic of open volumes introduced by severe plastic deformation on pure metals such as copper [11, 27], nickel [28–30] or iron [31].

In aluminium alloys the effects of precipitate fragmentation upon severe plastic deformation were investigated by means of electron microscopy [7, 32] and positron annihilation Doppler broadening spectroscopy [9]. Doppler broadening spectroscopy, in contrast to all other methods mentioned, is capable to identify the chemical environment of open volume defects. This gives additional insights into the effects of alloying components on defect formation, stabilisation and annealing.

2.1.2 Lithium-ion battery electrodes

Since the development of lithium-ion secondary batteries, several investigations on the effect of Li^+ -extraction onto the electrode materials have been performed. Electrochemical characterisation, as well as ex-situ and in-situ structural investigations with X-ray diffraction have been performed [14–16]. These experiments give insights into the structural stability of the compounds upon Li^+ -extraction. The results found by XRD were confirmed by neutron diffraction studies as well [17, 18].

Transmission electron microscopy [33, 34], scanning electron microscopy [35] and high resolution transmission electron microscopy [36] have also been utilised to investigate this kind of materials. Theoretical studies on the phase diagram, to determine the stability of the structures have been performed as well [37, 38]. Electrical resistivity measurements [39, 40] in LiCoO_2 revealed a variation of the conductivity with Li^+ -content of several orders of magnitude, including an insulator-metallic conductor transition. Diffusion of Li^+ within the electrode is strongly affecting the power density. Therefore, experimental [41, 42] and theoretical [43] investigations on Li^+ -diffusion in lithium-ion battery cathodes have been performed. Different Li^+ -diffusion pathways are considered, but experimental validation is missing.

In order to circumvent phase instabilities and to obtain beneficial properties, different ways to produce composite electrodes have been examined. Coating of the active particles [44–46] or partly substituting Co^{3+} by other transition metals [47, 48], as e.g. Ni or Mn, are currently investigated.

In spite of the research activities in the last two decades, an atomistic approach to understand degradation mechanisms is still lacking. The application of positron annihilation techniques may give additional insights into the atomistic processes, leading to cathode degradation and, therefore, open up new ways to overcome the constraints on Li^+ -extraction and cyclability.

Positron annihilation studies on lithium-ion electrode materials have, until now, not been performed.

2.2 Positron annihilation in condensed matter

A specific method to investigate condensed matter on an atomistic scale is positron annihilation spectroscopy. A positron injected into a solid annihilates with an electron. By measurement and analysis of the positron annihilation characteristics, a detailed picture of the local electron densities and the electron momenta can be obtained. A brief review of the basic principles of positron annihilation will be presented here.

In the 1960's a strong correlation between positron lifetime and temperature was found by McKenzie [49]. Positrons may, therefore, be used as mobile probe to investigate atomic free volumes in solids. Energetic positrons from a radioactive source, which are injected into condensed matter, slow down to thermal energies within a few picoseconds [50]. The kinetic energy is at first dissipated by plasmon excitation and ionisation collisions. Further dissipation occurs by creation of electron–hole–pairs and diffraction at phonons [51, 52]. The thermalisation of the continuous energy-spectrum of β^+ -decay can be macroscopically described by an exponential law [53]. Positrons thermalise with the probability given by:

$$\delta P = \alpha e^{-\alpha x} \delta x \quad (2.1)$$

within the interval $x + \delta x$. For the linear absorption coefficient α a good approximation in condensed matter is [53]:

$$\alpha \approx 17 \frac{\rho}{E_{max}^{1.43}} \quad (2.2)$$

with ρ the sample density in g cm^{-3} and E_{max} the maximum kinetic energy of the positrons in MeV. In thermal equilibrium, the positron diffuses through the crystal and it could be shown [52] that the mean diffusion length is given by:

$$L \approx \sqrt{6D_+ \bar{\tau}} \quad (2.3)$$

with the diffusion coefficient D_+ and $\bar{\tau}$ the mean positron lifetime. With typical lifetimes in the range of 100 to 300 ps in metals and semiconductors, positrons sense a volume of about 10^9 atoms. After living in thermal equilibrium, the positron annihilates with an electron from the surrounding. The dominant emission of two 511 keV γ -rays follows the conservation of energy by Einsteins $E = m_0 c^2$, with m_0 the rest mass of an electron or positron and the speed of light c . One and three γ -quanta decays

have only diminishing probabilities and can, therefore, be neglected [54].

The positron annihilation rate λ is determined by the overlap of the electron and positron densities. In the case of a perfect lattice, the positron may be characterised by an extended quantum-mechanical wave function. The positron–electron pair correlation has to be taken into account by an enhancement factor $\gamma(n_-)$, leading to the annihilation rate

$$\lambda = \pi r_0^2 c \int n_+(r)n_-(r)\gamma(n_-)dr \quad (2.4)$$

where $n_-(r)$ and $n_+(r)$ describe the electron and positron density functions, with c the speed of light and r_0 the classical electron radius. Utilising the Sommerfeld model of free electron gas and neglecting the enhancement function $\gamma(n_-)$ leads to:

$$\lambda_{so} = \pi r_0^2 cn. \quad (2.5)$$

Obviously, the positron annihilation rate is direct proportional to the electron density n . The inverse of the positron annihilation rate λ is the positron lifetime τ . When positrons annihilate in a perfect crystal the positron lifetime τ corresponds to the so called bulk lifetime, which is a characteristic material constant. This bulk lifetime varies between 100 and 165 ps [55, 56] for most metals and from 200 to 280 ps [57] for elemental and many compound semiconductors.

Upon diffusion through the crystal the positron may annihilate from the free state or be trapped at crystal defects. Crystal defects, such as vacancies, dislocations, grain boundaries, voids or pores exhibit additional free volumes in the crystal. By the absence of positively charged atomic cores, these free volumes exhibit lower energy levels and act as attractive sites for positrons. These free volumes do not only lack the ionic core of an atom, but as well lack the electronic shell and, therefore, exhibit a decreased electron density at the annihilation site. As positron annihilation is correlated to the electron density (see eq. 2.4), positrons trapped at open volumes show an increase in their lifetime.

The positron trapping at defects can be easily described in the framework of a transition rate theory [58, 59], by the trapping rate κ , which can be given as

$$\kappa = \mu C_{trap} \quad (2.6)$$

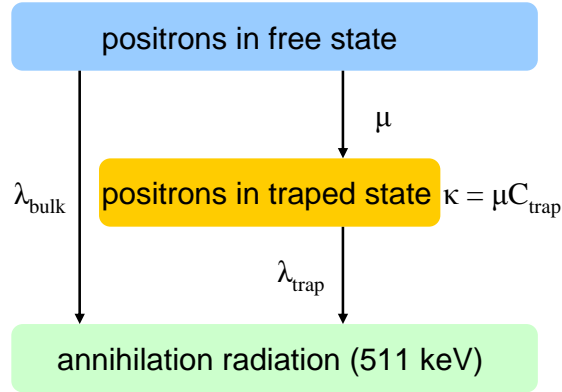


Figure 2.1: Sketch of the simple trapping model, with the trapping rate κ , the specific trapping rate μ , the defect concentration C_{trap} and the annihilation rates λ_{bulk} and λ_{trap} of the free and trapped state, respectively.

with μ the specific trapping coefficient and the positron trap concentration C_{trap} .

In the case of a single type of defect (see Figure 2.1), the temporal evolution of the number of free positrons within the sample can be given by:

$$\frac{dn_b(t)}{dt} = -\lambda_b n_b(t) - \mu C_{trap} n_b(t) \quad (2.7)$$

$$\frac{dn_d(t)}{dt} = -\lambda_d n_d(t) + \mu C_{trap} n_b(t). \quad (2.8)$$

with n_b and n_d the amount of positrons in the free state and trapped in the defect state, respectively. Solving this system of coupled differential equations, with the basic condition that at $t = 0$ all positrons are within the free state, leads to the following term:

$$n(t) = n_b + n_d = I_1 e^{-\lambda_1 t} + I_d e^{-\lambda_d t} \quad (2.9)$$

with the relative intensities I of the positron lifetime component and the annihilation rates λ , with the substitution $\lambda_1 = \lambda_b + \mu C_{trap}$. In an experiment the total annihilation probability is measured and is given by:

$$P(t) = -\frac{dn}{dt} = I_1 \lambda_1 e^{-\lambda_1 t} + I_d \lambda_d e^{-\lambda_d t} \quad (2.10)$$

As can be seen from eq. 2.10, the positron lifetime spectrum is composed of two exponential decays, with the positron lifetimes τ_1 and τ_d given by the inverse of the

corresponding annihilation rate λ_1 and λ_d . The positron lifetime in the bulk material can be calculated from the measured parameters by:

$$\tau_b = \frac{1}{\lambda_b} = \frac{1}{I_1\lambda_1} + \frac{1}{I_d\lambda_d}. \quad (2.11)$$

While the measured positron lifetime τ_1 is called the reduced bulk lifetime, the measured lifetime component τ_d is the positron lifetime in the open volume defect. The lifetimes τ_1 , τ_d and their corresponding intensities I_1 and I_d can be obtained from numerical analysis of the measured spectra. From these parameters, the trapping rate κ may be calculated by:

$$\kappa = \mu C_{trap} = I_2 \left(\frac{1}{\tau_1} - \frac{1}{\tau_d} \right). \quad (2.12)$$

The specific trapping coefficients μ are available from quantum-mechanical calculations and from the comparison of the trapping rate μC_{trap} with the defect concentrations obtained from complementary techniques. Specific trapping coefficients μ for single atom vacancies in metals are in the range of 10^{14} s^{-1} to 10^{15} s^{-1} [60, 61]. These values are about 5 orders of magnitude larger than the typical annihilation rate in defect free metals ($\lambda_{free} = 5 \times 10^9 \text{ s}^{-1}$ [52]). Therefore, defect concentrations in the range of 10^{-7} to 10^{-4} can be resolved [23]. The upper limit is given by saturation trapping, which means each positron is trapped at a defect. An important measure obtained by positron lifetime spectroscopy is the mean positron lifetime. From this stable parameter relative changes in defect concentrations can be determined. The mean positron lifetime $\bar{\tau}$ is given by:

$$\bar{\tau} = \int_0^{\infty} P(t) dt \quad (2.13)$$

$$\bar{\tau} = \frac{I_1}{\lambda_1} + \frac{I_d}{\lambda_d} = I_1\tau_1 + I_d\tau_d = \tau_f \times \frac{1 + \kappa\tau_d}{1 + \kappa\tau_f}. \quad (2.14)$$

To describe positron trapping at grain boundaries, the limitation of positron trapping at grain boundaries, due to diffusion has to be taken into account. Recently an exact solution of the diffusion-reaction theory of positron trapping at grain boundaries and competitive trapping at intergranular point defects was presented by Oberdorfer [62]. The mean positron lifetime is given by:

$$\bar{\tau} = \frac{\frac{3\alpha}{r_0} \gamma_0 DL(\gamma_0 r_0) [\tau_b (\tau_f^{-1} + \sigma_v C_v) - (1 + \sigma_v C_v \tau_v)] + [\alpha + \gamma_0 DL(\gamma_0 r_0)] (\tau_f^{-1} + \sigma_v C_v) (1 + \sigma_v C_v \tau_v)}{[\alpha + \gamma_0 DL(\gamma_0 r_0)] (\tau_f^{-1} + \sigma_v C_v)^2} \quad (2.15)$$

with the specific trapping rate at grain boundaries α , the spherical grain radius r_0 , the Langevin function $L(\gamma_0 r_0)$ and

$$\gamma^2 = \frac{\tau_f^{-1} + \sigma_v C_v}{D}. \quad (2.16)$$

The solution of the diffusion-reaction model for positron trapping in grain boundaries and the simple trapping model for two types of traps are special cases of the solution presented in equation 2.15. For nanocrystalline metallic samples, the complete reaction controlled trapping model may be applied [63], leading to the following equation:

$$\bar{\tau} = \tau_b \frac{1 + 3\alpha r_0^{-1} \tau_{gb}}{1 + 3\alpha r_0^{-1} \tau_b} \quad (2.17)$$

which leads to a κ of

$$\kappa = \frac{3\alpha}{r_0}. \quad (2.18)$$

CHAPTER 3

Methods & Materials

In this section, a short review on the investigation methods and the investigated materials is given.

3.1 Methods

3.1.1 Positron annihilation lifetime spectroscopy

For the experimental measurement of positron lifetimes, a suitable positron source has to be chosen. The synthetic ^{22}Na isotope decays by efficient emission of a positron to ^{22}Ne . The excited ^{22}Ne emits a γ -quantum with an energy of 1.275 MeV, only a few picoseconds after the positron emission. Therefore, this 1.28 MeV γ -quantum can be utilised as start signal for positron lifetime measurements, while one of the two 511 keV annihilation quanta serves as stop signal. A typical fast-fast spectrometer setup is sketched in Figure 3.1. The γ -quanta are absorbed in a scintillation crystal and stimulate light emission. A photomultiplier converts this light signal into an electron pulse, which is proportional to the γ -quantum energy. Constant fraction differential discriminators are set to only accept either start or stop quanta. In a time to amplitude

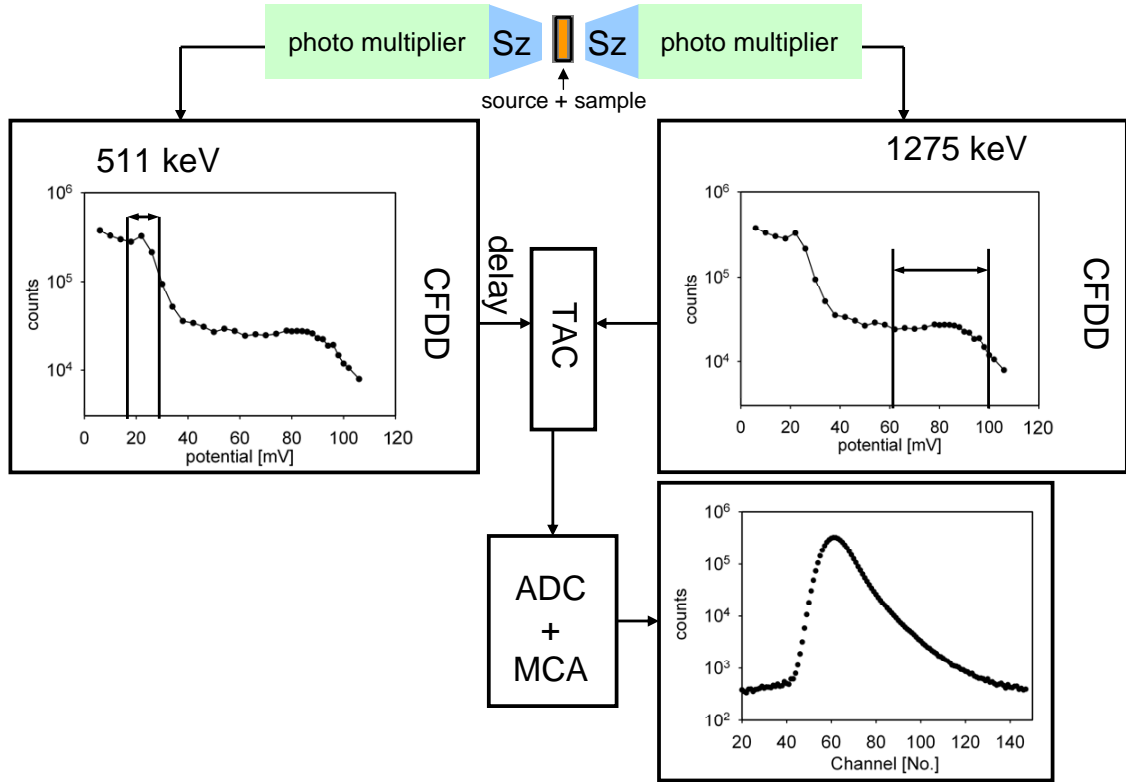


Figure 3.1: Sketch of the positron lifetime measurement setup. Sz: scintillation crystal, CFDD: constant fraction differential discriminator, TAC: time to amplitude converter, ADC: analog digital converter, MCA: multi-channel analyser

converter (TAC) the timing signal is converted to a voltage signal which is digitised in the analog to digital converter (ADC). The signal is then stored in a multi-channel analyser, where each channel represents a pre-set time interval. For assigning the correlated start and stop signal, a positron source activity of $<1\text{MBq}$ is chosen. This guarantees that there is only a single positron present within the sample at any time. 1MBq corresponds to 1 positron every $1\ \mu\text{s}$, which exceeds the positron lifetime within a sample by more than 3 orders of magnitude.

The measured spectra are composed of a sum of exponential decays, convoluted with an experimental time resolution function and a background. The time resolution function is approximated by a Gaussian with two exponential tails [64]. To determine the actual time resolution function, a radioactive source, which emits two γ -quanta with the correct energies, such as ^{207}Bi [23], which emits two γ -quanta with a timing difference of 130ps or by measuring a defect free sample, with a known lifetime, such as float zone

melted silicon, is used. In this work well annealed aluminium and float zone melted silicon were used as reference materials.

As the positron source utilised in this work is $^{22}\text{NaCl}$, which is packed between two layers of thin aluminium foil (Figure 3.2), positrons annihilating within the positron source material have to be taken into account as well.

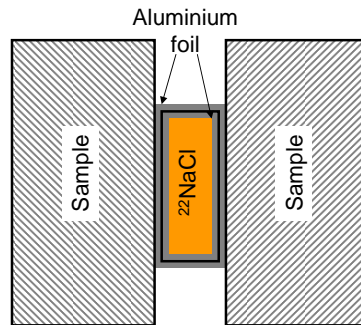


Figure 3.2: Sketch of the used positron source-sample sandwich. The $^{22}\text{NaCl}$ is packed between two layers of aluminium foil and placed between a pair of samples.

This source contribution consists of two positron lifetimes, first the lifetime of positrons annihilating within the NaCl (420ps [66, 67]) and the lifetime of positrons annihilating within the aluminium foil (165ps [68–70]). To determine the source contribution of the utilised positron sources the positron lifetime of well annealed palladium as reference material was investigated in this work, which exhibits a single positron lifetime of 106ps [65]. First, $^{22}\text{NaCl}$ was directly put onto a palladium foil. Another pair of annealed palladium foils was investigated with the typical positron source, $^{22}\text{NaCl}$ packed into a thin layer of aluminium foil and a third pair of palladium foils was investigated with a source covered with an additional aluminium layer, to protect the source. By analysing the obtained spectra, a source contribution of 320ps with an intensity of 14.5% was determined for the double layered positron source. This source lifetime is an intermixture of the positron lifetimes in NaCl and aluminium.

Measurements of the positron lifetimes have been performed on two spectrometer setups and prompt curves, approximated by a Gaussian with two exponential tails, characterised by the full width at half maximum (FWHM) of the Gaussian and the decay constants (λ_{left} , λ_{right}) given in picoseconds of 190,20,20 (FWHM, $\frac{1}{\lambda_{left}}$, $\frac{1}{\lambda_{right}}$) and

220,20,26 (FWHM, $\frac{1}{\lambda_{left}}$, $\frac{1}{\lambda_{right}}$) have been determined, utilising the program `pfposfit` [64]. The lifetime spectra have typically been fitted with either two or three positron lifetimes. A long lifetime of ≥ 1 ns and an intensity of $\leq 2\%$, which corresponds to positron annihilation at the sample surface, was obtained, but may be neglected in the discussion of the measurement results.

3.1.2 Positron annihilation Doppler broadening spectroscopy

Due to conservation of momentum of the electron-positron pair, the annihilation radiation shows deviations from collinearity by an angle Θ in the laboratory system. In addition, the momentum-component parallel to the direction of the emitted photons leads to an energy shift of the annihilation radiation in the laboratory system of

$$\Delta E = \pm \frac{p_z c}{2} \quad (3.1)$$

with p_z the part of the momentum in direction of the emitted photons and c the speed of light.

The thermalised positron does not significantly contribute to the momentum of the electron–positron pair. Therefore, the Doppler shift can be assigned to the electron momentum. Due to the low energy-shift, high resolution detectors, such as high purity germanium detectors are necessary to resolve the Doppler shift. Valuable information of the chemical environment of the annihilation site can be deduced from the contribution of high momentum core electrons. To resolve these high momentum events, a good peak to background ratio is necessary and this is achieved by simultaneous measurement of both annihilation quanta in a two detector setup, sketched in Figure 3.3. In addition, an improvement of the energy resolution by a factor of $\sqrt{2}$ can be achieved by using two high purity germanium detectors [13, 71]. A further background reduction is achieved by only using annihilation events, where $E_{\gamma_1} + E_{\gamma_2} = 2 \times 511 \text{ keV}$ is fulfilled. This method is typically referred to as two-dimensional Doppler broadening spectroscopy (2d-Doppler broadening). As the obtained spectra are characterised by relative changes, a determination of the resolution function may be skipped.

A sketch of the 2d-Doppler broadening measurement setup is presented in Figure 3.3. The annihilation radiation is detected by two high purity germanium detectors and con-

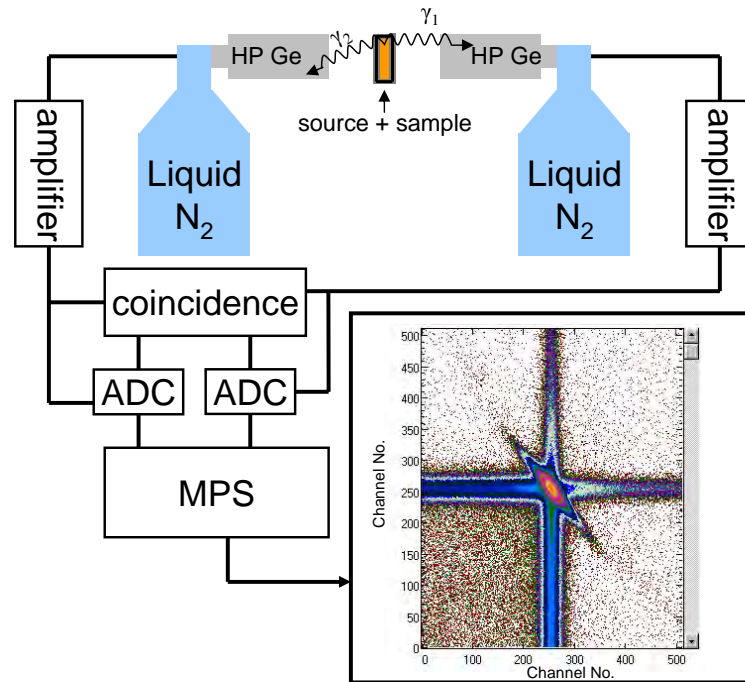


Figure 3.3: Sketch of the 2d-Doppler broadening measurement setup. ADC: analog to digital converter, MPS: multi parameter system, HP Ge: High purity Germanium detector

verted into electronic pulses. The detector outputs are only accepted, if both measured events are in timing coincidence, guaranteeing that both measured γ -quanta originate from the same annihilation event. The photon energies digitised in the analog to digital converter are then stored in a multi parameter system.

There are three different ways to evaluate the spectra obtained by 2d-Doppler broadening experiments. First, integral parameters, so called shape (S) and wing (W) parameter can be calculated. The S-parameter is a measure for annihilation with valence electrons and can be calculated by:

$$S = \frac{\sum_{i=a}^b N_i}{\sum_i N_i} \quad (3.2)$$

with N_i the content of channel i and the interval a to b , typically including electron momenta of $\pm 2.86m_0c \times 10^{-3}$. As the S-parameter gives the annihilation with valence electrons and the annihilation probability with valence electrons increases for positrons

trapped within open volume defects, the S-parameter can be used to monitor the introduction or annealing of open volume defects.

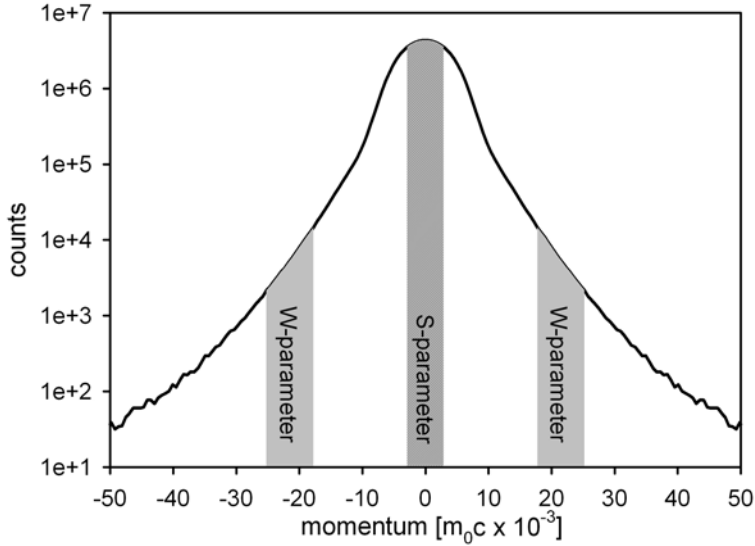


Figure 3.4: 2d-Doppler broadening spectrum of aluminium (mind the logarithmic scale). The marked areas denote the intervals utilised to calculate the S- and W-parameter

The high momentum core electrons contain element specific information, therefore, the W-parameter monitors changes in the chemical environment of the positron annihilation site. This can be best utilised in alloys. The W-parameter is calculated from the high momentum region by:

$$W = \frac{\sum_{i=c}^d N_i + \sum_{i=-d}^{-c} N_i}{\sum_i N_i}. \quad (3.3)$$

In this work, S and W parameter were calculated from $\pm 2.86 \times m_0c \times 10^{-3}$ and $\pm(17 - 25) \times m_0c \times 10^{-3}$ respectively (see Figure 3.4).

A second way to evaluate the 2d-Doppler broadening spectra, is a direct comparison of the measured spectra. As the absolute differences are relatively small, ratio spectra to a reference spectrum are formed. Therefore, the spectra have to be normalized and

are analysed in the following way:

$$F = \frac{N_{i_{sample}}}{N_{i_{reference}}}. \quad (3.4)$$

The obtained F , therefore, describes the deviation from the reference material. At low momenta, increasing or decreasing defect contribution can be observed, while at high momenta the chemical environment can be obtained by a characteristic shape, typical for individual elements.

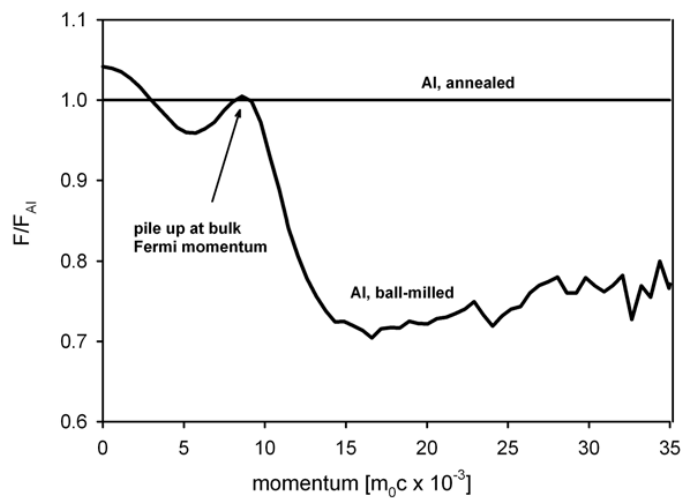


Figure 3.5: Spectrum of deformed aluminium with respect to pure aluminium. The increased annihilation with electrons with a momentum at the bulk Fermi edge is clearly visible at a momentum of $\approx 8 \times m_0c \times 10^{-3}$

Figure 3.5 shows such ratio spectra of aluminium and ball-milled aluminium, with aluminium as reference material. Increased annihilation with valence electrons in the ball milled sample can be observed by an increased F -ratio at low momenta, while a decreased annihilation with core electrons can be observed at high momenta. From the slope of the ratio curve at high momenta, the chemical environment can be determined. A local maximum at approximately $8 \times m_0c \times 10^{-3}$, just beyond the bulk Fermi momentum, is a typical feature of vacancies in aluminium [72, 73] and can be attributed to smearing of the Fermi cutoff associated with the motion of confined positrons [72]. This smearing is manifested as a peak just beyond the bulk Fermi momentum.

The third way to analyse the 2d-Doppler broadening spectra is a numerical separation of elemental contribution. An alloy spectrum is assumed to be a linear combination of the composing elements. Care has to be taken, as spectra obtained from defect free samples and samples with defects may deviate significantly (see Figure 3.5). Therefore, not only a linear combination of the defect free elemental samples is sufficient, but also the defected samples have to be taken into account. Otherwise, the chemical environment of a defect site would be largely underestimated. The fitting is carried out according to Somoza et al.[12]:

$$F_{\text{alloy}} = \sum_i w_i F_i + \sum_i w_i^* F_i^* \quad (3.5)$$

where i is the number of alloying elements, w_i the contribution of the pure elements and w_i^* the contribution of the defected elements and F and F^* denote the spectra of the annealed and defected elements, respectively. Boundary conditions for the fitting process are determined by normalising $\sum w_i$ to 1 and statistical weighting by $\frac{1}{F_{\text{alloy}}}$.

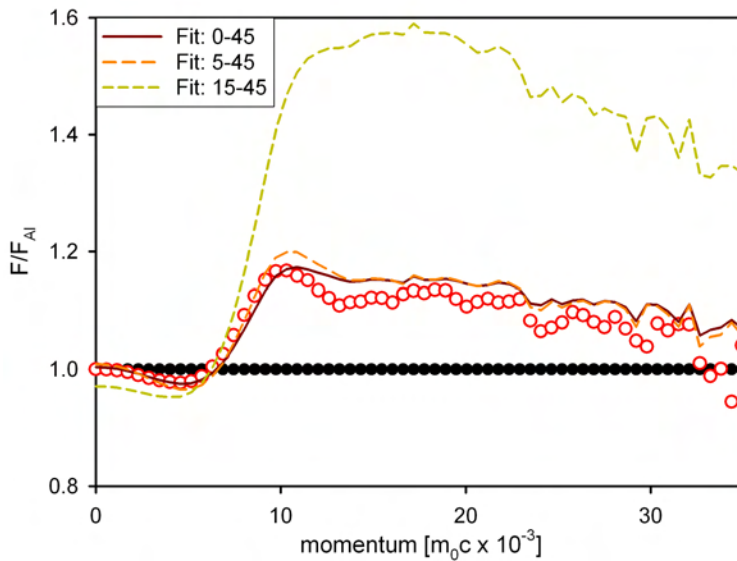


Figure 3.6: Spectrum of a quenched aluminium-copper alloy sample (red circles) with respect to pure aluminium (black circles). The quenched aluminium-copper alloy sample spectrum was fitted according to eq. 3.5 with pure aluminium, defected aluminium, and defected copper for three different fitting ranges. The results of the fitting are shown for comparison.

Figure 3.6 shows the fitting results on a quenched aluminium-copper alloy sample,

following equation 3.5, by choosing three different fitting ranges. As can be seen, choosing the fitting range at very high momenta ($\geq 15 \times m_0c \times 10^{-3}$), leads to an over estimation of the copper signature, whereas the local maximum at about $10 \times m_0c \times 10^{-3}$ is not reproduced. Fitting of the whole data range does not reproduce the local maximum at momenta of $\approx 10 \times m_0c \times 10^{-3}$, which is a significant feature of the measured spectrum. Therefore, an intermediate fitting range, starting at momenta of $5 \times m_0c \times 10^{-3}$ up to momenta of $45 \times m_0c \times 10^{-3}$ was chosen. This fitting interval gives the best fitting results over the whole momenta range.

3.2 Materials preparation

3.2.1 Nanostructured metals and alloys by high pressure torsion

To achieve bulk nanostructured materials, high pressure torsion was applied to different iron samples and an aluminium-copper alloy. High pressure torsion (HPT) is in principal a shear deformation. The specimen is placed between two anvils, which impose a hydrostatic pressure onto the sample. A high hydrostatic pressure omits the formation of cracks and pores [74, 75] while one of the anvils is rotated, as sketched in Figure 3.7. Therefore, bulk nanostructured materials can be produced.

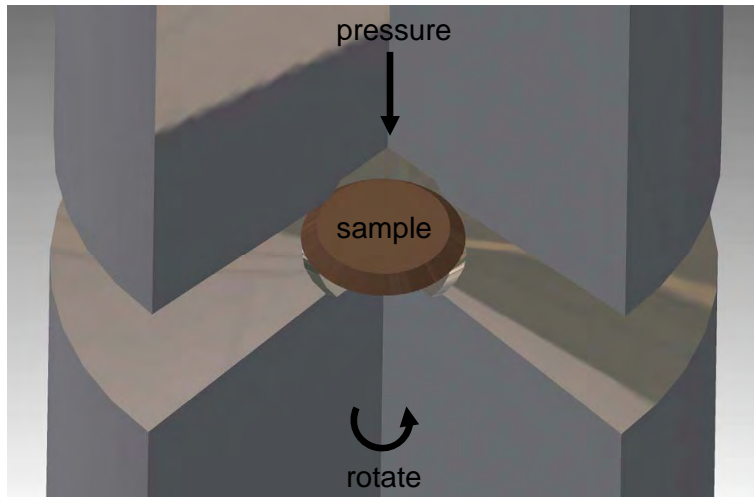


Figure 3.7: Sketch of the high-pressure torsion (HPT) deformation. The sample is placed between two anvils. A hydrostatic pressure is imposed onto the sample, while one of the anvils is rotated. Image by M. Luckabauer

The shear strain can be estimated according to [76, 77]:

$$\gamma = \frac{2\pi nr}{t} \quad (3.6)$$

where n , r and t denote to the number of revolutions, the distance from the centre of the sample and the sample thickness respectively. The deformation process starts by introducing dislocations, which are accumulated first at grain boundaries and upon further deformation even within the grains. These dislocations form cell blocks and upon further deformation even new high angle grain boundaries are formed [76]. This

processes go on, until a saturation is achieved, which means that further deformation does not change the microstructure any further. The HPT deformation leads to shear strains, which refer to a von Mises equivalent strain of [76]:

$$\epsilon_V = \frac{\gamma}{\sqrt{3}}. \quad (3.7)$$

3.2.2 Electrochemical defect introduction in functional oxides

Figure 3.8 sketches the charging and discharging process of lithium-ion batteries. Upon battery charging, lithium-ions are removed from the cathode material and transported via the liquid electrolyte to the graphitic carbon anode, where they are intercalated between graphite layers. The metal oxide framework of the cathode material stays intact upon Li^+ extraction and Li^+ -vacancies are left behind. Therefore, lithium-ions may be re-intercalated into the metal oxide framework upon discharging the battery. Due to the continued move of the lithium-ions between the electrodes, these types of batteries are often referred to as rocking chair batteries [78, 79]. Excessive Li^+ -extraction from the cathode material eventually leads to structural changes which may then lead to irreversible capacity loss [16].

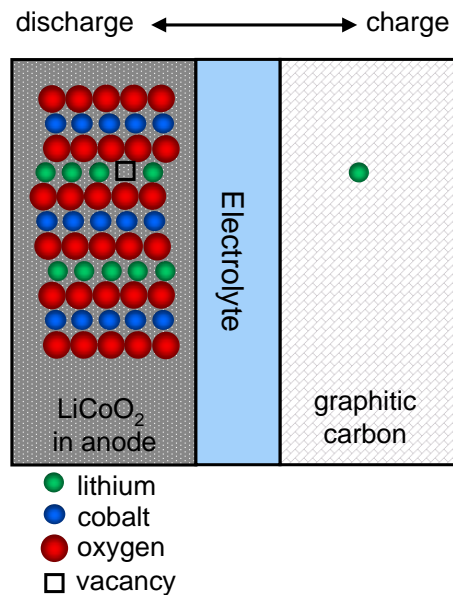


Figure 3.8: Sketch of the charging and discharging process in a Li-ion battery.

Figure 3.9 shows the typical voltage-composition plot of battery charging. Battery charging leads to the removal of lithium-ions from the cathode. These lithium-ions are transported via the electrolyte to the counter electrode, typically made of carbon and are stored there at interstitial sites.

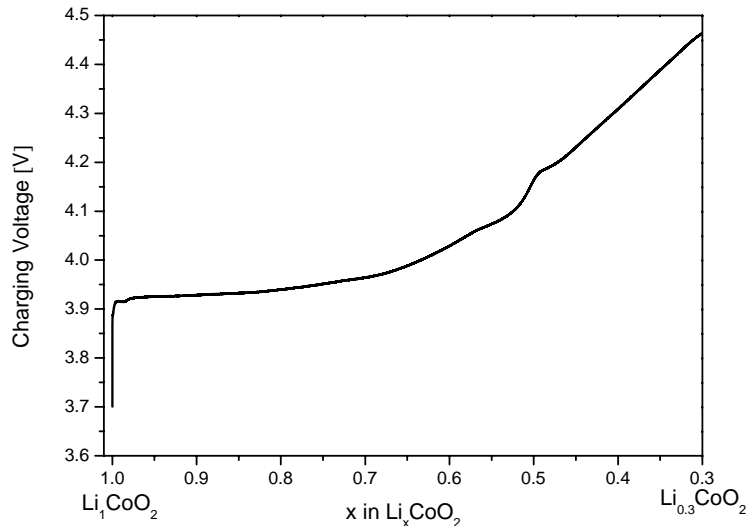


Figure 3.9: Battery charging voltage in dependence of Li^+ -extraction from the LiCoO_2 intercalation electrode material.

The investigated Li-ion battery cathodes were prepared by Bernd Fuchsbichler and Christian Baumann (VARTA Micro Innovations GmbH). The electrochemical tests were performed in a 3 electrode test-cell (Swagelok[®]-T-cell) using a metallic lithium foil as counter and reference-electrode. A polypropylene non-woven separator (Freudenberg FS2190) was used to isolate the composite electrode from the lithium counter-electrode. As electrolyte a mixture of ethylene carbonate (EC) and ethyl methyl carbonate (EMC) (volume ratio of EC:EMC=3:7) with 2 wt% vinylene carbonate (VC) and 1 M LiPF_6 as conducting salt was used.

The Li^+ -removal from the electrodes, which corresponds to battery charging, was performed with a Maccor Series 4000 battery tester at 20°C. After a six hour rest the electrodes were delithiated with a current density of about $13.5 \mu\text{A cm}^{-2}$ to their predefined remaining Li^+ -concentration. This corresponds to a so called C-rate of 0.005, which is defined as the inverse of the duration (in hours) necessary for complete Li^+ -

removal.

The switch off criteria at the final Li^+ -concentration was determined by the electrode capacity, which was calculated by using the theoretical capacity for the complete deintercalation of Li^+ from the active-electrode material. The theoretical capacity of LiCoO_2 , LiMn_2O_4 and $\text{Li}(\text{Co}_{1/3}\text{Mn}_{1/3}\text{Ni}_{1/3})\text{O}_2$ denote to 274 ,148 and 279 mAh g^{-1} , respectively. After Li^+ -extraction the test-cell was dismantled, the electrodes were carefully removed, washed with diethyl carbonate to remove the electrolyte and dried under vacuum (10^{-3}mbar) for 24 hours at 80°C . All the handling and measurements of the electrode (see Figure 3.10) were performed under protective argon atmosphere.

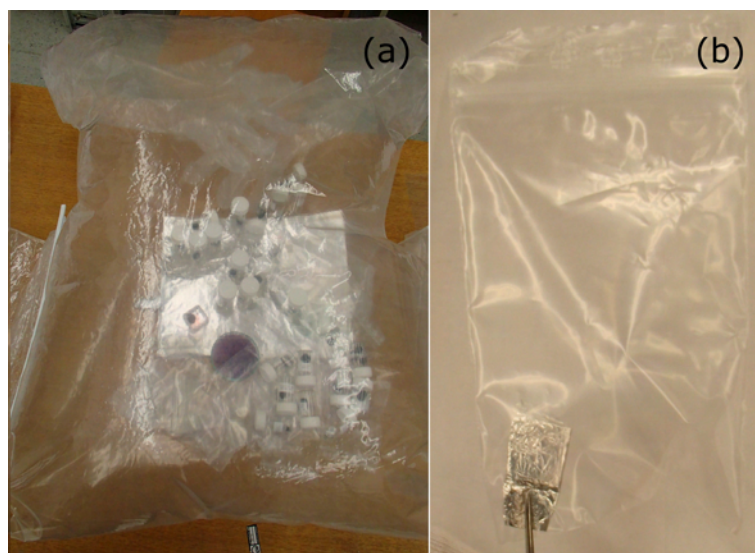


Figure 3.10: (a) Handling of Li-ion battery electrodes in an Glove-bag. (b) Measurements were as well performed in argon atmosphere.

X-ray-diffraction experiments were performed by Brigitte Bitschnau and Franz-Andreas Mautner (working group spectroscopy and electrochemistry of the Institute of Physical and Theoretical Chemistry, TU Graz) using a Bruker D8 Advance with a flat sample in Bragg-Brentano-Geometry utilising $\text{Cu-K}\alpha$ radiation. Diffractograms were measured in the 2Θ range from 15° to 130° with an increment of 0.03° . The spectra were analysed by Rietveld-refinement with the program FULLPROF [80, 81] and X'PertHighScorePlus (Panalytical).

Preliminary measurements

As no investigations of lithium-ion battery electrodes with positrons exist, the applicability of positron annihilation techniques on this kind of material had to be proven. Therefore, 2 pellets of 150mg of pure LiCoO_2 powder were pressed and investigated by positron lifetime spectroscopy and 2d-Doppler broadening spectroscopy. The results were compared to measurements on LiCoO_2 -electrodes. Due to the low thickness of the porous LiCoO_2 -electrode samples of about $170\mu\text{m}$, a fraction of positrons might annihilate in the aluminium substrate (see fig. 3.11). For clear comparability four different measurement-setups, as sketched in Figure 3.12 were investigated to determine the aluminium contribution. For a first test, an iron layer with a thickness of about 0.8 mm was added to determine the amount of positrons penetrating the electrode material. The amount of positrons annihilating within the iron layer may be subtracted from the measured electrode spectra. For the final measurements the iron layer was replaced by an aluminium layer with a thickness of about 1 mm. Therefore, only a single additional component for the aluminium current collector and the additional aluminium layer has to be subtracted from the electrode spectra.

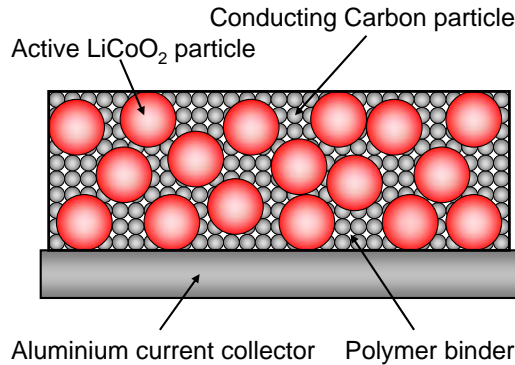


Figure 3.11: Sketch of the typical composition of LiCoO_2 electrodes.

Figure 3.13 shows the impact of the different measurement setups on 2d-Doppler broadening spectra. For easier deducibility, in this first approach, iron was chosen as reference material. Following the analysis method of fitting by utilising equation 3.5 the spectra were fitted to the following equation:

$$F = F_{\text{LiCoO}_2} \times w_{\text{LiCoO}_2} + F_{\text{Fe}} \times w_{\text{Fe}} + F_{\text{Al}} \times w_{\text{Al}} \quad (3.8)$$

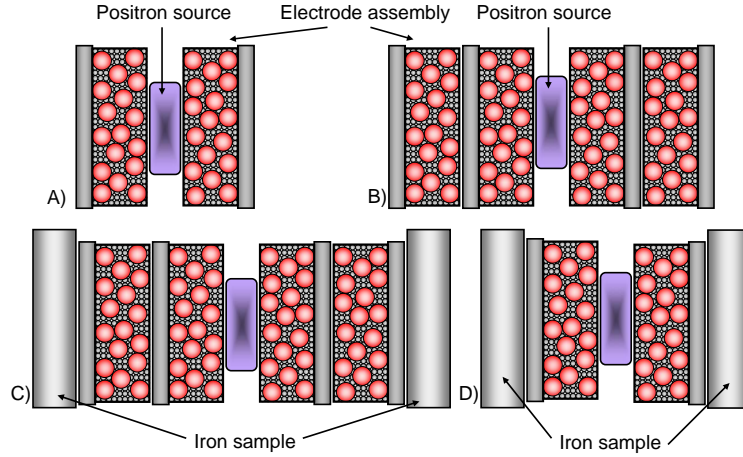


Figure 3.12: Sketch of the 4 different measurement setups to investigate the reliability of the results. A) Single electrode setup. B) Double electrode setup. C) Double electrode setup with iron support. D) Single electrode setup with iron support.

the amount of positrons, not annihilating within the active electrode material, could be calculated. For the 4 different setups, the results presented in Table 3.1 and Figure 3.13 were obtained.

Table 3.1: Weighting fractions of fitting the spectra according to equation 3.8. Geometry according to Figure 3.12.

geometry	w_{LiCoO_2}	w_{Fe}	w_{Al}
A	80	0	20
B	91	0	9
C	89	11	0
D	66	30	4

Due to availability of samples, measurements had to be performed in setup D. By utilising an aluminium support instead of the iron support, a correction fraction of 33% with a lifetime of pure aluminium (165ps) was added to the source correction. For reliability testing, measurements on different samples in measurement geometry A and D were performed.

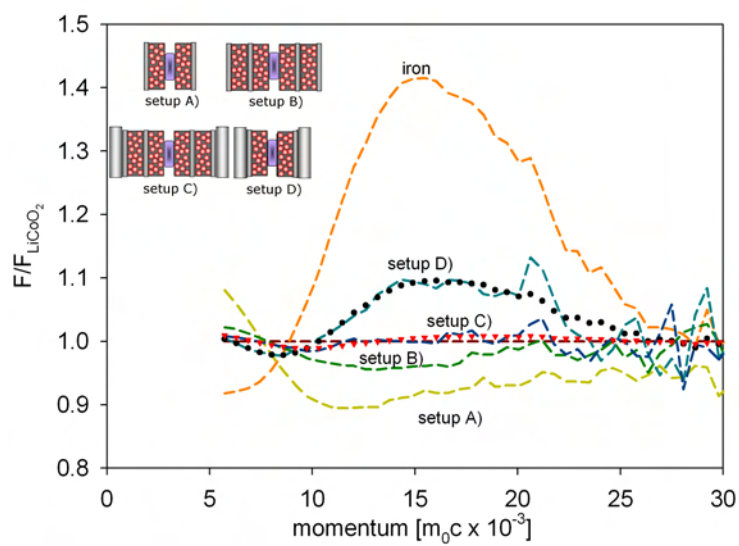


Figure 3.13: Comparison of 2d-Doppler broadening spectra of the 4 different measurement setups with respect to pure, compressed LiCoO_2 powder. By fitting according to eq. 3.8 the amount of positrons annihilating within the iron support can be calculated.

CHAPTER 4

Results and Discussion

4.1 Open volume defects in nanoscale alloys

Severe plastic deformation (SPD) has become one of the most promising methods to produce so called bulk nanostructured materials [82, 83]. High-pressure torsion (HPT) exhibits the benefit of high strain and, therefore, leads to fine microstructures down to grain sizes of less than 100nm [84] which is finer than obtained by other means of SPD [85], like equal channel angular pressing (ECAP). Beside the grain refinement, a high concentration of free volumes is introduced by this preparation method which has a major influence on the physical properties. Microstructures of pure metals processed by SPD have been widely investigated in the past two decades.

In this chapter open volume defects in nanoscale metals and alloys are discussed. A comprehensive set of materials was chosen to give a broad overview on the effects of open volumes on the nanometer scale. First, bulk nanostructured materials prepared by means of high-pressure torsion are presented. Structural materials, such as iron and aluminium-copper alloys were deformed and investigated to improve the understanding of materials properties after severe plastic deformation. Further on, an iron-nickel alloy

meteorite in perfect thermal equilibrium condition was investigated. Even though in perfect thermal equilibrium, precipitates in the nanoscale are present.

4.1.1 Iron

In this first part, the influence of sample purity on defect formation and annealing behaviour on HPT-deformed iron samples with different purities is presented. As reference materials ARMCO-iron, with a purity of $\approx 99.8\%$ (further referred to as "ARMCO-iron") and a second high-purity iron sample with a purity of $\approx 99.98\%$ (further referred to as "pure iron") were chosen. Both samples were subject to high-pressure torsion, performed at the Erich Schmid Institute of Materials Physics Leoben. Studies by means of difference dilatometry have been performed by Bernd Oberdorfer [86] and Boris Scherwitzl [87], while positron annihilation measurements on the ARMCO-iron were performed in the scope of the Diploma Thesis by Xiang Zhou [88] under the co-supervision of the author. The results of the mean positron lifetime measurements $\bar{\tau}$ and the 2d-Doppler broadening measurements ($\frac{S}{S_0}$) of the ARMCO-iron sample have already been published recently [89]. Here, a more detailed discussion of the positron lifetimes and 2d-Doppler broadening measurements will be presented.

Results

Initial condition

The main difference of the investigated iron samples is determined by the residual concentration of carbon. It is well known that carbon impurities can stabilise vacancies in iron [90, 91]. Both iron samples were initially annealed, to reduce the defect concentration. Samples with a diameter of 30mm and a thickness of 10mm were severely plastically deformed up to saturation deformation. This was achieved by means of high-pressure torsion (HPT). A pressure of 2.8 GPa was applied onto the samples and 10 revolutions were performed at room temperature. This leads to a von Mises equivalent strain of $\epsilon \approx 36$. This is larger than the equivalent strain of $\epsilon = 23$ which is reported to correspond to saturation deformation for this material [99]. The samples

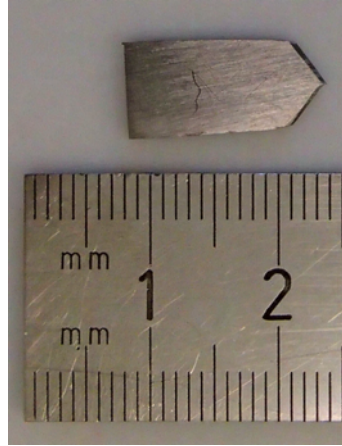


Figure 4.1: Iron sample after cutting from the deformed specimen.

were then cut and the surface polished. Right after deformation already differences in the microstructure of the ARMCO-iron and the pure iron samples are visible. Figure 4.2 shows the microstructure of the deformed ARMCO-iron and the pure iron sample. While the ARMCO-iron sample shows elongated grains with a mean diameter of about 150nm in the long direction the pure iron sample shows spherical grains with a mean diameter of about 340nm. The method of HPT, therefore, leads to a significant grain refinement, down to crystallite sizes in the 100 to 300 nm regime. The larger grain size of the high purity iron can be explained by dynamical recrystallisation during deformation due to the lack of stabilising impurities [84].

Table 4.1: Positron lifetimes of pure iron and defects in pure iron, reported in literature.

type	τ [ps]	literature
bulk	106-110	[91, 100, 101]
dislocation	150-167	[69, 92, 93],[100]
vacancy	175	[69, 90, 91]
vacancy-carbon	165	[90, 91]
grain boundary	126-174	[95, 96]
vacancy-cluster	210-500	[55, 91, 93, 94, 100]

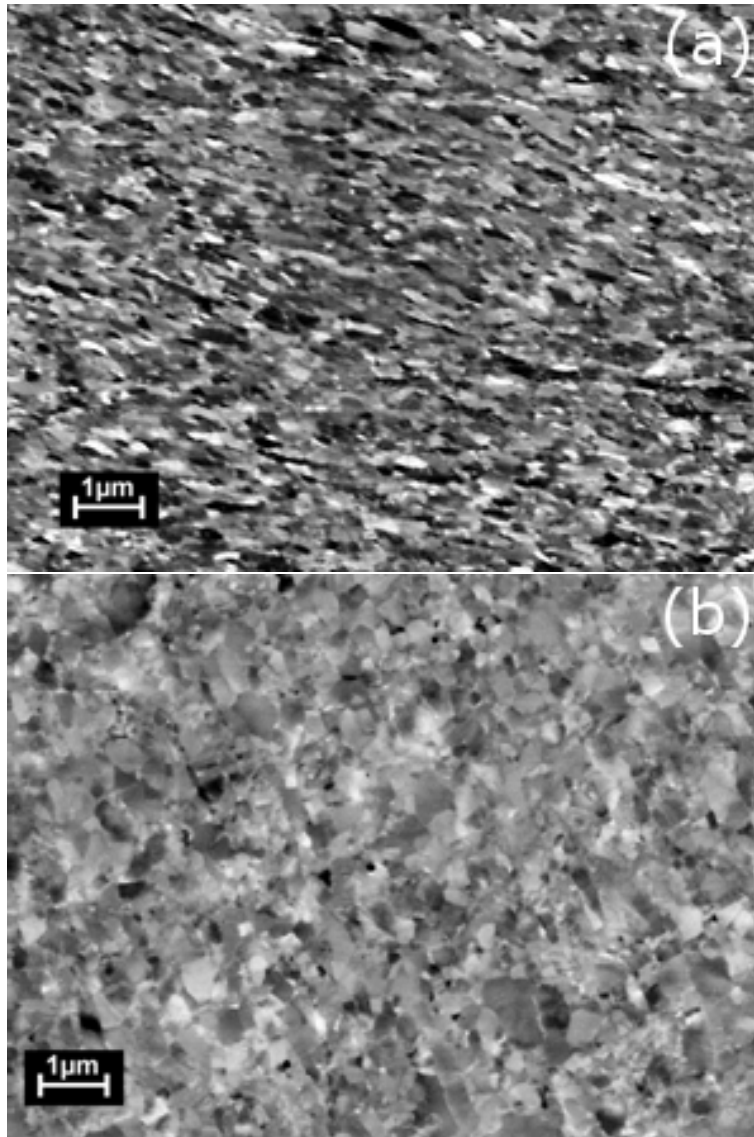


Figure 4.2: Scanning electron micrographs of the deformed iron samples. (a) ARMCO-iron and (b) pure iron. Published in [89].

In Table 4.1 an overview of positron lifetimes for trapping at different defects in iron, reported in literature is given. Positron lifetime measurements of the as deformed samples give a mean positron lifetime for ARMCO-iron of $\bar{\tau}_{ARMCO} \approx 145\text{ps}$ while the pure iron sample exhibits a mean positron lifetime of $\bar{\tau}_{pure} \approx 183\text{ps}$. A two-term analysis of the spectra reveals saturation trapping at defects for both samples. While in ARMCO-iron only a single positron lifetime of $\tau_2 = 145\text{ps}$ can be reliably identified, the pure iron sample shows two distinguishable lifetime components of $\tau_2 = 147\text{ps}$ and

$\tau_3 = 316\text{ps}$. These two positron lifetimes can be attributed to positron trapping at dislocations or grain boundaries and to trapping at vacancy-cluster. A positron lifetime of vacancy-clusters of $\tau_{vc} \approx 320\text{ps}$ is reported for a cluster size of about 6 vacancies [55, 93]. Positron lifetime calculations for positron trapping at grain boundaries from Kuriplach et al. [95, 96] give positron lifetimes of $\tau_{gb} = 126 - 174\text{ps}$, depending on the type of the grain boundaries and whether there are vacancies attached to the grain boundaries or not. Therefore, the positron lifetime of $\tau_2 = 145\text{ps}$ of the ARMCO-iron sample is most likely associated to trapping at grain boundaries and dislocations introduced by HPT. While all positrons are trapped at grain boundaries in the deformed ARMCO-iron sample, competitive trapping at grain boundaries and vacancy-clusters can be observed within the pure iron sample. Due to the positron diffusion length in metals of about 100nm [22] it seems plausible that all positrons reach grain boundaries within the elongated grains of the ARMCO-iron sample, while positrons annihilating within the grains of the pure iron sample are trapped at vacancy-clusters within the crystallites. The absence of single atom vacancies can be easily explained due to deformation at room temperature. It is well known [90, 91] that single atom vacancies in iron become mobile at temperatures of about -50°C , which is lower than the deformation temperature of about 20°C . In pure iron samples the formation of microvoids has been reported to occur [91] at temperatures higher than -50°C , which is in good agreement with the results found for the pure iron sample.

Isochronal annealing

The deformed iron samples were subjected to isochronal annealing in steps of $\approx 25^\circ\text{C}$ for 1 hour in vacuum up to 775°C . After each step S-Parameter measurements were performed which are presented in Figure 4.3.

The deformed pure iron sample show a constant value of the S-Parameter from room-temperature up to 175°C . From 200°C up to 500°C a linear decrease of the S-Parameter is observed and at temperatures higher than 500°C the measured S-Parameter stays constant.

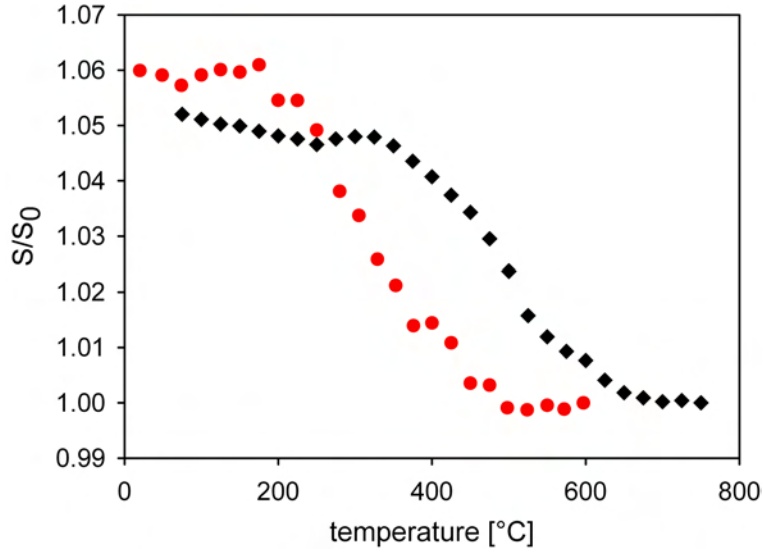


Figure 4.3: Comparison of S-parameter of pure (red) and ARMCO- (black) iron in dependence of annealing temperature, with respect to S_0 of the well annealed sample.

The ARMCO-iron sample reveals a different temperature behaviour. Up to temperatures of 350°C a slight decrease of the S-Parameter of the ARMCO-iron sample is present. Between 350°C and 600°C a change in the slope of the S-parameter curve occurs.

Obviously the different sample purities lead to a different defect annealing behaviour. The annealing temperatures of the ARMCO-iron sample are shifted to higher temperatures by about 100°C.

Upon temperature treatment, open volume defects are annealed out. To distinguish between trapping at grain boundaries and other open volume defects, such as vacancies, vacancy-clusters and vacancy-impurity-complexes, the mean grain size was determined from electron micrographs. These measurements were performed by Hohenwarter [97] for ARMCO-iron and by Scherwitzl [87] for the pure iron sample. In Figure 4.4 a relationship between the mean grain size and the S-parameter for both iron samples is indicated.

Initially the ARMCO-iron sample exhibited elongated grains with a mean diameter of about 150nm. Upon annealing at 350°C for 1 hour, spherical grains with a mean

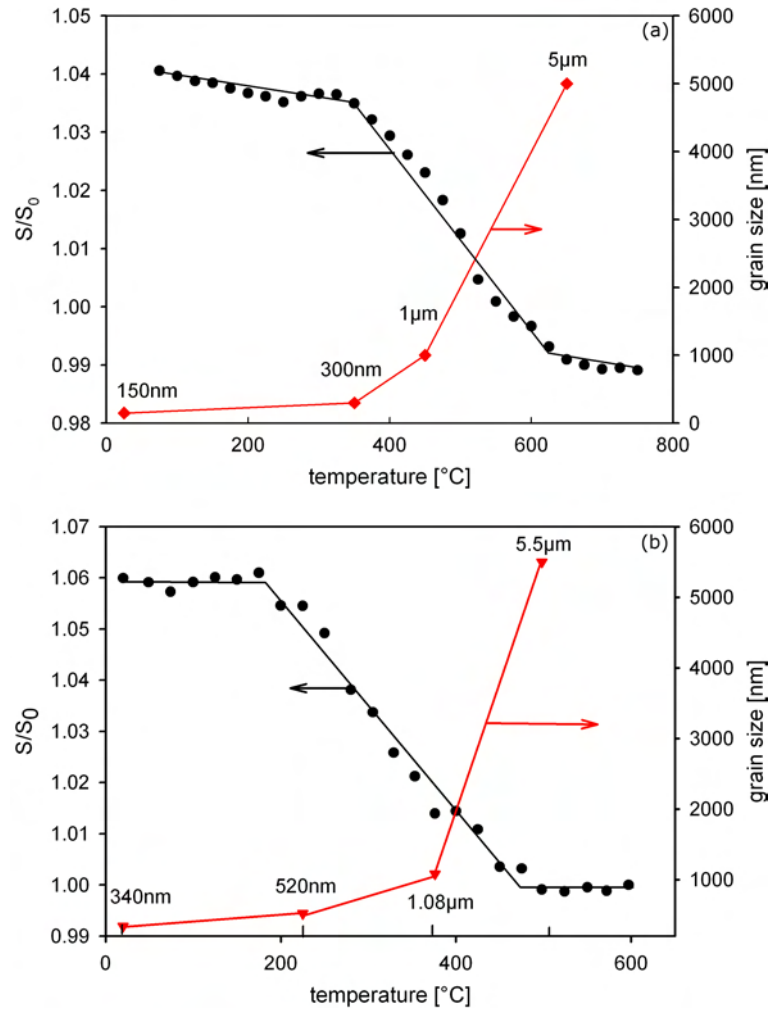


Figure 4.4: S-parameter plot of Doppler broadening and mean grain size deduced from SEM in dependence of annealing temperature, with respect to S_0 of the well annealed iron sample. (a) ARMCO-iron sample. (b) Pure iron sample.

diameter of 300nm are present. Further annealing at 450°C reveals a pronounced grain growth up to a mean grain size of $\approx 1\mu\text{m}$. After annealing at 650°C, which corresponds to half of the melting temperature a mean grain size of $\approx 5\mu\text{m}$ is obtained.

The pure iron sample shows a temperature induced grain growth from an initial value of about 340nm to $\approx 520\text{nm}$ after annealing at 236°C and further grain growth up to $\approx 1.08\mu\text{m}$ at 377°C. A mean grain size of $\approx 5.5\mu\text{m}$ after annealing at 502°C, is reported from Scherwitzl [87]. Figure 4.4 reveals, that the decrease of the S-parameter and the increase of the mean grain size show a reverse behaviour. The increase of the mean grain size leads to a decrease of the S-parameter, due to reduced trapping at grain boundaries. In addition, an increase of the recrystallisation temperature of about 100°C for the ARMCO-iron sample can be determined from the grain sizes (Figure 4.4) as well.

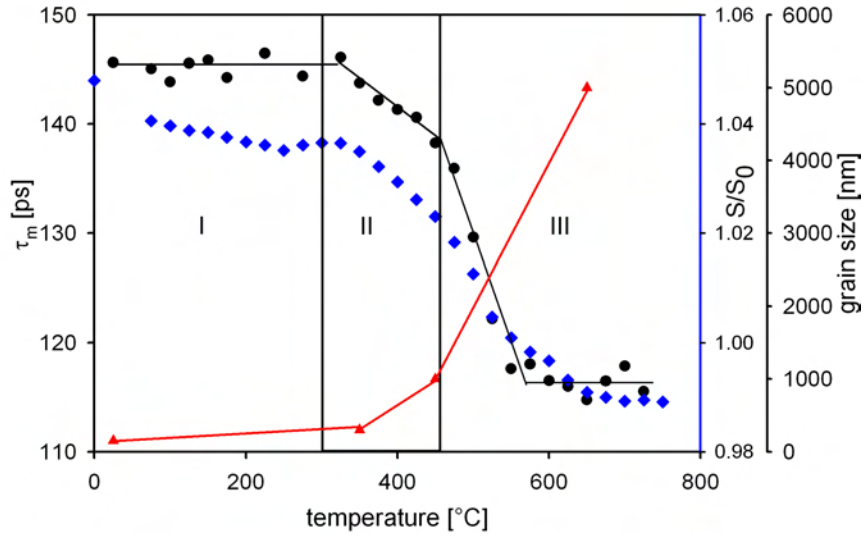


Figure 4.5: Mean positron lifetime $\bar{\tau}$ (black circles), S/S_0 -ratio (blue diamonds) and grain size (red triangles) of ARMCO-iron as function of the annealing temperature. Lines are guide to the eye.

In addition positron lifetime measurements were performed. The evolution of the mean positron lifetime of the ARMCO-iron sample and the $\frac{S}{S_0}$ -ratio are presented in Figure 4.5. From Figure 4.5 a very similar behaviour of the mean positron lifetime and the S-parameter of the ARMCO-iron sample can be deduced, however, the mean positron lifetime curve shows more pronounced features. The mean positron lifetime $\bar{\tau}$ reveals

three distinct annealing stages, stage I up to about 300°C, stage II between 300 and 450°C and stage III at temperatures higher than 450°C. Initially in stage I, $\bar{\tau}$ stays constant, due to saturation trapping at deformation induced defects. As can be deduced from Figure 4.5, hardly any grain-growth occurs within this stage. At temperatures between 300°C and 450°C a decrease of $\bar{\tau}$ takes place. This may be attributed to the annealing of deformation induced dislocations as well as the beginning grain growth. At temperatures higher than 450°C (stage III), a change in the slope of $\bar{\tau}$ is clearly visible. At these high temperatures, pronounced grain growth takes place.

Initially, up to temperatures of 475°C, a two component analysis of the positron lifetime data of the ARMCO-iron sample is not feasible, due to saturation trapping at grain boundaries, dislocations and deformation induced defects. At temperatures higher than 475°C a two component analysis reveals positron annihilation from the free state and trapping at open volume defects with a positron lifetime of $\tau_2 \approx 162\text{ps}$ (see Table 4.2). With increasing temperature, the defect lifetime τ_2 increases, up to $\approx 190\text{ps}$, while its intensity decreases from 61% at 475°C to 20% at 700°C.

The positron lifetime τ_2 of 190ps is proposed to originate from vacancy-impurity-complexes, while the lifetime value of 162ps is an intermixture of positron lifetimes due to competitive trapping at grain boundaries ($\tau_{gb} = 154\text{ps}$) and vacancy-impurity-complexes ($\tau_{v-imp} \approx 190\text{ps}$). These complexes are stable up to temperatures of at least 725°C (see Table 4.2).

The defect lifetime of 190ps is higher than positron lifetimes reported for vacancies in pure iron ($\tau_V = 175\text{ps}$ [91]). In fact, vacancies in pure iron are reported to anneal out at temperatures of about -50°C and positron trapping in deformed pure iron is found for dislocations and vacancy-cluster [90, 91]. In addition carbon-stabilised vacancies start to anneal out at 80°C, due to the migration of the interstitial carbon at this temperature and a carbon-vacancy dissociation temperature of 250°C is reported [90, 91]. The observed shift of the defect annealing temperatures here, therefore, has to be correlated to larger vacancy-carbon-complexes.

An alternative interpretation of the defect lifetime component of 190ps is based on the results of Kuriplach et al. [96]. They found by numerical simulations that vacancies attached to grain boundaries are stable up to temperatures of 475°C with a positron

Table 4.2: Mean positron lifetime $\bar{\tau}$ of the ARMCO-iron sample at different annealing temperatures. At temperatures higher than 450°C a two component analysis can be performed and a reduced positron bulk lifetime τ_1 and defect lifetime τ_2 with their respective intensities I_1 and I_2 are obtained.

temperature	τ_1 (± 2)[ps]	τ_2 (± 4)[ps]	I_1	I_2	$\bar{\tau}$ (± 2)[ps]
20°C	-	-	-	-	146
75°C	-	-	-	-	145
100°C	-	-	-	-	144
125°C	-	-	-	-	145
150°C	-	-	-	-	146
175°C	-	-	-	-	144
200°C	-	-	-	-	146
225°C	-	-	-	-	146
250°C	-	-	-	-	145
275°C	-	-	-	-	144
300°C	-	-	-	-	145
325°C	-	-	-	-	146
350°C	-	-	-	-	144
375°C	-	-	-	-	142
400°C	-	-	-	-	141
425°C	-	-	-	-	141
450°C	-	-	-	-	138
475°C	91	162	36	61	136
500°C	88	171	49	49	130
525°C	90	176	61	36	122
550°C	91	178	68	30	118
575°C	94	180	70	27	118
600°C	92	183	71	26	117
625°C	96	196	78	20	116
650°C	94	186	75	22	115
675°C	94	190	75	23	116
700°C	98	197	77	20	118
725°C	95	189	76	21	115

lifetime of $\approx 194\text{ps}$ and anneal out at temperatures higher than 625°C .

The mean positron lifetime of the pure iron sample can be separated into two different defect lifetimes right after deformation (see Table 4.3), namely $\tau_2 = 154\text{ps}$ from trapping at grain boundaries and deformation induced dislocations and $\tau_3 = 316\text{ps}$ from trapping at vacancy-clusters. Annealing up to 200°C does not have any influence on the measured positron lifetimes. After annealing at 900°C , two remaining lifetimes can be distinguished, namely positron annihilation from the free state with $\tau_1 = 103\text{ps}$ and annihilation within vacancy-cluster with a lifetime of $\tau_3 \approx 207\text{ps}$. This result indicates annealing of vacancy-clusters, in fact emission of vacancies from vacancy-cluster at temperatures higher than 250°C is also reported by Eldrup et al. [94].

Table 4.3: Mean positron lifetime $\bar{\tau}$ of the pure iron sample at different annealing temperatures. Two different defect lifetimes could be separated, namely τ_2 and τ_3 with their respective intensities I_2 and I_3 . After annealing at 900°C , τ_1 can be attributed to the reduced bulk lifetime with the intensity I_1 .

temperature	τ_1 (± 2)[ps]	τ_2 (± 2)[ps]	τ_3 (± 3)[ps]	I_1	I_2	I_3	$\bar{\tau}$ (± 2)[ps]
20°C	-	154	316	-	81.2	18.8	185
125°C	-	152	320	-	80.5	19.5	185
200°C	-	150	317	-	80.7	19.3	182
900°C	103	-	207	79	-	21	125

Figure 4.6 shows the 2d-Doppler broadening spectra of deformed and annealed pure iron as well as deformed and annealed ARMCO-iron with respect to annealed pure iron. After deformation the spectra show strong similarities, only between momenta of $(30 \text{ to } 35) m_0c \times 10^{-3}$ differences can be monitored. In the annealed state, deviations of the ARMCO-iron sample from the pure iron sample can be deduced at momenta from 0 to $30 m_0c \times 10^{-3}$. This is a strong indication, that impurities lead to a change in the positron annihilation characteristics of the ARMCO-iron.

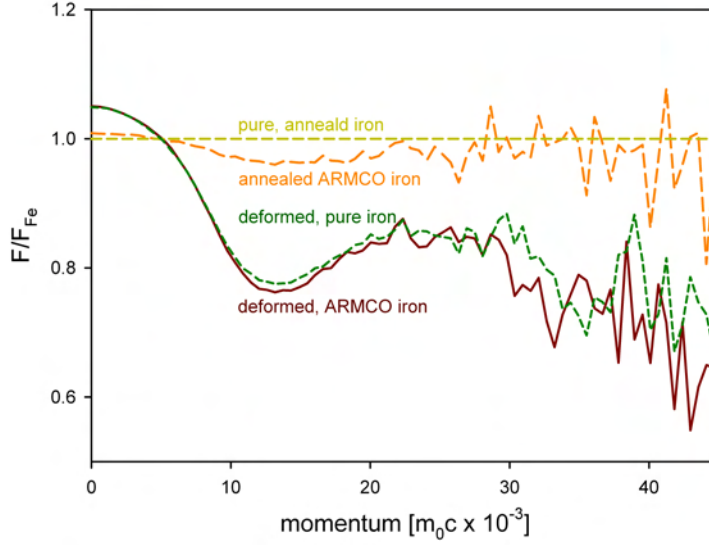


Figure 4.6: 2d-Doppler broadening spectra of deformed and annealed ARMCO-iron as well as deformed and annealed pure iron with respect to annealed pure iron. The significant deviation of the annealed spectra reveals the influence of impurities.

Calculation of defect densities

The positron lifetimes and intensities of the pure iron sample upon temperature treatment are given in Table 4.3. Up to temperatures of 200°C complete trapping of positrons at two different defect populations, namely grain boundaries and vacancy-cluster, can be observed. In this case, the intensities of the positron lifetime components of the defects are proportional to the corresponding trapping rates. The ratio of the intensities and, therefore, the ratio of the trapping rates are given by $\frac{I_{vc}}{I_{Gb}} = \frac{\kappa_{vc}}{\kappa_{Gb}} = \frac{1}{4}$. The mean grain sizes at the temperatures were estimated according to Figure 4.4 (b). According to theoretical calculations by Nieminen et al. [98] the specific trapping rate of a vacancy-cluster μ_{cl} is proportional to the number of vacancies in the cluster, valid for the case of small cluster radii. The value κ_{Gb} can be calculated according to $\kappa_{Gb} = \frac{3\alpha}{r_0}$ [63], while κ_{vc} may be calculated according to $\kappa_{vc} = \mu_{cluster} \times C_{cluster}$ utilising a specific trapping rate $\mu_{cluster} = \mu_{vacancy} \times \bar{N}$ with \bar{N} the average number of vacancies in the cluster and $\mu = 4 \times 10^{14} s^{-1}$ for pure metals [61]. Positron lifetimes

of 320ps and 208ps correspond to vacancy-cluster containing about 6 (320 ps) and 3 (208 ps) vacancies [23], respectively. The calculated vacancy-cluster concentration of the as deformed sample, with a grain radius r_0 of 340 nm and $\alpha = 1 \times 10^4 \text{m s}^{-1}$ [27, 102], is $C_{cluster} \approx 4 \times 10^{-6}$. Calculating the initial vacancy-concentration, forming the vacancy-cluster leads to $C_v \approx 3 \times 10^{-5}$. This concentration of vacancies is significantly smaller than the vacancy-concentrations of 10^{-4} , reported for HPT-deformed metals, investigated by dilatometry [4] and calorimetry [1, 2]. As vacancies attached to dislocations are reported to exhibit positron lifetimes in the range of 150-167 ps, they cannot be separated from positron trapping at grain boundaries ($\tau_{Gb} = 154\text{ps}$). As the concentration of vacancies attached to dislocations cannot be calculated, the vacancy-concentration calculated from the vacancy-cluster reported here is lower than the absolute vacancy-concentration introduced by HPT. After annealing at 900°C a remaining cluster concentration of about 8×10^{-7} is found from the two state trapping model. This cluster-concentration cannot be accessed by dilatometry or calorimetry, as these methods determine the vacancy-concentrations from annealing.

A numerical analysis of the positron lifetimes obtained for the ARMCO-iron samples is not as straight forward. Temperature treatments of up to 450°C reveal complete positron trapping at deformation induced dislocations and grain boundaries. After annealing at 475°C and higher two distinguishable positron lifetimes can be determined (see Table 4.2), namely, a reduced bulk lifetime τ_1 and a defect lifetime τ_2 . This defect lifetime component shows a steady increase from 162ps at 475°C up to about 190ps at 625°C and stays constant after annealing at higher temperatures. At temperatures higher than 625°C the simple trapping model (STM) may be applied and a concentration of the vacancy-impurity-complexes of $C_{v-imp} \approx 3.12 \times 10^{-6}$ can be calculated using the specific trapping rate of $\mu = 4 \times 10^{14} \text{s}^{-1}$ for pure metals [61]. The positron lifetime τ_2 obtained in the temperature range from 475°C and 600°C is assumed to be an intermixture of two lifetimes, originating from positron trapping at grain boundaries ($\tau_{Gb} \approx 154\text{ps}$) and trapping at vacancy-impurity-complexes ($\tau_{v-imp} = 190\text{ps}$). As a numerical separation of the two defect lifetimes from the measured spectra could not be performed, the following concept for analysis was applied. A linear combination of the two defect lifetimes of the vacancy-impurity-complex and grain boundaries was performed, leading to the measured lifetime, following $\tau_2 = I'_1 \times \tau_{v-imp} + I'_2 \times \tau_{Gb}$ with

$I'_1 + I'_2 = 1$. This analysis shows that between 475°C and 600°C the ratio of trapping at grain boundaries and vacancy-impurity-complexes changes from $\frac{I_{v-imp}}{I_{Gb}} = \frac{1}{4}$ to $\frac{I_{v-imp}}{I_{Gb}} = \frac{4}{1}$.

Table 4.4: Calculated mean positron lifetime $\bar{\tau}$ obtained by the diffusion transition trapping model, equation 2.15. Grain radii were estimated from Figure 4.5 and a constant vacancy-impurity concentration of $C_{v-imp} = 3.12 \times 10^{-6}$, obtained from the simple trapping model applied to the 725°C annealed state, was assumed.

temperature	grain radius [nm]	calculated $\bar{\tau}$ [ps]	measured $\bar{\tau}$ (± 2)[ps]
475°C	510	136	136
500°C	900	127	130
525°C	1200	124	122
550°C	1500	121	118
575°C	1650	121	118
600°C	2000	120	117

In Table 4.4 the mean positron lifetimes, according to the diffusion-transition trapping model (equation 2.15) were calculated. For the performed calculations, some assumptions on positron diffusion length, the specific trapping coefficient at grain boundaries and the specific trapping coefficient at vacancy-impurity complexes had to be made. A typical positron diffusion length of $D = 0.8 \text{ cm}^2 \text{ s}^{-1}$ [103] was assumed and a specific trapping coefficient at grain boundaries α of $\alpha = 10^4 \text{ m s}^{-1}$ [27, 102] and the specific trapping coefficient of vacancies in pure metals $\mu = 4 \times 10^{14} \text{ s}^{-1}$. As a constant vacancy-impurity concentration $C_{v-imp} = 3.12 \times 10^{-6}$ was found by applying the simple trapping model to the measurement results at temperatures higher than 600°C, it seems safe to assume, that this concentration is constant at lower temperatures as well. The mean grain sizes were estimated according to Figure 4.5. As can be seen in Table 4.4, the measured and calculated values of $\bar{\tau}$ are in good agreement.

Discussion

The results on HPT deformed ARMCO- and pure iron samples give a comprehensive picture about the influence of impurities on the deformation induced defects as well as the defect annealing characteristic. Stabilizing effects of carbon impurities on vacancies in iron have been reported [90, 91]. It has been shown, that the sample purity has a strong impact on the defect stability. First, a different shape and size of the grains produced by HPT was found. In ARMCO-iron positron trapping at grain boundaries and dislocations and vacancy-carbon-complexes is dominating, while in pure iron in addition to trapping at grain-boundaries and dislocations the formation of vacancy-cluster with a cluster size of about 6 vacancies was observed. Further the annealing characteristic is quite similar for both samples, but the defect annealing is shifted to higher temperatures in the ARMCO-iron sample by about 100°C. Positron trapping at grain boundaries obviously seems to play an important role up to grain sizes of almost 5 μ m (see Table 4.4 and Figure 4.4) and was found for both purity samples. Such a phenomenon has in fact recently been proposed by Oberdorfer [62]. In addition to grain refinement, vacancy-impurity-complexes (ARMCO-iron), $C_{v-imp} \approx 3 \times 10^{-6}$, and vacancy-cluster (pure iron), $C_{vc} \approx 4 \times 10^{-6}$, are formed upon HPT deformation. Upon temperature treatment of the pure iron sample, similar to the results reported by Eldrup et al. [94], a reduction of the positron lifetime from $\tau_3 = 320$ ps to 208ps is observed as larger voids start to dissipate but are still present after temperature treatment as high as 900°C. Residual concentrations of vacancy-impurity-complexes in ARMCO-iron $C_{v-imp} \approx 3 \times 10^{-6}$ and vacancy-cluster in pure iron of $C_{vc} \approx 8 \times 10^{-7}$ were found.

4.1.2 Al-3wt%Cu

Parts of the measurements on an Al-3wt%Cu alloy have been published in the *Physics Procedia* [104] and the *Journal of Applied Physics* [105]. Sample preparation (homogenisation and HPT-deformation) and TEM investigation were performed by Michael Faller (Erich Schmid Institute of Materials Sciences Leoben), SEM images by Herbert Reingruber (Austrian Centre for Electron Microscopy and Nanoanalysis). The positron lifetime and 2d-Doppler broadening measurements, interpretation and discussion of the results, as well as predominant manuscript composition were performed by the author.

Materials properties

Aluminium alloys are well known as high strength and low weight materials with a wide range of applications. This can be attributed to the phenomenon of precipitation hardening. In aluminium, copper is completely solvable at 548°C up to a content of 5.65wt% [106, 109] (see Figure 4.7). Quenching from this high temperature leads to a supersaturated solid solution and upon aging at lower temperatures semi-coherent and coherent precipitates are formed. The precipitation process is sketched in Figure 4.8. At low temperatures coherent layers of copper, so called Guinier-Preston zones (GP-zones), are formed. Increasing the temperature leads first to the formation of multilayer Guinier-Preston zones, so called Θ'' -precipitates, further aging leads to the formation of the semi-coherent, non-equilibrium Θ' -precipitates. These fine dispersed precipitates inhibit dislocation climbing and improve, therefore, the mechanical stability of the material. At very long aging times finally the equilibrium, incoherent Θ -precipitates are formed. The coarsening of these precipitates leads to a decrease of the materials hardness.

Aluminium alloys have recently become object of severe plastic deformation. Upon multiple runs of Equal Channel Angular Pressing (ECAP) Murayama et al. [32] found a partly dissolution of the semi-coherent Θ' -precipitates. Lechner et al. [9] observed the same behaviour in a commercial aluminium alloy (DURAL) upon high pressure torsion. Overall it could be shown, that severe plastic deformation on aged aluminium alloy samples leads to fine crystallite sizes and fragmentation of the precipitates. In

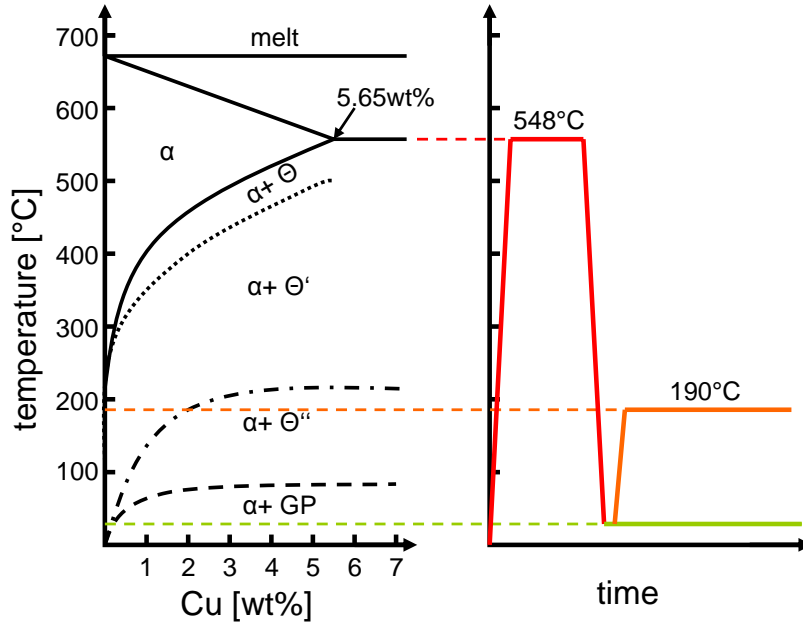


Figure 4.7: Aluminium rich section of the Al-Cu phase diagram and typical aging temperatures (after [106]). α = solid solution, GP = Guinier-Preston zones, Θ'' = multilayer Guinier-Preston zones, Θ' = semi-coherent precipitates, Θ = incoherent Al_2Cu precipitates.

the following the introduction of defects by HPT, the defect annealing characteristics and the effect on the precipitation processes on an Al-Cu alloy will be presented.

Preparation

For the present study an Al-3wt%Cu alloy was homogenised and afterwards cut into slices with a diameter of 14mm and a thickness of 2mm. These samples were solution treated at 550°C for 3 hours in argon atmosphere and afterwards quenched into water of $\approx 15^\circ\text{C}$. One pair of samples was subsequently subjected to HPT deformation [107]. The specimen was placed between two anvils, which imposed a hydrostatic pressure of 2.1 GPa onto the sample. One of the anvils was rotated for 3.5 revolutions. This deformation was performed at room temperature. The HPT deformation leads to a shear strain of $\gamma \approx 55$ at the investigated area, which refers to a von Mises equivalent strain of $\epsilon_V \approx 32$ ($\epsilon_V = \gamma/\sqrt{3}$). This deformation corresponds to the saturation regime which defines the limit of microstructural refinement [108] by HPT. For comparison

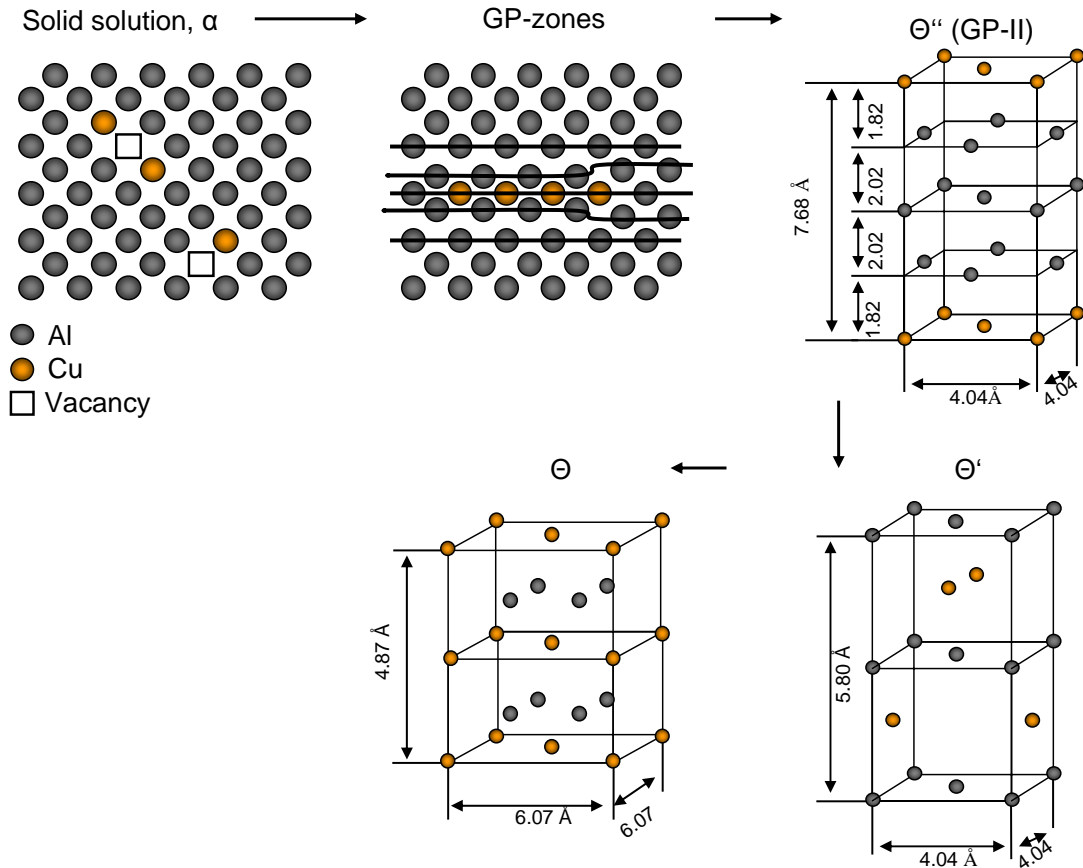


Figure 4.8: Sketch of the precipitation processes occurring in Al-Cu alloys upon aging (after [106]). α = solid solution, GP = Guinier-Preston zones, Θ'' = multilayer Guinier-Preston zones, Θ' = semi-coherent precipitates, Θ = incoherent Al_2Cu precipitates.

undeformed samples with the same pre-treatment (solution treated at 550°C for 3h and quenched into water of 15°C) were also studied. The HPT-deformed and the undeformed sample were subject to isothermal (193°C) heat treatment up to 290 hours and subsequent isochronal (1h) annealing in vacuum in temperature steps of approximately 30°C, from 230°C to 531°C. In fact the 193°C isothermal heat treatment was chosen to omit the early stages of precipitation formation and to reduce the annealing time until peak hardness is achieved. After each temperature treatment the samples were slowly cooled down to room temperature. The thermal treatment was accumulative. In addition pure aluminium, as well as ball-milled aluminium and HPT-deformed copper were measured as reference materials.



Figure 4.9: Deformed (left) and undeformed (right) Al-3wt%Cu samples after annealing treatment. After etching the grain size in the mm range can be seen by the naked eye.

Results

Initial state after quenching

In the first part results on the solution treated and quenched reference samples (further referred to as "undeformed") as well as on the solution treated, quenched and HPT-deformed samples (further referred to as "HPT") are presented. Figure 4.10 shows the 2d-Doppler broadening spectra of the undeformed Al-3wt%Cu reference sample, the HPT-deformed sample, as well as spectra of deformed aluminium and deformed copper in comparison to pure aluminium.

Comparing the Al-3wt%Cu undeformed reference sample to the spectra measured on ball-milled aluminium and deformed copper reveals three main features. First, at low momenta ($< 2 \times m_0c$) $\times 10^{-3}$ the reference sample shows enhanced $\frac{F}{F_{Al}}$ -ratios compared to pure undeformed Al (can hardly be distinguished from Figure 4.10), as typical for positron trapping at open volume defects. Second, a local maximum at a momentum of approximately $10 \times m_0c \times 10^{-3}$ can be identified. A similar maximum at a momentum of approximately $8 \times m_0c \times 10^{-3}$ can be observed for ball-milled aluminium (Figure 4.11), whereas deformed copper does not show such a local maximum (see Figure 4.10). This local maximum, just beyond the bulk Fermi momentum, is a typical feature of vacancies in aluminium [72, 73] and can be attributed to smearing of the Fermi cutoff associated with the motion of confined positrons [72]. This smearing is manifested as

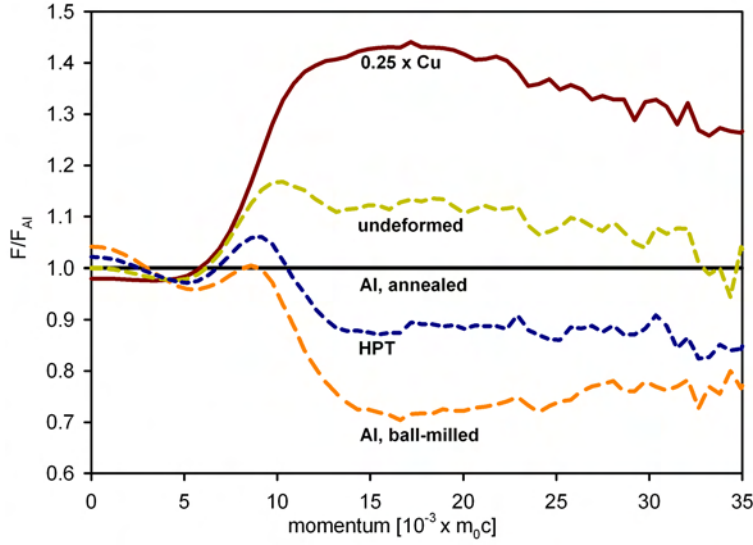


Figure 4.10: Comparison of 2d-Doppler broadening Spectra of HPT deformed copper, undeformed Al-3wt%Cu, HPT deformed Al-3wt%Cu and ball milled aluminium. Plotted are the $\frac{F}{F_{Al}}$ ratios of the spectra, with the spectrum of pure aluminium (F_{Al}).

a peak just beyond the bulk Fermi momentum. In copper this smearing is obscured by the contribution of the 3d electrons.

A slight shift of this local maximum in the undeformed reference sample may be attributed to an overlap of the peak-like feature of the vacancy in aluminium with the positive slope of the increasing left shoulder which is due to a copper containing environment. The third feature is a negative slope of the spectrum from a momentum of $17 \times m_0c \times 10^{-3}$ onwards, similar to deformed copper. These three characteristic features together (see Figure 4.10) indicate the annihilation of positrons at vacancy-type defects in aluminium, stabilised by copper atoms, forming vacancy-copper complexes, which are created by the solution treatment and quenching. The 2d-DB spectra of the undeformed sample was also analysed with linear combinations of the momentum distributions of pure annealed aluminium, defected aluminium and defected copper according to equation 3.5, leading to the following equation:

$$F = F_{Al} \times w_{Al} + F_{Al_{def}} \times w_{Al_{def}} + F_{Cu_{def}} \times w_{Cu_{def}} \quad (4.1)$$

Figure 4.12 and Table 4.5 show the component analysis of the 2d-DB spectra. The

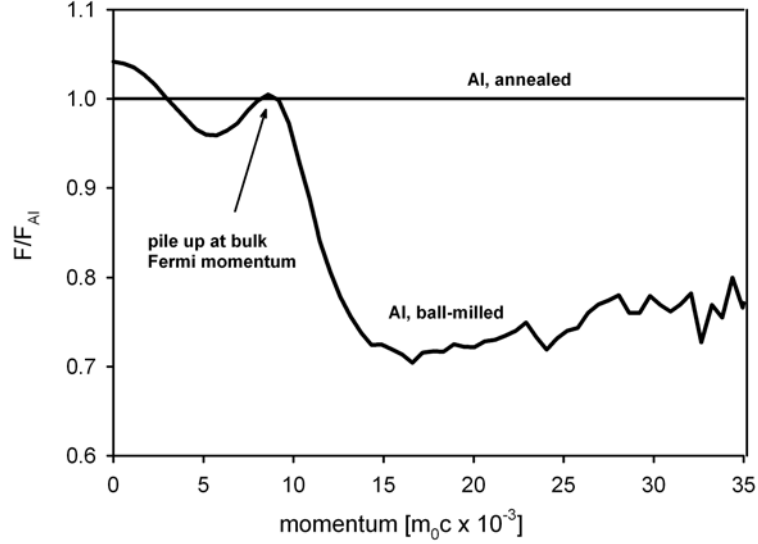


Figure 4.11: Spectrum of deformed aluminium with respect to pure aluminium. The increased annihilation with electrons with a momentum at the bulk Fermi edge is clearly visible at a momentum of $\approx 8 \times m_0c \times 10^{-3}$

results for the undeformed reference sample in the initial state after quenching show a strong deformed aluminium signature ($w_{Al_{def}} = 0.58$) in addition with a strong copper signature ($w_{Cu_{def}} = 0.22$). This shows clearly, that vacancies, stabilised by copper atoms, were quenched in. This conclusion is in agreement with literature see e.g. Folegati et al. [110] and Somoza et al. [111]. In addition, vacancies in aluminium are known to anneal out at temperatures between about -70°C to -20°C [112, 113]. Therefore, at least one copper atom has to be attached to each vacancy. From the weighting fractions of deformed aluminium and deformed copper an estimation of the mean copper environment of the quenched in vacancies can be deduced by the following equation, taking into account the 12 next neighbours of a vacancy:

$$C_{Cu_{def}} = \frac{w_{Cu_{def}}}{w_{Al_{def}} + w_{Cu_{def}}} \quad (4.2)$$

This gives a $C_{Cu_{def}}$ of 27.5% which can be attributed to a mean copper environment of about 3.3 copper atoms per vacancy. This result is in good agreement with the mean copper environment of about 3, reported for quenched Al-Cu-alloys from experiments [12, 114] and calculations [110].

Table 4.5: Weighting fractions obtained by fitting the measured spectra according to equation 4.1.

undeformed	w_{Al}	$w_{Al_{def}}$	$w_{Cu_{def}}$	HPT	w_{Al}	$w_{Al_{def}}$	$w_{Cu_{def}}$
20°C	0.20	0.58	0.22	20°C	0.07	0.85	0.08
193°C -1h	0.94	0	0.06	193°C -1h	0.40	0.59	0.01
193°C -5h	0.92	0	0.08	193°C -5h	0.46	0.53	0.01
193°C -10h	0.88	0	0.12	193°C -10h	0.44	0.54	0.02
193°C -48h	0.78	0	0.22	193°C -48h	0.54	0.45	0.01
193°C -72h	0.70	0.04	0.26	193°C -72h	0.58	0.41	0.01
193°C -120h	0.73	0	0.27	193°C -120h	0.52	0.46	0.02
193°C -168h	0.66	0.04	0.30	193°C -168h	0.58	0.41	0.01
193°C -239h	0.72	0	0.28	193°C -239h	0.68	0.31	0.01
193°C -290h	0.72	0	0.28	193°C -290h	0.70	0.30	0
230°C -1h	0.72	0	0.28	230°C -1h	0.70	0.30	0
260°C -1h	0.72	0	0.28	260°C -1h	0.65	0.34	0.01
290°C -1h	0.78	0	0.22	290°C -1h	0.84	0.16	0
320°C -1h	0.83	0	0.17	320°C -1h	0.95	0.05	0
350°C -1h	0.88	0	0.12	350°C -1h	0.99	0.01	0
373°C -1h	0.95	0	0.05	373°C -1h	0.99	0	0.01
415°C -1h	0.96	0	0.04	415°C -1h	0.98	0	0.02
445°C -1h	0.96	0	0.04	445°C -1h	0.98	0	0.02
473°C -1h	0.95	0	0.05	473°C -1h	0.97	0	0.03
504°C -1h	0.97	0	0.03	504°C -1h	0.96	0	0.04
531°C -1h	0.96	0	0.04	531°C -1h	0.96	0	0.04

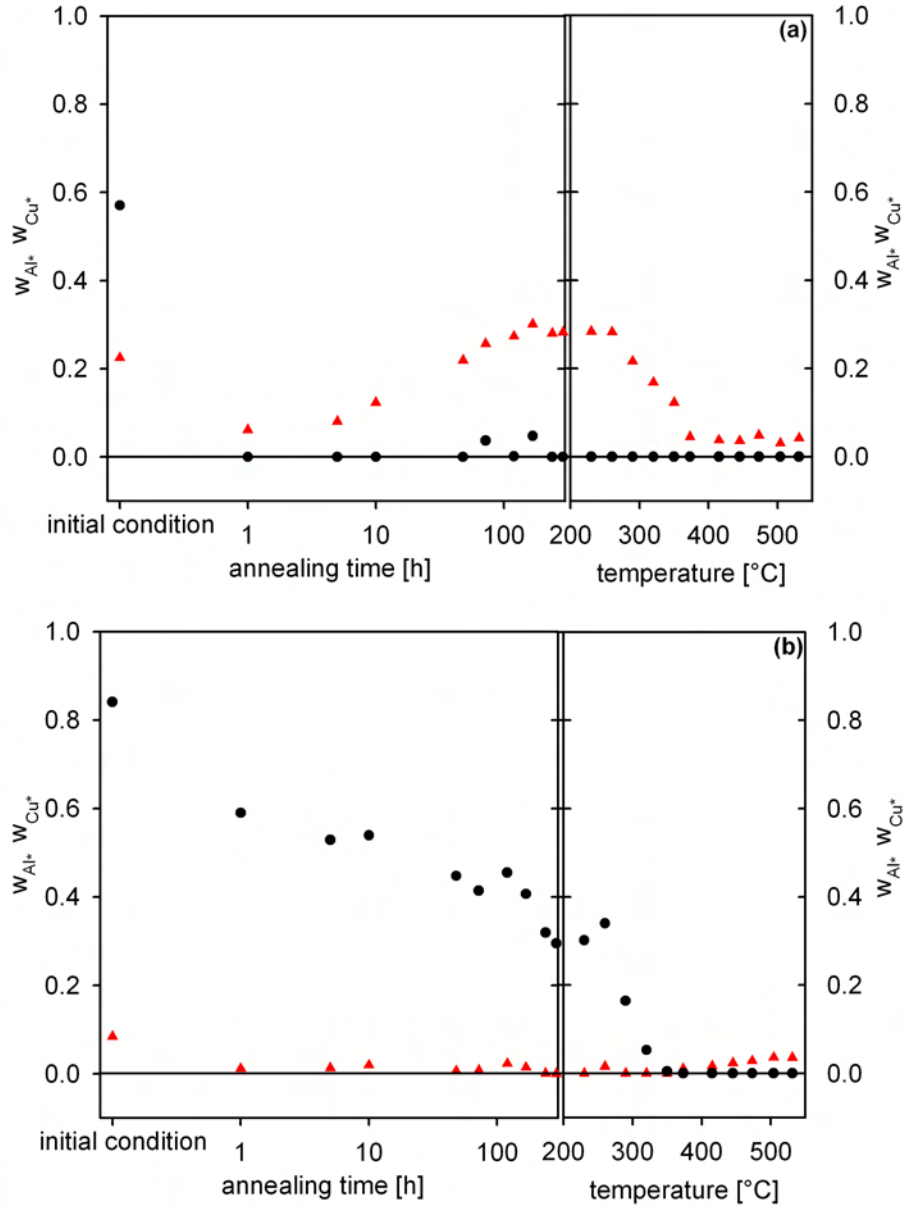


Figure 4.12: Evolution of the weighting fractions of deformed copper ($w_{Cu_{def}}$, red triangles) and deformed aluminium ($w_{Al_{def}}$, black circles) of (a) the undeformed reference sample and (b) the HPT-deformed sample, obtained by fitting the measured spectra according to equation 4.1 upon temperature treatment.

TEM investigations after solution treatment and quenching give no indication of formed incoherent precipitates, as can be seen in Figure 4.13(a1).

In the undeformed sample a relatively high mean positron lifetime of 196 ps (Figure 4.14 and Table 4.6) can be observed. This lifetime is higher than the positron lifetime in bulk aluminium ($\tau_b = 165\text{ps}$), but lower than the lifetime of positrons trapped at aluminium vacancies ($\tau_V = 246\text{ps}$) [115] or vacancy-copper complexes ($\tau_{V-Cu} = 229 - 206\text{ps}$, depending on copper environment) [116]. This positron lifetime of 196ps is often found in as quenched samples [110, 117–119] and is most likely a mixture of positron lifetimes of vacancy-copper complexes, with a lifetime of ≈ 205 ps often found in literature [116, 117, 120, 121] and 178ps (found by Ferragut et al. [118] after short heat treatment at 150°C for 1min). The formation of Guinier-Preston zones, with a positron lifetime of 167ps [116], in the quenched sample is possible, but can not be confirmed by the measurements. A comprehensive overview on positron lifetimes in aluminium and aluminium-copper alloys is presented in Table 4.7.

The HPT-deformed sample shows a quite different behaviour compared to the undeformed reference sample (Figure 4.10). A pronounced similarity to the 2d-Doppler-broadening spectrum of ball-milled aluminium is obvious (Figure 4.10). Despite the similarity to ball-milled pure aluminium, a weak copper signature can be identified at high momenta. This copper signature is indicated by the negative slope of the ratio parameter curve of the HPT deformed sample for momenta greater $\approx 17 \times m_0c \times 10^{-3}$ (Figure 4.10). All of this indicates that positrons are mainly trapped at open volume defects with a dominant aluminium environment and indicates a high defect density introduced by HPT. The minor copper signature may derive from a small fraction of remaining vacancy-copper complexes or from free volume type defects at grain boundaries with segregated copper. This interpretation is very well supported by the numerical fitting process, which reveals a contribution of $w_{Al_{def}} = 0.85$ from the ball-milled aluminium spectrum and a reduced copper fraction of $w_{Cu_{def}} = 0.08$, whereas for the undeformed reference a value $w_{Cu_{def}} = 0.22$ (Figure 4.12 and Table 4.5) is obtained. This view is also supported by a linear combination of the two 2d-DB spectra obtained for (i) the sample after solution treatment and quenching and (ii) for the ball

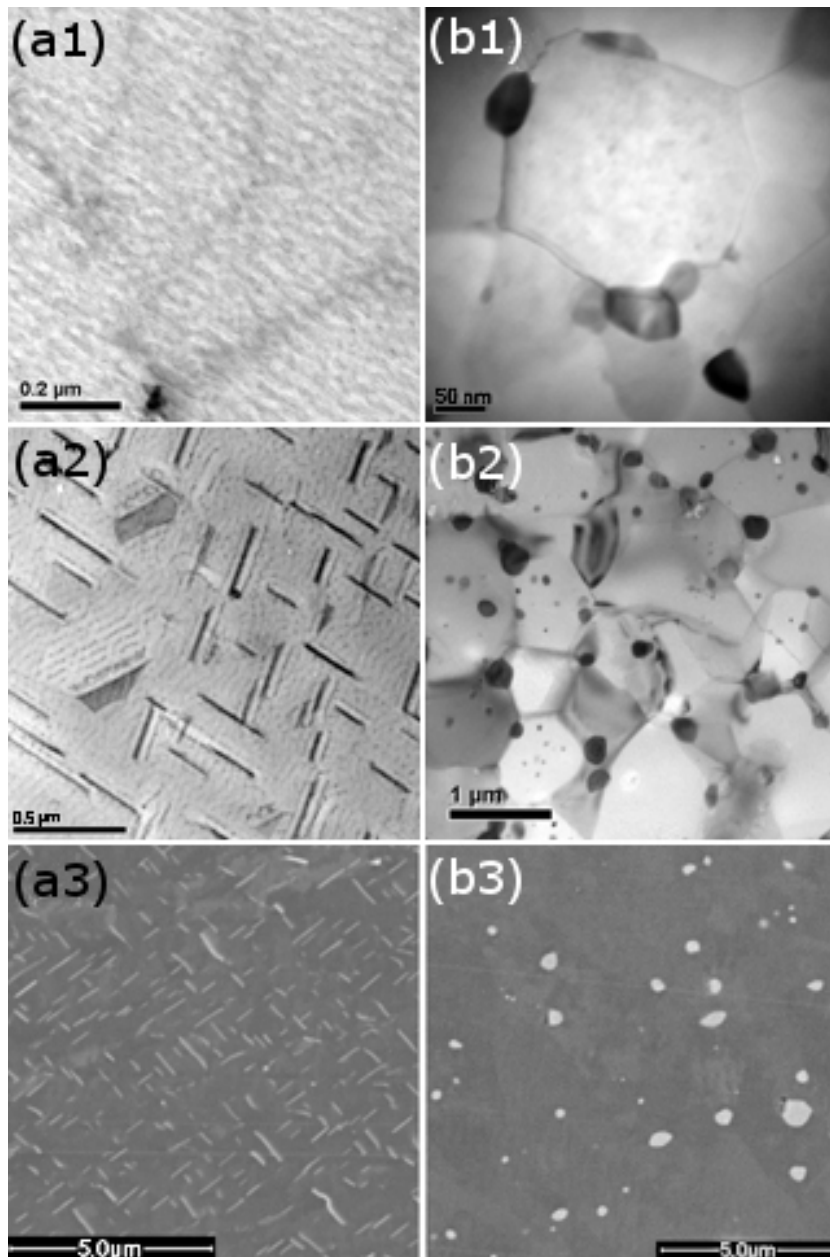


Figure 4.13: Electron micrographs of (a) undeformed and (b) HPT-deformed Al-3wt%Cu sample at different annealing stages. (a1) undeformed sample after solution treatment and quenching, (b1) HPT-deformed after solution treatment and quenching. ((a2),(b2),TEM) undeformed and HPT-deformed sample respectively after aging for 144h at 193°C. ((a3),(b3),SEM) undeformed and HPT-deformed sample after aging at 320°C for 1h.

Table 4.6: Positron lifetimes τ_1 (± 2 ps)[ps] and τ_2 (± 3 ps)[ps] obtained by fitting the measured spectra with two components. An additional positron lifetime of $\tau_3 \geq 1$ ns with an intensity $\leq 0.5\%$ could be resolved as well. This lifetime component can be attributed to positron annihilation at surface states and, therefore, is not further discussed.

undeformed	τ_1 [ps]	τ_2 [ps]	I_1	I_2	HPT	τ_1 [ps]	τ_2 [ps]	I_1	I_2
20°C	-	196	-	100	20°C	-	211	-	100
193°C -1h	165	-	100	-	193°C -1h	-	208	-	100
193°C -5h	167	-	100	-	193°C -5h	-	206	-	100
193°C -10h	167	-	100	-	193°C -10h	114	226	21.1	78.9
193°C -48h	173	-	100	-	193°C -48h	101	221	21.2	78.8
193°C -72h	174	-	100	-	193°C -72h	100	221	23	77
193°C -120h	176	-	100	-	193°C -120h	109	223	25.8	74.2
193°C -168h	177	-	100	-	193°C -168h	120	227	31.3	68.7
193°C -239h	176	-	100	-	193°C -239h	134	236	41.6	58.4
193°C -290h	176	-	100	-	193°C -290h	127	232	37.5	62.5
230°C -1h	175	-	100	-	230°C -1h	101	214	22.1	77.9
260°C -1h	177	-	100	-	260°C -1h	90	209	18.4	81.6
290°C -1h	176	-	100	-	290°C -1h	122	216	35.4	64.6
320°C -1h	173	-	100	-	320°C -1h	101	196	22.1	77.9
350°C -1h	108	182	18.3	81.7	350°C -1h	91	186	18.3	81.7
373°C -1h	166	-	100	-	373°C -1h	166	-	100	-
415°C -1h	165	-	100	-	415°C -1h	165	-	100	-
445°C -1h	164	-	100	-	445°C -1h	165	-	100	-
473°C -1h	164	-	100	-	473°C -1h	163	-	100	-
504°C -1h	164	-	100	-	504°C -1h	165	-	100	-
531°C -1h	163	-	100	-	531°C -1h	163	-	100	-

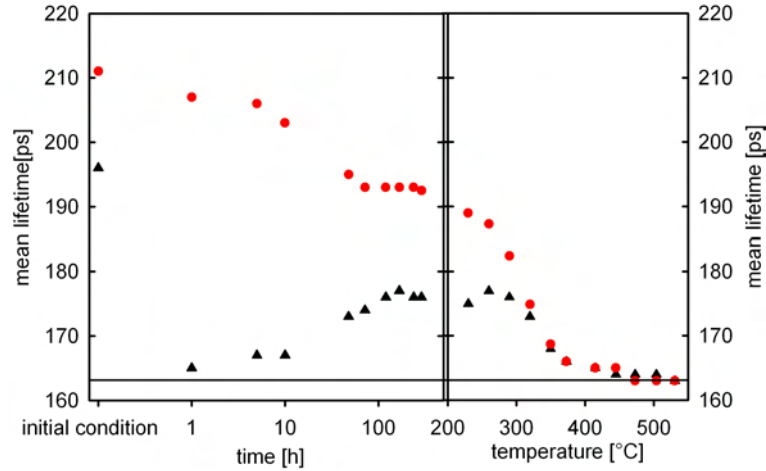


Figure 4.14: Mean positron lifetime $\bar{\tau}$ of the undeformed (black triangles) and the HPT-deformed samples (red circles) in dependence of the isothermal annealing at 193°C and the isochronal annealing (1h).

Table 4.7: Positron lifetimes in aluminium and aluminium-copper alloys reported in literature.

Al	τ [ps]	reference	Al-Cu-alloy	τ [ps]	reference
bulk	159-168	[68],[69],[70]	bulk	165 / 168	[70]
vacancy	245-252	[115, 123]	vac.-Cu	235, 205-229	[70],[116]
edge disloc.	215,173	[69],[123]	GP-zones	167	[116]
disloc. loop	191	[123]	Θ''	178 / 167	[118],[124]
disloc.+vac.	225	[123]	Θ'	174 / 193	[120],[121]
disloc.+jog	224, 220	[123],[69, 125]	Θ	≈ 143	[121]

milled sample to fit the as deformed 2d-DB spectrum. This analysis leads to a very appropriate approximation of the measured spectrum, as presented in Figure 4.15, and therefore supports the above mentioned interpretation.

The excellent agreement of the measured values and the fitted values is evident. Following the assumption that the remaining vacancy-copper-complexes have a similar copper environment as in the undeformed state given by

$$w_{V-Cu} = \frac{w_{Cu_{def}}}{w_{Al_{def}} + w_{Cu_{def}}} = \frac{0.22}{0.80}. \quad (4.3)$$

With this proportion, the fraction of positrons trapped at vacancy-copper complexes

may be estimated by:

$$\frac{(w_{Cu_{def}}/w_{V-Cu})}{w_{Al_{def}} + w_{Cu_{def}}} \approx \frac{1}{3}. \quad (4.4)$$

Only every third positron is trapped at a copper decorated defect in the HPT deformed sample.

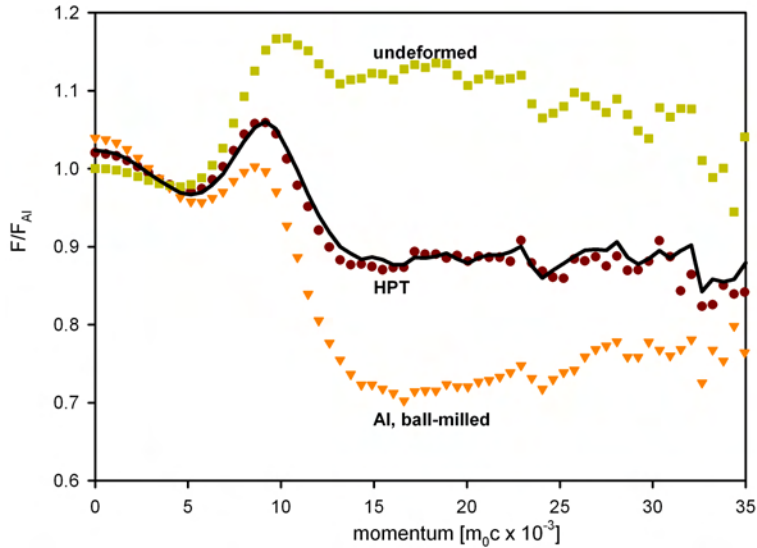


Figure 4.15: Result of fitting (solid line) the HPT-deformed sample by linear combination of the undeformed quenched sample and the ball milled aluminium sample.

The mean positron lifetime of 212 ps for the HPT-deformed sample is significantly higher than that for the undeformed reference sample (Figure 4.14 and Table 4.6), indicating a much higher defect density and the existence of different types of defects, such as dislocations and grain boundaries. In fact, HPT leads to grain refinement and a similar positron lifetime of deformed Duralumin ($\bar{\tau} = 215\text{ps}$) has been reported by Lechner et al. [9]. TEM images reveal a mean crystallite size in the range of 100nm after deformation (Figure 4.13, (b1)). These crystallites are stabilised by precipitates, which are found at grain boundaries and triple junctions (Figure 4.13, (b1)). These precipitates have to be formed during the HPT process otherwise crystallite sizes in the 100nm regime would not be stable in aluminium. In fact, in pure aluminium crystallite sizes only in the μm regime can be achieved by HPT due to dynamic recrystallisation [77, 122]. Taking into account the diffusion length of positrons (trapping model at grain boundaries) [62] saturation trapping of positrons at free volume-type defects in grain

boundaries and dislocations is most likely to take place. It is remarkable that even though positrons diffuse typically in the 100nm range reaching the grain boundaries, no evidence for trapping at the Al_2Cu precipitates can be found. This can be considered as further evidence for strong positron trapping at deformation-induced lattice defects.

For a rough quantitative estimation of the remaining vacancy-copper-complex concentration, competitive trapping at grain boundaries and vacancies is assumed. Therefore, the trapping rate of the vacancy-copper-complexes ($\kappa_{V-Cu} = \mu \times C_{V-Cu}$) is in a ratio of 1:3 (as shown above) to the trapping at grain-boundaries ($\kappa_{Gb} = 3\alpha/r_0$ [63]). With the specific vacancy trapping rate $\mu = 4 \times 10^{14} \text{s}^{-1}$ [61], the grain radius r_0 of 50 nm and a typical specific grain-boundary trapping rate α of 10^4ms^{-1} [27, 102], a vacancy-copper-complex concentration C_{V-Cu} in the order of 5×10^{-4} can be estimated. This vacancy-concentration is similar to the vacancy-concentrations reported for HPT-deformed metals of 10^{-4} , investigated by differential dilatometry [4], differential scanning calorimetry [1, 2] and positron annihilation techniques [129, 130]. The calculated vacancy-concentration of 5×10^{-4} reflects only the copper-stabilised vacancies and does not take into account vacancies attached to dislocations and grain-boundaries.

Influence of HPT on the aging process (isothermal annealing at 193°C)

To investigate the influence of HPT on precipitation phenomena artificial aging at 193°C has been performed. Aging of the undeformed reference sample for 1 hour at 193°C leads to significant changes of the mean positron lifetime (Figure 4.14 and Table 4.6) and the 2d-DB spectra (Figure 4.17 (a)). The strong decrease of the mean positron lifetime from 196 ps to 165 ps upon aging at 193°C for 1h, which is close to the positron lifetime in defect free aluminium, indicates the annealing out of the quenched in vacancies. In addition the local maximum in the 2d-DB spectrum at approximately $10 \times m_0 c \times 10^{-3}$ has vanished (Figure 4.17 (a)), revealing that the vacancies have disappeared. Further the Cu-type signature of the spectrum is significantly reduced (Figure 4.17 (a)), showing that in the proximity of the positron annihilation sites less copper is present. A strong reduction of the copper signature from $w_{Cu_{def}} = 0.22$ to $= 0.06$ (Figure 4.12 (a) and Table 4.5) is also deduced from the numerical analysis of the

2d-DB spectrum. These facts can be attributed to the annealing of the quenched in vacancy-copper complexes at vacancy sinks at dislocations. Since the positron lifetime of multilayer GP-zones is ≈ 167 ps [116] which is similar to bulk aluminium (165 ps), a formation of multilayer GP-zones cannot be deduced by positron lifetimes. The slight remaining copper signature, observed in the 2d-Doppler broadening spectra, may derive from the GP-zones [116]. This is one significant difference to Al-Mg-Cu alloys, where vacancies are stabilised by magnesium even when subjected to higher temperatures (see Lechner et al. [9]).

For the HPT-deformed sample isothermal annealing at 193°C for 1 hour leads to the disappearance of the negative slope in the 2d-DB spectra, associated with the copper environment (Figure 4.17 (a)) at high momenta which is also illustrated by the reduction of the fitting coefficient $w_{Cu_{def}}$ from 0.08 to 0.01 (Figure 4.12 (b) and Table 4.5). Since in addition, XRD investigations (Figure 4.16) clearly reveal the formation of Al₂Cu precipitates as indicated by new peaks, we attribute this behaviour to the formation and coarsening of the equilibrium-type precipitates and to the recovery of the remaining copper associated defects. The mean positron lifetime shows only a minor decrease to 208 ps (Figure 4.14 and Table 4.6), reflecting the annealing of a minor amount of defects. These results lead to the conclusion that the copper-associated defects were annealed out and the positrons are solely trapped at defects free of copper environment.

Prolonged annealing at 193°C

Sustained annealing for up to 290 hours at 193°C of the undeformed reference sample leads to a re-increase of the copper signature as indicated by the ratio curve, presented in Figure 4.17, as well as by spectrum fitting ($w_{Cu_{def}}$ Figure 4.12 (a) and Table 4.5). In addition the mean positron lifetime re-increases with prolonged temperature treatment to approximately 177ps (Figure 4.14 and Table 4.6). Both findings together indicate trapping of positrons at new generated trapping sites with copper environment. This is attributed to the formation of the metastable Θ' -precipitates along with misfit dislocations which act as Cu-decorated positron trapping sites. This is very well supported by electron micrographs presented in Figure 4.13(a2). After annealing for 144h at 193°C,

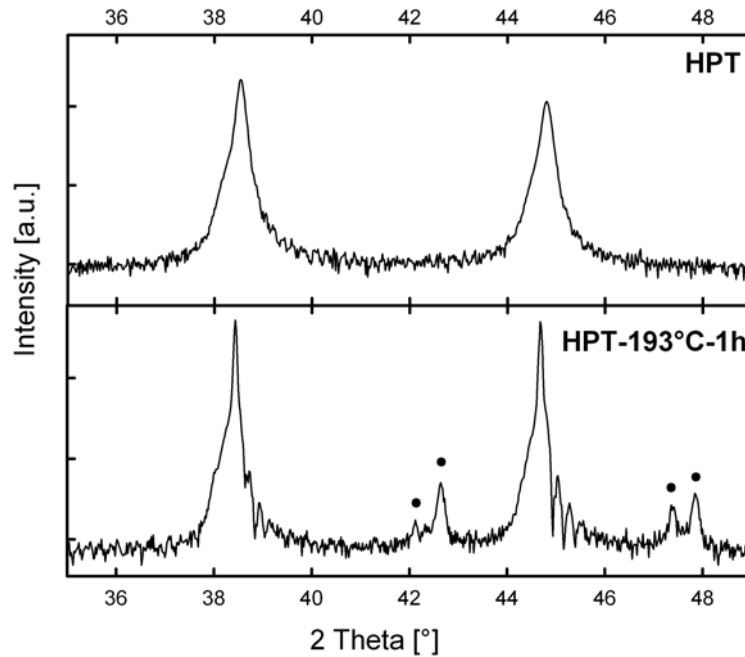


Figure 4.16: X-ray diffraction pattern of the HPT-deformed sample in the as deformed stage and after 1h of annealing at 193°C . Additional reflexes (●), originating from Al_2Cu precipitates, emerge.

platelet shaped precipitates with a length and mean distance of approximately 200nm can be found (Figure 4.13(a2)).

A similar trend upon prolonged annealing of Al-Cu alloys is reported in literature [117, 118, 120, 126]. This positron lifetime of 177ps is in accordance with the positron lifetime of 174ps calculated by Häkkinen et al. [123] for simple dislocations in aluminium and the positron lifetime for positrons trapped within or at misfit dislocations of Θ' -precipitates of 174ps reported by Melikhova et al. [121]. As dislocations in aluminium are known to act as shallow traps [123], it seems that the decoration of the dislocations with copper atoms, which exhibit a higher positron affinity than aluminium [128], increases the binding energy of the positron to the open volume of the dislocation. In fact, an increased positron affinity of the Θ' -precipitates was calculated by Melikhova et al. [121]. Therefore, the conclusion can be drawn, that positrons are effectively trapped at Θ' -misfit dislocations and this type of defect exhibits a positron lifetime of 177ps.

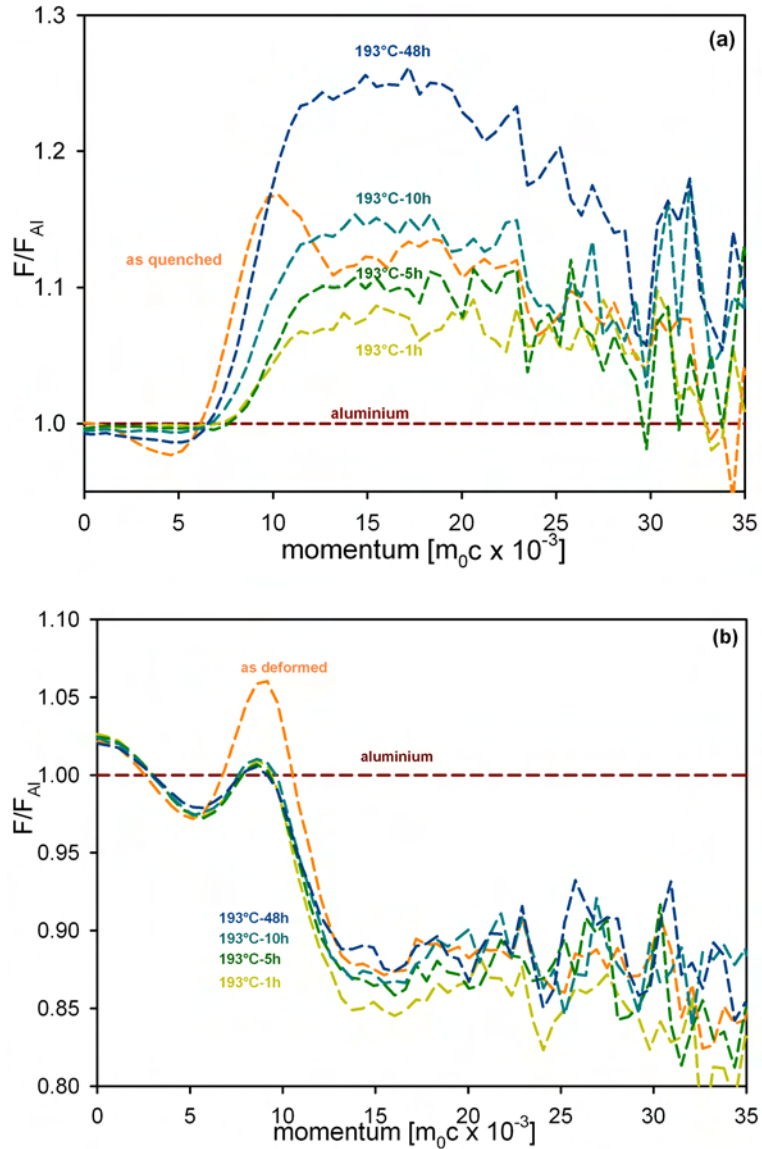


Figure 4.17: 2d-DB Spectra of (a) undeformed and (b) HPT-deformed Al-3wt%Cu samples at different isothermal annealing stages at 193°C. Plotted are the difference ratio spectra with respect to pure aluminium.

The HPT-deformed sample on the other hand, shows a slight evolution of the difference-ratio-curve towards annealed, pure aluminium (Figure 4.17 (b)) upon further annealing at this temperature for up to 290h. This is clearly supported by the DB-spectrum analysis, which shows a significant decrease of the fraction of deformed aluminium from $w_{Al_{def}} = 0.85$ to $w_{Al_{def}} = 0.30$ and the reduction of the copper contribution from $w_{Cu_{def}} = 0.08$ to $w_{Cu_{def}} = 0$ (Figure 4.12 (b) and Table 4.5). A formation of semi-

coherent Θ' -precipitates, which occurs in the undeformed reference sample, is not found in the HPT-deformed sample by TEM (see Figure 4.13(b2)). A steady decrease of the mean positron lifetime can be observed (Figure 4.14 and Table 4.6) as well. A two-term analysis of the positron lifetime spectra reveals a defect lifetime τ_2 of 221-236ps. As the calculated bulk lifetime based on the simple two-state-trapping model gives higher values than 165ps, this defect lifetime of 221-236ps is attributed to be a mixture of different defects such as deformation induced dislocations and grain boundaries. The decrease of the intensity of this positron lifetime reveals the annealing of these types of defects upon prolonged temperature treatment. These changes of the annihilation behaviour can be attributed to the recovery of the deformation induced defects accompanied by starting grain growth.

This is in fact observed by TEM where mean grain sizes in the range of 1 – 2 μ m upon annealing for 144h (Figure 4.13(b2)) can be found. According to TEM investigations (Figure 4.13(b2)) the HPT deformed sample shows the equilibrium-type precipitates at grain boundaries and triple junctions after annealing at 193°C for 144h, whereas the undeformed sample shows platelet shaped semi-coherent precipitates at this annealing stage (compare Figure 4.13 (a2) and (b2)). These Al₂Cu equilibrium Θ -precipitates exhibit a crystallite size between 50 and 200nm as deduced from TEM images. The strongly reduced copper signature, compared to the undeformed reference sample (compare Figure 4.12 and 4.17 (a) and (b), respectively) can be attributed to a larger mean distance of approximately 880nm between the Θ -precipitates, compared to the closely packed Θ' -precipitates of the undeformed reference sample (distance approx. 200nm) as shown in Figure 4.13 (a2). Therefore, positron trapping and annihilation at the Al₂Cu-precipitates or the Al₂Cu-matrix interface is strongly reduced in the HPT-deformed sample as compared to the metastable Θ' -precipitates in the undeformed sample.

Melikhova et al. [121] found that the incoherent Θ -precipitates exhibit a similar positron affinity as the pure aluminium matrix and, therefore, do not act as efficient positron traps. A summarised comparison of the different positron trapping sites for the undeformed and HPT-deformed samples is presented in Figure 4.18. It can be concluded, that in contrast to the undeformed sample upon annealing at 193°C, in the HPT-deformed sample no indications for the formation of semi-coherent Θ' -precipitates are found.

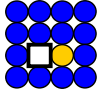

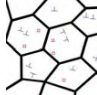

Al-3wt%Cu	undeformed		HPT-deformed	
treatment	quenched	annealed 193°C-72h	quenched + deformed	annealed 193°C-72h
positron traps				
lifetime	196 ps	177ps	211 ps	221 ps

Figure 4.18: Sketch of the dominant positron traps before and after isothermal annealing.

Isochronal annealing

After annealing at 193°C for 120h both HPT-deformed and undeformed samples exhibit a plateau in the mean positron lifetime (Figure 4.14) and the 2d-DB spectra analysis (Figure 4.12 and Table 4.5). This plateau ranges from annealing for 120h up to annealing for 290 hours. Following the isothermal heat treatment, an isochronal annealing for 1 hour at higher temperatures in steps of approximately 30°C was performed.

The 2d-DB spectra of the undeformed sample reveal a decreasing copper signature with increasing temperature. For temperatures above 200°C (Figure 4.19 (a)) a decrease of $w_{Cu_{def}}$ (Figure 4.12 (a) and Table 4.5) is observed. This is accompanied by a continuous decrease of the mean positron lifetime (Figure 4.14 and Table 4.6) and leads to the conclusion that upon annealing at increasing temperatures a decrease of positron trapping at misfit dislocations of the aluminium matrix precipitate interface takes place, as vacancies and vacancy-copper-complexes have already annealed out. This is attributed to the coarsening of the Θ' -precipitates which is supported by electron micrographs (Figure 4.13, (a3)), where an increase in mean size and distance ($\approx 500\text{nm}$) of the Θ' -precipitates can be observed. From 350°C onwards, the transformation of Θ' -precipitates into the incoherent equilibrium Θ -precipitates occurs [121] accompanied with further coarsening, leading to further increase of the mean distance

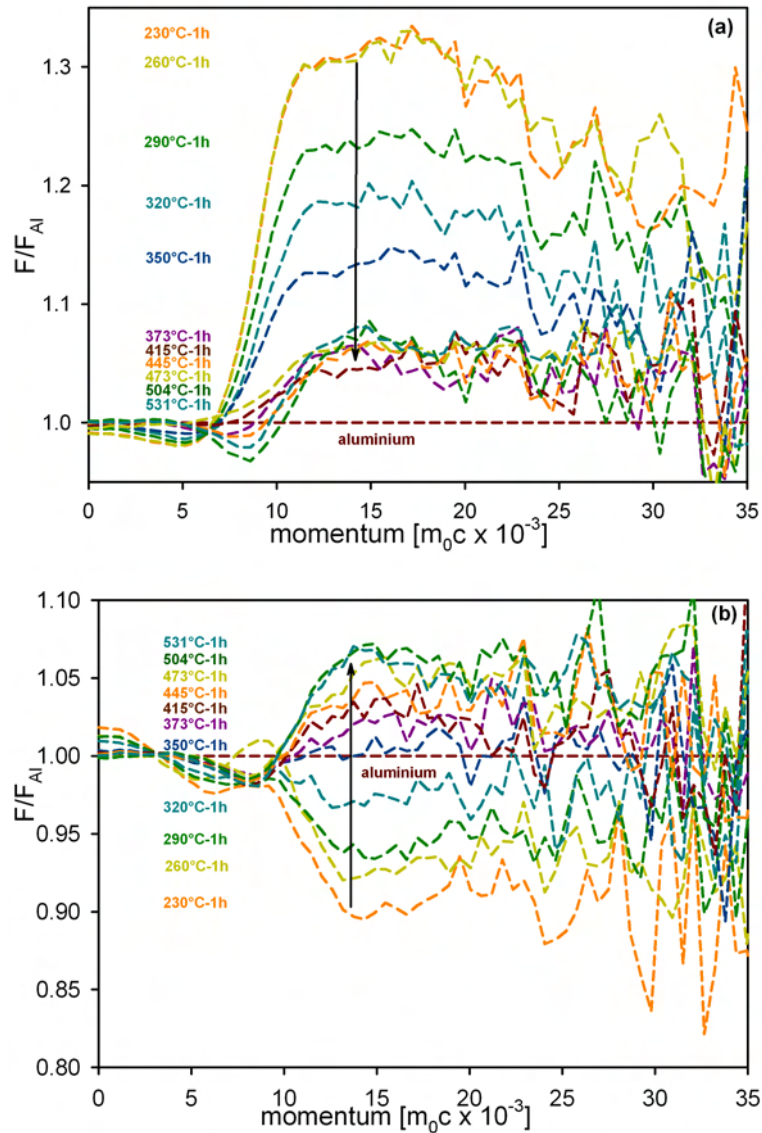


Figure 4.19: 2d-DB spectra of (a) undeformed and (b) HPT-deformed Al-3wt%Cu samples at different isochronal annealing stages for 1 hour. Plotted are the difference ratio spectra with respect to pure aluminium.

of the precipitates. At a temperature of 531°C 2d-DB spectra reveal a minor, but still significant copper signature (Figure 4.12 (a), Table 4.5 and Figure 4.19, 531°C-1h). The remaining copper signature may derive from Guinier-Preston zones. This GP-zones may form during cooling down the samples after heat treatment since precipitates start to dissolve at temperatures at and above 500°C. GP-zones are reported to trap positrons, but exhibit a positron lifetime of about 167ps, which can hardly be

separated from the positron lifetime in bulk aluminium of 165ps.

Utilising the simple trapping model $\bar{\tau} = \tau_f \times \frac{1+\kappa\tau_d}{1+\kappa\tau_f}$ leads to a trapping coefficient κ of about 1.2×10^{10} after annealing at 320°C. By using a trapping rate κ for shallow but extended traps of $\kappa = 4\pi r_d D_+ C$ [127], with r_d the radius of the defect, D_+ the positron diffusion coefficient and C the defect density, the defect density may be calculated. Assuming spherical precipitates with a mean diameter of 500nm (obtained from SEM, Figure 4.13 (a3)) for the undeformed reference sample after annealing at 320°C and a positron diffusion coefficient of $0.8 \text{ cm}^2\text{s}^{-1}$ leads to a calculated precipitate-density of about $2 \times 10^{13} \text{ cm}^{-3}$. As the applied model is valid only for spherical defects, the calculated precipitate density gives an approximation of the order of magnitude of the platelet shaped Θ' -precipitate density.

The 2d-DB spectra of the HPT-deformed sample upon annealing at higher temperatures (up to 350°C) evolve towards pure, defect free aluminium and are after temperature treatment of 350°C almost identical to the pure defect free aluminium spectrum (Figure 4.19 (b)). The numerical analysis reveals a reduction of $w_{Al_{def}}$ to 0 (Figure 4.12 (b) and Table 4.5) while the copper contribution stays $w_{Cu_{def}} = 0$. The decrease of the mean positron lifetime towards the lifetime of defect free aluminium (see Figure 4.14 and Table 4.6) indicates reduced positron trapping due to the annealing of the existing traps. This behaviour is similar to the behaviour of the undeformed sample within the same temperature range and can be attributed to the increase of the mean distance of the positron traps (grain boundaries) due to grain growth, while the Θ -precipitates, present within the HPT-deformed sample are subject to further coarsening and, therefore, do not act as positron traps, due to their increased spacing. Electron micrographs show this coarsening of the Θ -precipitates (Figure 4.13, (b3)) and a further increase of their mean distance to $\approx 1.8\mu\text{m}$. Annealing at 373°C and above leads to a slight but steady increase of $w_{Cu_{def}}$ from 0 to 0.04 (Figure 4.12 (b) and Table 4.5), which equals the $w_{Cu_{def}}$ value of the undeformed reference sample after annealing at 531°C for 1 hour. The similarity of the spectra of the undeformed and HPT deformed specimen, as well as the copper signature is obvious by comparing the spectra of the deformed and undeformed Al-3wt%Cu samples after annealing for

1 hour at 531°C (Figure 4.19, 531°C-1h). In addition the HPT-deformed and undeformed reference sample show similar positron lifetimes from 320°C onwards (Figure 4.14), leading to the conclusion that similar defects are present. A starting dissolution of the equilibrium precipitates at these high temperatures and the formation of metastable phases, most likely Guinier-Preston zones (GP zones), upon cooling down to room temperature is suggested. This conclusion is supported by the calculations of positron lifetimes and 2d-Doppler broadening spectra of Staab et al. [116] and by the fact that the same positron annihilation characteristics occur as for the reference sample after annealing at 193°C for 1 hour (see section 4.1.2).

Integral S&W parameter

The analysis of the Doppler broadening S- and W-parameter, as communicated in the Physics Procedia [104], is in agreement with the results presented above. The influence of the thermal treatment on the shape (S) and wing (W) parameter, deduced from 2d-Doppler broadening spectra, is shown in Figure 4.20. These parameters were plotted with respect to the S_0 and W_0 parameter of well annealed aluminium, indicated by the point at (1, 1). The ageing sequence, discussed above can be clearly deduced as well. Arrow 1 indicates the change due to the first annealing at 193°C for 1 hour. The HPT sample evolves towards pure, deformed aluminium, whereas the undeformed sample evolves towards pure, annealed aluminium. Arrow 2 gives the shift upon the prolonged isothermal annealing at 193°C. While the HPT-deformed sample evolves towards annealed aluminium, the copper signature of the undeformed sample re-increases. Annealing at higher temperatures, indicated by arrow 3, shows the evolution towards pure, annealed aluminium and ends at similar S and W parameter values for both samples.

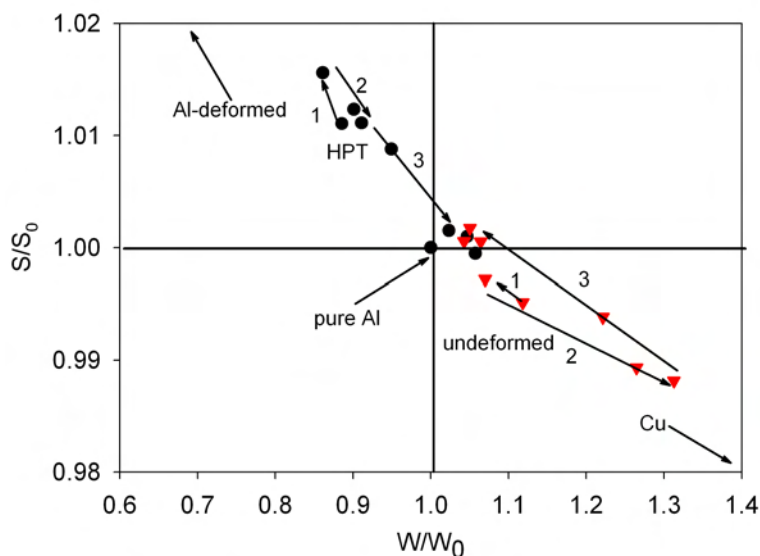


Figure 4.20: S&W parameter plot of Doppler broadening, with respect to S_0 and W_0 of pure, well annealed aluminium (1,1). The locations of deformed copper and deformed aluminium are outside of the plot, indicated by arrows. Red triangles indicate the parameter for the undeformed sample and black circles for the HPT-deformed sample. Arrow 1 shows the evolution of the S&W parameter of the samples upon annealing at 193°C for 1 hour. Arrow 2 shows the evolution upon prolonged annealing at 193°C for up to 290 hours. Annealing at higher temperatures ($\geq 260^\circ\text{C}$) leads to the evolution of the S&W parameter as indicated by arrow 3. After annealing at 373°C for 1 hour almost no further changes can be monitored. Published in Physics Procedia [104].

Summary

The presented analysis of the measured spectra, F-ratio-plot, numerical analysis and S-W-plot provide a self consistent picture of the chemical environment of the positron trapping sites. A reduced copper environment of the trapping sites for the HPT-deformed sample was revealed (Figure 4.10, Figure 4.12), due to primary trapping of positrons at deformation induced open volume defects as dislocations and grain boundaries. Upon ageing, the minor copper signature disappears, leaving only copper free defects as grain boundaries and dislocations. From TEM micrographs the formation of

the equilibrium Al_2Cu precipitates can be clearly identified (Figure 4.13 (b)). Ageing leads to a continuous evolution of both the mean positron lifetime, and the 2d-DB spectra, towards pure, annealed aluminium (Figure 4.14, Figure 4.12 (b) and Figure 4.17). At temperatures higher than 350°C the HPT deformed and undeformed sample exhibit the same mean positron lifetime, as well as very similar 2d-DB spectra, leading to the conclusion, that a similar state has been obtained (Figure 4.19 and Figure 4.20). Regarding the influence of HPT, the following conclusions can be drawn from the present combined studies of positron lifetime, 2d-Doppler-broadening and electron microscopy.

1. HPT-deformation is capable to refine Al-Cu alloys down to crystallite sizes of about 100nm, due to stabilisation by precipitation.
2. Trapping of positrons in the HPT-deformed sample occurs mainly at grain boundaries and deformation induced dislocations in contrast to the undeformed sample, where positrons are solely trapped at copper decorated defects.
3. HPT-deformation of a solution treated and quenched Al-3wt%Cu alloy leads to the formation of the equilibrium Al_2Cu precipitates at room temperature.
4. Trapping at the equilibrium Θ precipitates could not be monitored.
5. During aging, no detectable amount of semi-coherent Θ' -precipitates are formed in the HPT-deformed sample, leading to the conclusion that almost the whole copper is already accumulated in the equilibrium precipitates.
6. Upon annealing at and above 350°C , the HPT-deformed and undeformed reference sample exhibit the same mean positron lifetime and 2d-DB spectra. Therefore a similar state is reached.
7. Indications for starting dissolution of the equilibrium Θ -precipitates at temperatures as high as 400°C and formation of Guinier-Preston zones while cooling down were found.
8. In general, the copper signature in the HPT-deformed sample is strongly reduced.
9. A positron lifetime of 177 ps is attributed to positron trapping at copper decorated misfit dislocations between the aluminium matrix and the Θ' -precipitates.

4.1.3 Iron-Nickel meteorite

In this section, positron trapping at precipitates within an iron-nickel meteorite is discussed. The results have recently been presented at the International Conference on Positron Annihilation (ICPA-16) in Bristol and were accepted for publication in the Physics Procedia [132]. The initial question was, whether carbon precipitates exist within the meteorite, as supposed by Weller and Wegst [131] and which would indicate thermodynamic equilibrium. These carbon precipitates should dissolve at about 676°C [131]. It is well known and was also shown already in section 4.1.2 that positrons are sensitive to misfit dislocations.

SEM imaging was performed by Herbert Reingruber (Austrian Centre for Electron Microscopy and Nanoanalysis). Sample preparation, positron lifetime and 2d-Doppler broadening measurements, interpretation and discussion of the results were performed within the scope of the baccalaureats thesis of Matthias Leitner [133] under the co-supervision of the author. Manuscript composition was performed by the author.

Preparation

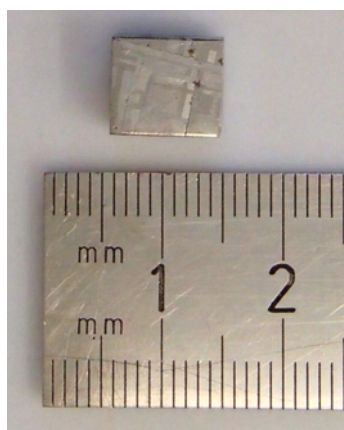


Figure 4.21: Gibeon meteorite sample after etching. The Widmanstätten pattern can be seen.

The investigated sample stems from an iron-meteorite, the so-called Gibeon meteorite. This meteorite was found near the city of Gibeon in Namibia, Africa. While entering

earth's atmosphere it broke into several thousand smaller parts, which were scattered on an area of approximately 370x185 km. Up to now about 26 tons of materials were collected. During its travel through space the meteorite was subject to very low cooling rates, of approximately 35°C per one million years[134]. This unique cooling rates are the reason for the typical Widmanstätten structure, a two-phase microstructure of Fe-rich Kamacite (ferrite, α -iron) and Ni-rich Taenite (austenite, γ -iron). The composition of the meteorite was Fe 91.62 wt%, Ni 7.93 wt%, Co 0.41 wt%, P 0.04 wt% and small amounts of carbon[135]. For the positron investigation two pieces of approximately $8 \times 8 \times 3 \text{ mm}^3$ were cut with a low-speed diamond saw from a larger chunk.

Results

Initial Condition

After polishing and etching the meteorite sample shows the typical Widmanstätten structure in the mm range observable by the naked eye. Broad Ni-poor Kamacite bars are separated from areas of fine-grained Kamacite and Taenite by narrow bands of Ni-rich Taenite, as shown in Figure 4.22 (a) and (b). Positron lifetime measurements reveal a relatively high mean positron lifetime of $\bar{\tau} = 165\text{ps}$. Compared to the positron lifetime in defect free iron, $\tau_f = 110\text{ps}$ [90], this shows that open volume defects are present in the meteorite sample. The lifetime of 165ps is too short for vacancies in iron. Typically vacancies in pure iron exhibit a positron lifetime of $\tau_v = 175\text{ps}$ [90]. In addition, vacancy-carbon complexes, which are reported to exhibit a positron lifetime of about 165ps, anneal out at about 80°C [90, 91]. Therefore, no remaining vacancies or vacancy-carbon-complexes are expected to be present in the meteorite sample, due to the slow cooling of the meteorite in space. This leads to the conclusion, that the positron traps in the meteorite sample are mainly dislocations. In fact dislocations in iron are reported to exhibit a positron lifetime of $\tau_d \approx 160\text{ps}$ [92, 93]. In Figure 4.23 2d-Doppler broadening spectra of the meteorite sample and its major composition elements, namely pure iron, defected iron, defected nickel and carbon are shown with respect to pure annealed iron.

In Figure 4.23 a comparison of the 2d-Doppler broadening spectra of the meteorite sample and defected iron, defected nickel and carbon with respect to defect free iron

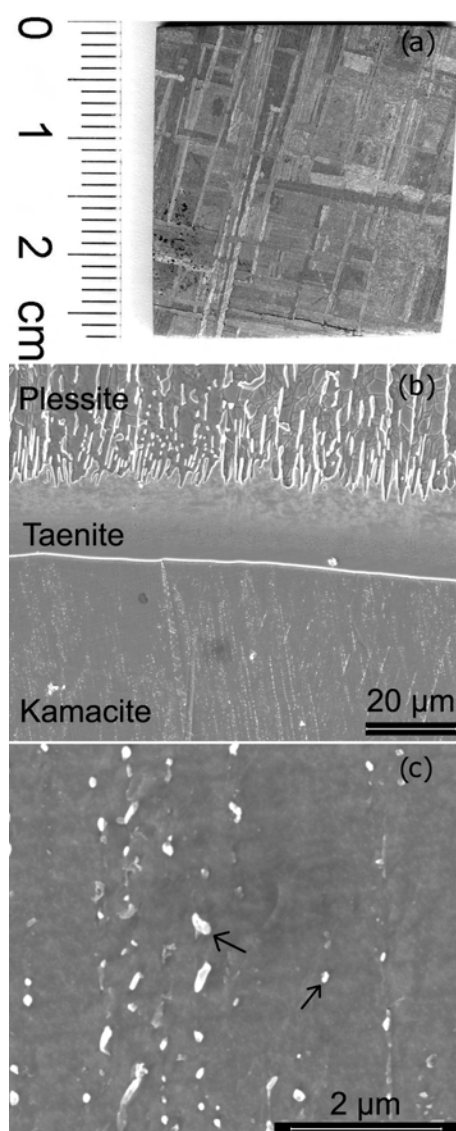


Figure 4.22: (a) Optical micrograph of the Widmanstätten structure of the meteorite sample. (b) SEM micrograph of the phase boundaries between Taenite, Kamacite and Plessite. (c) Close up of nickel rich precipitates (arrows) within Kamacite bars.

is presented. A relative strong similarity to defected nickel can be observed, which indicates positron trapping at nickel decorated defects.

The meteorite 2d-DB spectra were also fitted with linear combinations of the momentum distributions of pure annealed iron, defected iron, defected nickel and carbon

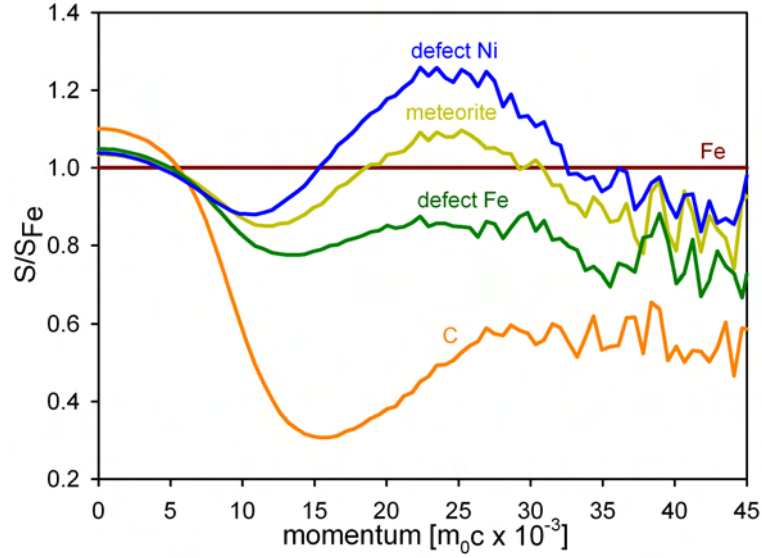


Figure 4.23: Comparison of 2d-Doppler broadening spectra of deformed iron, pure and annealed iron, meteorite sample, pyrolythic carbon and pure, deformed nickel. Plotted are the ratio spectra with respect to pure and annealed iron.

Table 4.8: Weighting fractions obtained by fitting the measured spectra according to equation 4.5.

temperature	w_{Fe}	$w_{Fe_{defect}}$	w_{Ni}	$w_{Ni_{defect}}$	w_C
20°C	0.24	0.02	0	0.62	0.12

according to equation 3.5, leading to the following equation:

$$F = F_{Fe} \times w_{Fe} + F_{Ni} \times w_{Ni} + F_C \times w_C + F_{Fe_{defect}} \times w_{Fe_{defect}} + F_{Ni_{defect}} \times w_{Ni_{defect}} \quad (4.5)$$

In Table 4.8 the calculated contributions for the meteorite sample are presented. First, a large defect-nickel signature is observed. This indicates that defects with a strong nickel environment are present. As these defects are identified to be dislocations from positron lifetime measurements, misfit dislocations between the Ni-rich Taenite and Ni-poor Kamacite are present. Electron micrographs reveal that within the broad Ni-poor Kamacite bars small Ni-rich precipitates with a diameter of $\approx 200nm$ are present (see Figure 4.22(c)). Therefore, it can be concluded that at the interface between matrix

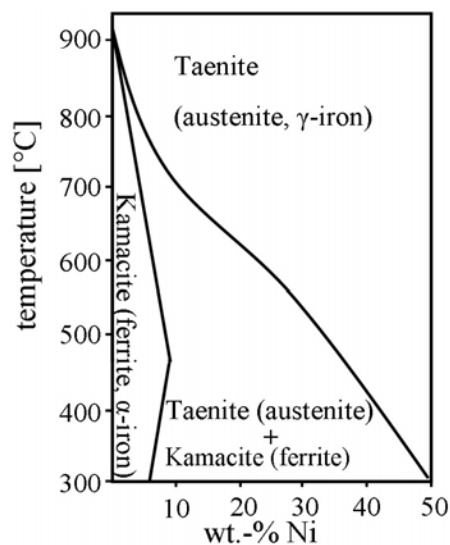


Figure 4.24: Iron rich section of the iron-nickel phase diagram, redrawn after Swartzendruber et al. [137].

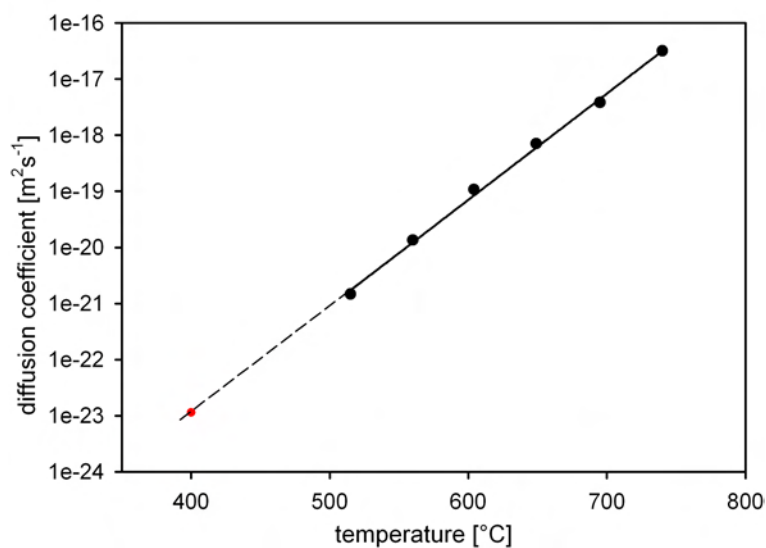


Figure 4.25: Extrapolation of diffusion coefficient of nickel within iron matrix. Data from Cermak et al. [138].

and precipitates misfit dislocations are introduced. In fact, the cubic body-centred Kamacite exhibits a lattice parameter of $a = 0.286 \text{ nm}$ [136] and the cubic face-centred Ni-rich Taenite exhibits a lattice parameter of $a = 0.358 \text{ nm}$ [136].

Furthermore, according to the phase diagram (Figure 4.24) the nickel content of the

Kamacite decreases by about 4 wt% after reaching a maximum solubility at about 460°C and due to the low cooling rates of $35 \times 10^{-6} \text{Ka}^{-1}$ and an extrapolated nickel diffusion coefficient (data from Cermak et al. [138]) of $D \approx 1 \times 10^{-23} \text{m}^2 \text{s}^{-1}$ at 400°C a diffusion length of the nickel atoms of $\approx 3.6 \times 10^{-2} \mu\text{m}$ per year can be estimated (see Figure 4.25). Therefore, Ni-rich precipitates have to be formed during the slow cooling down, due to an average width of the Kamacite bars of about 500 μm . In fact, the misfit dislocations between the Taenite precipitates and the Kamacite matrix are detected by positrons. The precipitates are also confirmed by electron microscopy (Figure 4.22(c)). Nowell et al. [139] reported the existence of small nickel-rich precipitates with diameters down to 80nm, found by electron micrographs, as well. In addition the numerical analysis of the 2d-DB spectra reveals a minor but detectable carbon signature (Table 4.8). This shows that positrons are as well trapped at carbon precipitates within the meteorite sample. The existence of carbon precipitates within the meteorite was proposed by Weller and Wegst [131] from internal friction experiments.

Isothermal annealing

The meteorite samples were then subjected to subsequent isochronal thermal treatment for one hour at 400°C, 500°C, 600°C, 676°C and 900°C. The evolution of the mean positron lifetime is presented in Figure 4.26.

In Figure 4.27 the S- and W-parameter, obtained from 2d-Doppler broadening experiments are shown. Upon annealing three distinct annealing stages can be observed from both Figures 4.26 and 4.27. First, up to 400°C, a minor decrease of the mean positron lifetime can be observed, while the results of the Doppler broadening S- and W-parameter show no decrease of the S-parameter (Figure 4.27 and Figure 4.29) in this temperature region. The W-parameter (Figure 4.27 and 4.29) on the other hand shows a pronounced decrease. In addition with the numerical analysis of the 2d-DB spectra (Figure 4.28 and Table 4.9) following conclusions can be drawn. Upon this temperature step the chemical environment of the open volume defects changes, as the dissolvable nickel content of the Kamacite is increasing in this temperature region (see Figure 4.24). The nickel signature at the defects decreases slightly (see Table 4.9 and Figure 4.28), while the misfit dislocations persist. The nickel diffusion length in Fe at this temperature for one hour is approximately 0.2 nm, which is in the range of 1 lattice constant, allowing nickel to leave the proximity of the misfit dislocation. This

Table 4.9: Weighting fractions obtained by fitting the measured spectra according to equation 4.5.

temperature	w_{Fe}	$w_{Fe_{HPT}}$	w_{Ni}	$w_{Ni_{HPT}}$	w_C
20°C	0.24	0.02	0	0.62	0.12
400°C	0.30	0.13	0	0.47	0.10
500°C	0.44	0	0	0.44	0.12
600°C	0.71	0	0	0.26	0.03
676°C	0.69	0.13	0.14	0.04	0
900°C	0.68	0	0	0.27	0.05

change of the chemical environment is as well attributed to lead to the slight decrease of the mean positron lifetime.

At higher temperatures, stage II, between 450°C and 680°C, the defects start to disappear, which is indicated by the strong decrease of the mean positron lifetime (Figure 4.26) while at the same temperatures the S-Parameter (Figure 4.27 and 4.29) decreases rapidly as well. In addition the chemical sensitive 2d-DB spectra reveal a major in-

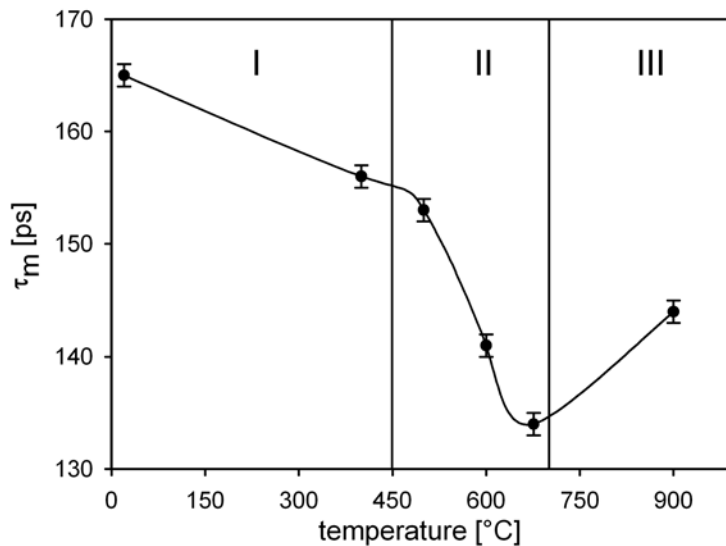


Figure 4.26: Mean positron lifetime of meteorite sample upon isochronal annealing (1h) at different temperatures. Three distinct stages can be identified. Line is guide to the eye. Published in Physics Procedia [132].

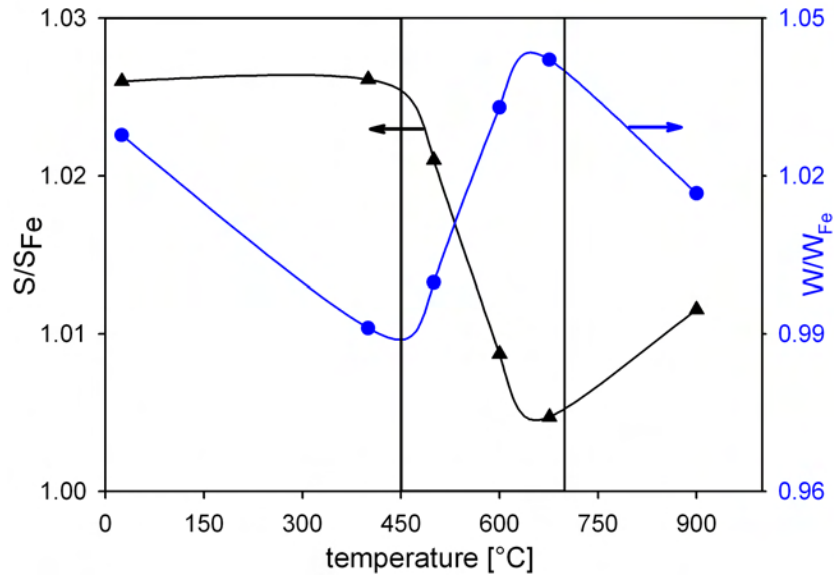


Figure 4.27: S&W parameter plots of Doppler broadening in dependence of annealing temperature, with respect to S_0 and W_0 of pure, well annealed iron. Published in Physics Procedia [132].

crease of the pure iron signature, while the defect nickel signature decreases strongly and the defect iron signature decreases as well (Figure 4.28 and Table 4.9). Starting at temperatures higher than 500°C the carbon signature of the meteorite sample decreases and disappears at 676°C (Figure 4.28 and Table 4.9). This leads to the conclusion, that carbon containing precipitates were dissolved at this temperature and the carbon now occupies interstitial sites and is not detectable by the positrons any more. The dissolution of carbon precipitates in a Fe-Ni meteorite at this temperature has in fact also been reported by Weller and Wegst [131], from internal friction experiments.

In stage III, at temperatures higher than 676°C, a re-increase of the mean positron lifetime (Figure 4.26), as well as the S-parameter and a decrease of the W-parameter (Figure 4.27) is observed, indicating the formation of new open volume defects in this temperature range. This behaviour and an increased contribution of the defect nickel signature of the fitting process (Figure 4.28 and Table 4.9) indicate that vacancy-type defects are formed and stabilised by impurity atoms such as nickel or carbon. Shirai et al. [140] showed the increasing formation of thermal vacancies in pure iron between 797°C and 911°C.

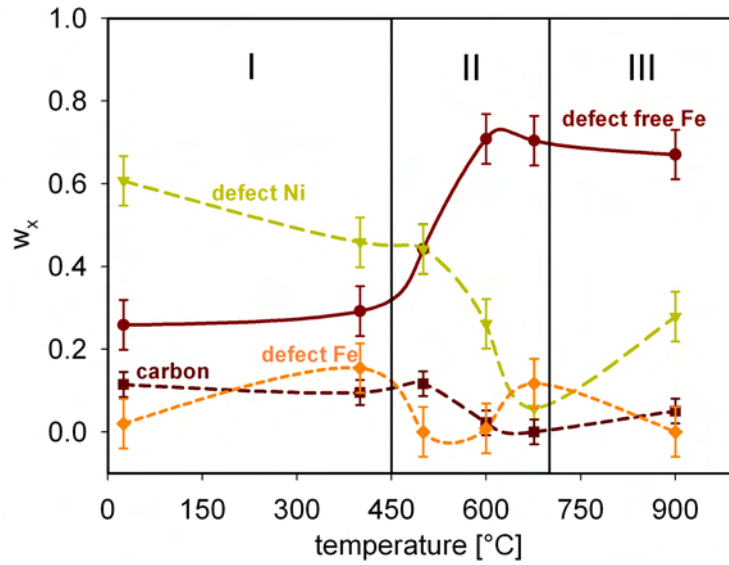


Figure 4.28: Evolution of the 2d-Doppler broadening fit parameter w_x as function of the annealing temperature. Lines are guide to the eye. Published in Physics Procedia [132].

In addition, after annealing at 900°C, no indication for precipitates within the Kamacite could be found by SEM (see Figure 4.30).

In Figure 4.31 the evolution of the 2d-DB spectra of the meteorite sample with increasing temperatures is presented. Up to temperatures of 676°C, a continuous increasing similarity to pure iron can be clearly observed, while after annealing at 900°C a deviation from this trend is found.

More detailed analysis of the positron lifetimes according to the trapping model could not be performed due to the existence of different defect types present in the sample, which could not be separated, such as misfit dislocations between the Kamacite and Taenite, as well as misfit dislocations at carbon precipitates. At high temperatures, the increase of the S-parameter and $\bar{\tau}$ clearly reveal the formation of additional defects, such as vacancy-impurity. As all of the positron lifetimes of these defects are expected to be within 10ps to 20ps around 160ps, these defects can not be separated.

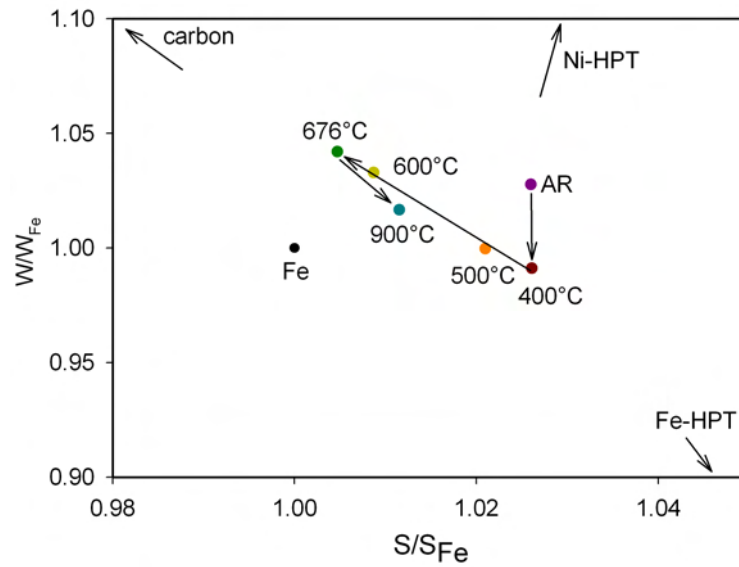


Figure 4.29: Evolution of the S and W parameter of the meteorite sample upon isochronal (1h) temperature treatment with respect to the S_0 and W_0 of well annealed pure iron.

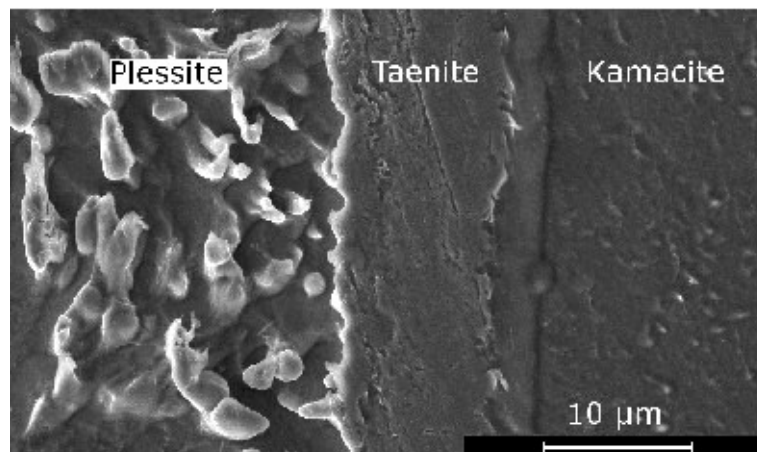


Figure 4.30: Electron micrograph of the meteorite sample after annealing at 900°C for 1 hour. The Widmanstätten pattern is still visible, but the precipitates within the Kamacite bars have vanished. Published in Physics Procedia [132].

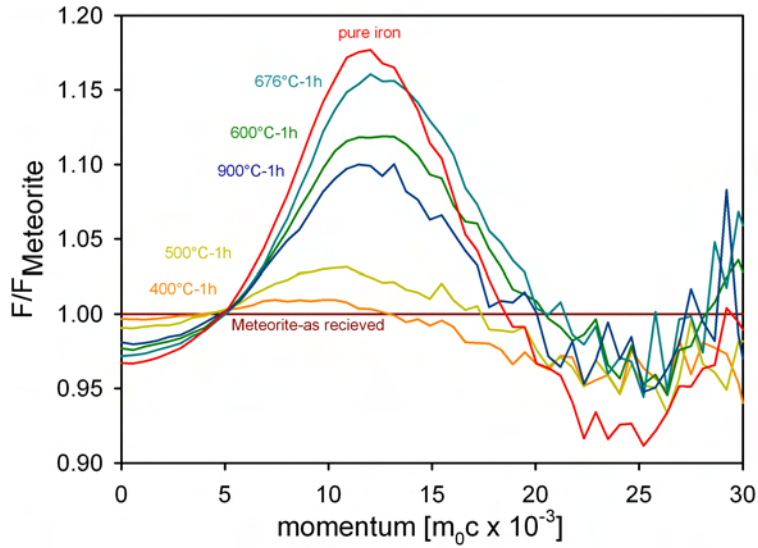


Figure 4.31: Evolution of the 2d-DB spectra of the meteorite sample upon isochronal (1h) temperature treatment with respect to the not thermal treated meteorite.

Summary

It was shown, that the meteorite sample is in a stable thermodynamic equilibrium condition with respect to a) thermal vacancies and b) carbon precipitates. The existence of carbon precipitates within the Gibeon meteorite, suggested by Weller et al. [131] could be confirmed by positron annihilation spectroscopy, as well as their dissolution at about 676°C. In addition, a mean positron lifetime of $\bar{\tau} = 165\text{ps}$ implies the existence of open volume defects. This positron lifetime is similar to positron lifetimes reported for dislocations in iron [90, 92]. Due to the stability of this lifetime component up to temperatures of 400°C, vacancy-carbon complexes can be ruled out, as they are reported to anneal out at about 80°C [90, 91] whereas vacancies in iron anneal out at about -50°C [90, 91]. By electron micrographs nickel rich precipitates with a diameter of 200nm could be identified. However, the structure of the meteorite formed upon the slow cooling exhibits the macroscopic Widmanstätten structure and c) small Ni-rich equilibrium precipitates due to the thermal decomposition of the super saturated Kamacite at low temperatures. The positron annihilation techniques give a comprehensive picture of the open volume defects in the meteorite sample.

4.1.4 Discussion

Severe plastic deformation is a valuable tool to produce bulk nanostructured materials with outstanding properties. To understand the changed properties of nanostructured materials, detailed knowledge about the defect types and concentrations is necessary as well as the influence of temperature treatment.

- In iron samples (see section 4.1.1) of different purities, the influence of impurities on the effect of HPT was investigated. It could be revealed, that even minor impurities give rise to increased grain refinement upon deformation. Further the existence of different types of open volume defects such as dislocations, grain boundaries and voids, introduced by HPT, were shown by positron annihilation lifetime spectroscopy. Both samples show positron trapping at grain boundaries and dislocations, but while in the pure iron sample, vacancies form voids in the size of 6 vacancies, in ARMCO iron vacancy-carbon-complexes are found to be present at grain boundaries. These complexes at grain boundaries are stable up to temperatures of 725°C. Overall, defect annealing and recrystallisation of the less pure ARMCO iron are shifted to higher temperatures by about 100°C.

- In solution treated Al-Cu (section 4.1.2), HPT deformation leads to the formation of the equilibrium Θ -precipitates at room temperature. Upon temperature treatment, remaining vacancy-copper complexes are annealed out, and positrons are trapped at grain boundaries and dislocations. The Θ -precipitates stabilise the grain in the 100 nm region and inhibit the dynamic recrystallisation typically occurring in severely plastically deformed aluminium. At temperatures as high as 350°C the differences between an undeformed reference sample and the HPT deformed sample vanish and similar annealing stages are obtained. At annealing temperatures above 415°C, the formation of GP zones or GP-II zones was indicated by a slight but consistent copper signature of the Doppler broadening experiments. A decreased trapping of positrons at copper decorated defects in the deformed sample was found. No evidence for positron trapping within the equilibrium Θ -precipitates could be found. In addition the undeformed sample revealed the positron lifetime of copper decorated Θ' -aluminium matrix interface misfit dislocations to account to 177ps.

- In the iron-nickel meteorite sample (section 4.1.3), different types of equilibrium precipitates could be revealed by the positron annihilation techniques. First, carbon precipitates in the meteorite could be identified by Doppler broadening measurement. This precipitates dissolve at temperatures of about 676°C. Second, nickel rich precipitates were found to exist in the nickel poor Kamacite bars of the Widmanstätten structure. This precipitates were formed while the meteorite initially cooled down and the Widmanstätten structure was formed. At temperatures lower than 450°C, in Kamacite less nickel can be dissolved. The excess nickel forms small precipitates due to the decreased nickel diffusion at these temperatures. This precipitates are dissolved again, when the meteorite sample is re-heated to temperatures of higher than 500°C.

Overall it could be shown, that positron annihilation techniques give valuable insights into defects introduced by severe plastic deformation as well as into the annealing characteristics. The defect annealing characteristics were shown to alter significantly with sample purity, not only by a shift to higher temperatures, but as well as the formation of different types of defects upon temperature treatment. By 2-dimensional Doppler broadening experiments it could be shown, that impurity decorated dislocations are capable to trap positrons, whereas dislocations in pure metals typically are only shallow traps, which do not trap positrons at room temperature.

4.2 Open volume defects in oxides

Lithium-ion batteries have recently developed into the most advanced battery technology. Light weight and high capacity are basic characteristics, needed for future electrification of individual mobility. Therefore, these materials are of high interest, but degradation mechanisms due to electrochemical removal and re-introduction of Li^+ are poorly understood. To enlighten the influence of open volumes to degradation in the course of use, three common representatives as LiCoO_2 , LiMn_2O_4 and $\text{Li}(\text{Mn}_{1/3}\text{Co}_{1/3}\text{Ni}_{1/3})\text{O}_2$ were investigated. These metal oxides are capable to reversibly intercalate and de-intercalate lithium-ions and are, therefore, suitable for the use in battery applications.

4.2.1 Sample preparation

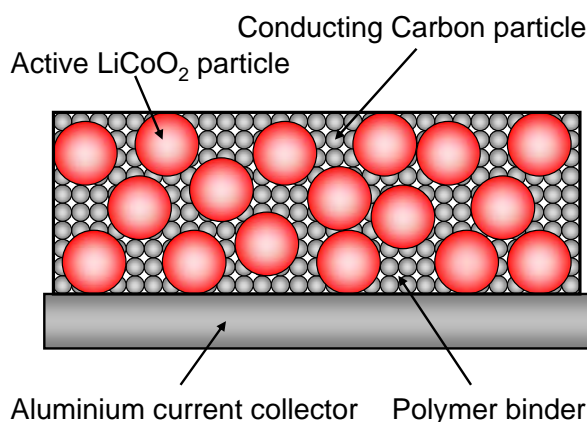


Figure 4.32: Sketch of the typical composition of LiCoO_2 electrodes.

The investigated Li-ion battery cathodes were prepared by Bernd Fuchsichler and Christian Baumann (VARTA Micro Innovations GmbH). For the three different electrode materials an electrode slurry, composed of 88 wt% of the active electrode material, carbon black (Super P) as conducting agent and a polymer binder (polyvinylidene difluoride hexafluoropropylene copolymer) was mixed. The detailed composition of the electrodes is given in Table 4.10. The electrode slurry was prepared via an optimized dispersing technique and coated on an aluminium foil as current collector and finally

Table 4.10: Composition of the three different lithium-ion battery cathodes.

active material	conducting agent	polymer binder
LiCoO_2	7 wt%	5 wt%
LiMn_2O_4	5 wt%	7 wt%
$\text{Li}(\text{Co}_{1/3}\text{Mn}_{1/3}\text{Ni}_{1/3})\text{O}_2$	7 wt%	5 wt%

dried (see Figure 4.32 and Figure 4.33). All electrochemical tests were performed as described in section 3.2.2.

4.2.2 LiCoO_2

Parts of the measurements on LiCoO_2 have been published in Applied Physics Letters [141]. Sample preparation (electrode fabrication and electrochemical lithium extraction) and SEM imaging were performed by Stefan Koller, Bernd Fuchsbichler and Christian Baumann (VARTA Micro Innovations GmbH), X-ray diffraction and Rietveld refinement by Brigitte Bitschnau and Franz-Andreas Mautner (working group spectroscopy and electrochemistry of the Institute of Physical and Theoretical Chemistry, TU Graz). Positron lifetime and 2d-Doppler broadening measurements, interpretation and discussion of the results, as well as predominant manuscript composition were performed by the author.

LiCoO_2 is a typical intercalation battery electrode material. However, these types of materials are subject to performance losses and electrode degradation in the course of their use. Reversible charge/discharge cycling of LiCoO_2 is only possible to 50% of the available Li-ions [142] since further removal of Li-ions drastically reduces the capacity and structural stability upon charge/discharge cycling. To improve the stability of the electrodes upon repeated discharge at higher voltages, various approaches as coating of LiCoO_2 particles [44–46] or substituting of Co partly with other transition metals [47, 48], as e.g. Ni or Mn are currently investigated. Structure sensitive methods such as X-ray diffraction [14, 15], electron microscopy [17], and neutron diffraction [18, 143] have been used to investigate Li-ion batteries and their degradation mechanisms. Upon charging and discharging lithium-ion batteries vast amounts of open volumes are in-

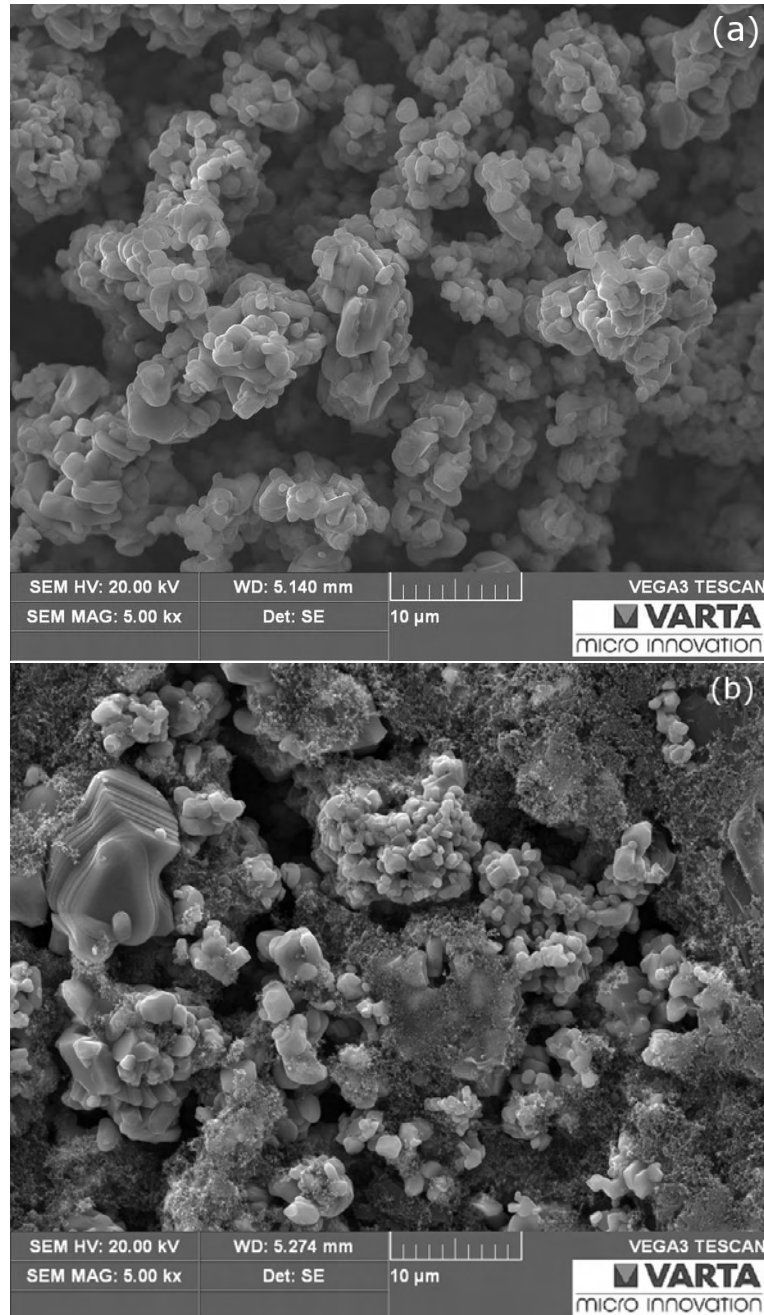


Figure 4.33: Electron micrographs of (a) pure LiCoO_2 -powder and (b) electrode assembly with carbon and binder. Typical particle sizes of 1 - 10 μm can be found.

roduced into the electrode materials and, therefore, detailed knowledge on the atomic order and defect structure produced by Li^+ -extraction might give additional insights into processes taking place during charging/discharging Li-ion batteries. Positron annihilation techniques exhibit a sensitive way to investigate these open volumes.

Results

In section 3 it was shown, that some corrections have to be performed to eliminate the influence of the supporting material and determine the positron annihilation parameter for the relative thin cathode material. Due to a limited number of samples, measurements had to be performed in setup D (see section 3, preliminary measurements, page 26). By utilising an aluminium support instead of the iron support, a correction value of 33% with a positron lifetime of pure aluminium (165ps) was added to the source correction. The influence of the increased source correction on the positron lifetime analysis was investigated. The results of τ_1 of a two component analysis of the measured spectra (b) with and (a) without the subtraction of the increased source correction are presented in Figure 4.34. As can be deduced from Figure 4.34 (a) and (b) only minor influences on the positron lifetime values are caused by the performed correction. However, it has to be mentioned, that the variance of the fit for a two component analysis, which is a measure for the validity of the applied model, without the increased corrections is high and indicates an additional positron lifetime component in the measured spectrum. A three component analysis reveals the existence of a short lifetime component between 150 and 190 ps, which clearly can be attributed to originate from the aluminium support ($\tau_{Al} = 165\text{ps}$). With the correction, a two term analysis of the spectra gives a variance in the acceptable range. The correction can be omitted for the 2d-Doppler broadening spectra, since only relative variations of the integral S- and W-parameter are of relevance.

After proving the feasibility and reliability of the performed measurements the results are presented in the following. To investigate the major influences of the electrode composition to the positron lifetime, measurements on a pure LiCoO_2 powder sample and on a fully lithiated electrode sample have been performed.

A two-term analysis of the fully lithiated electrode material reveals a dominant positron

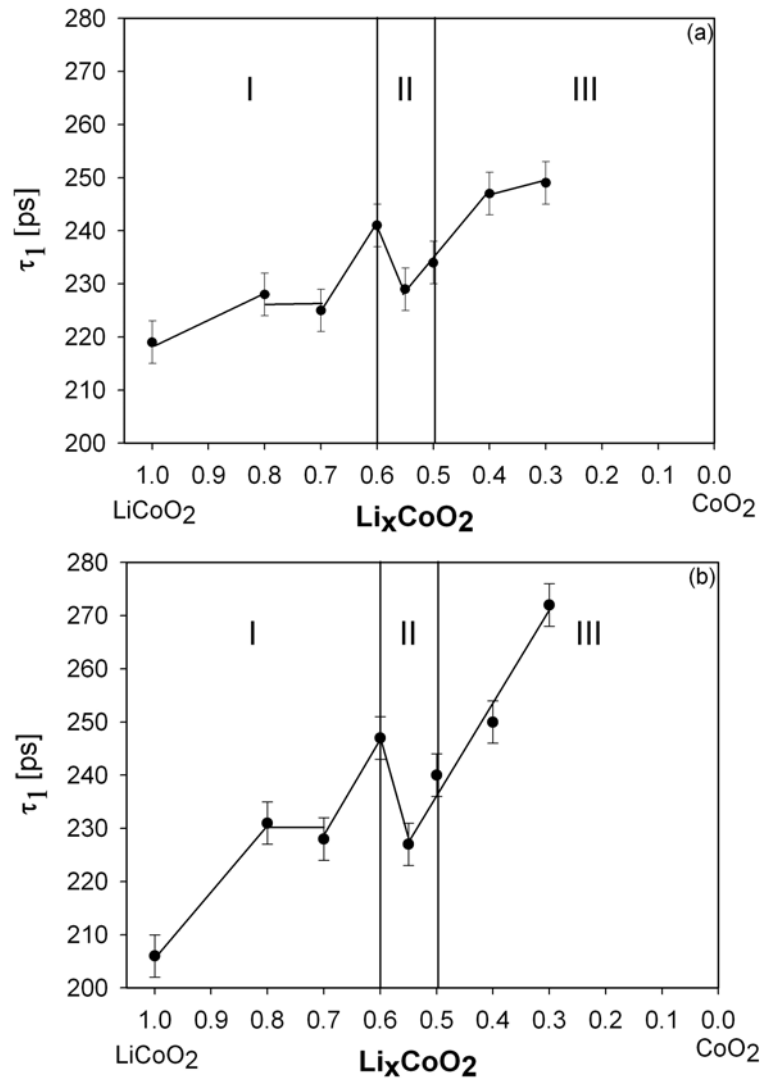
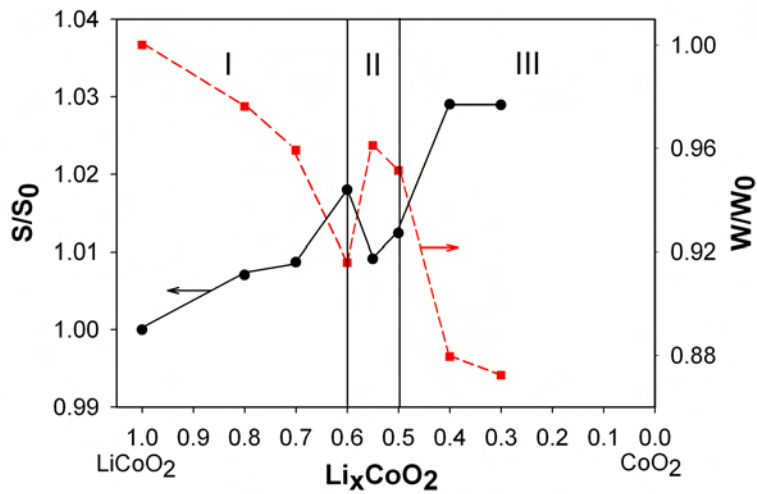


Figure 4.34: Positron lifetime of LiCoO_2 -electrodes with different Li^+ -content. (a) Positron lifetime without correction for the supporting aluminium layer (b) Positron lifetime with correction for the supporting aluminium layer. See Figure 3.12 and discussion in this chapter.

lifetime of 206ps with an intensity of 82.3% and a second positron lifetime of 476ps with a relative intensity of 17.7%. The longer second lifetime component can be attributed to annihilations on LiCoO_2 particle surfaces and to annihilations within carbon and the polymer binder between the LiCoO_2 particles (see Figure 4.33). This longer, second positron lifetime from annihilation on particle surfaces is a typical feature found in compressed powder samples [144]. The dominant lifetime component τ_1 is attributed

Table 4.11: Comparison of positron lifetimes and relative intensities of a LiCoO_2 -powder sample and the LiCoO_2 -electrode.

sample	τ_1 (± 2)[ps]	τ_2 (± 4)[ps]	I_1	I_2
LiCoO_2 -electrode	206 (± 2)	476 (± 6)	82.3	17.7
LiCoO_2 -powder	207 (± 2)	443 (± 6)	87.5	12.5


 Figure 4.35: Normalized S&W parameter plots of 2d-Doppler broadening as function of the Li^+ -extraction, with respect to S_0 and W_0 of fully lithiated LiCoO_2 .

to positron annihilation within the LiCoO_2 particles. This interpretation is supported by the dominant positron lifetime τ_1 of 207ps, measured on a compressed pure LiCoO_2 powder sample (see Table 4.11).

In Figure 4.35 the S- and W-parameter obtained from 2d-Doppler broadening experiments are presented, while Figure 4.36 shows the dominant positron lifetime τ_1 and the lattice parameter in c-direction of the hexagonal phase deduced by XRD. This structural analysis follows the procedure presented in literature, where the rhombohedral structure of LiCoO_2 with a superstructure in [111]-direction is mapped onto a hexagonal unit cell [14, 15, 37]. The linear increase of the lattice parameter c upon Li^+ -extraction is well documented in literature and can be attributed to an increasing Coulomb repulsion of the CoO_2 -groups with decreasing Li^+ -content [14, 15, 18]. The excellent agreement of the measured lattice constant values with literature data [15]

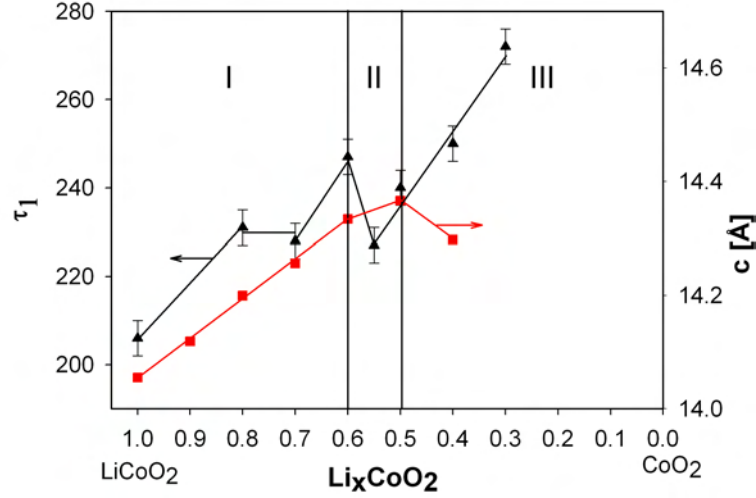


Figure 4.36: Evolution of positron lifetime τ_1 (black triangles) and c -parameter from XRD measurements (red squares) as function of Li^+ -content.

Table 4.12: Positron lifetimes τ_1 ($\pm 2\text{ps}$) of Li_xCoO_2 -electrodes in dependence of Li^+ -content x .

Li^+ -concentration x	1	0.8	0.7	0.6	0.55	0.5	0.4	0.3
τ_1 [ps]	206	231	228	247	227	240	250	272

demonstrates the reliability of the electrochemical Li^+ -extraction for sample preparation. The decrease of the lattice constant c at Li^+ -contents ≤ 0.5 is as well supported in literature [15, 18].

From the S -parameter plot (Figure 4.35) as well as from the positron lifetime data (Figure 4.36 and Table 4.12) three distinct stages can be deduced. At first, at a Li^+ -content between 1 and 0.6 (Stage I), an increase of the S -parameter as well as the positron lifetime τ_1 can be observed. Second, between Li^+ -contents of 0.6 to 0.5 (Stage II), a decrease of the S -parameter and τ_1 , followed by a re-increase is found. At Li^+ -contents ≤ 0.5 (Stage III) the S -parameter and the positron lifetime τ_1 show a further increase. The underlying processes of these three stages will be discussed in more detail in the following. The variation of the W -parameter shows an inverse behaviour to the S -parameter, indicating that the chemical environment of the lattice defects probed by the positrons does not change.

LiCoO₂ concentration range: $1 \geq x \geq 0.6$

The evolution of the positron lifetime τ_1 with respect to the Li⁺-content of the LiCoO₂ electrode material is presented in Figure 4.36. The two complementary methods of positron lifetime (Figure 4.36) and 2d-Doppler broadening (Figure 4.35) spectroscopy show a similar trend with decreasing Li⁺-content, supporting the reliability of the measurements.

The positron lifetime τ_1 of the fully lithiated electrode of 206ps and of the powder sample of 207ps is significantly higher than the lifetimes of positrons annihilating from the free state in metal oxides (Al₂O₃: τ_{free} =140ps [145], MgO: τ_{free} =155ps [145], ZrO₂: τ_{free} =175ps [145], AlTiO₂: τ_{free} =148ps [146]). This indicates that even in the fully lithiated state saturation trapping at vacancy-type defects takes place. Since vacancy concentrations in the range of 10^{-3} are sufficient for saturation trapping, it seems reasonable that Li⁺-vacancies in this range exist even in the fully lithiated state. From Figures 4.36 and 4.35, region I, an increase of the positron lifetime τ_1 and the S-parameter can be deduced. This indicates the growth of the size of the open volumes, as a gain in the concentration beyond saturation trapping would not lead to a further rise. At Li_{0.9}CoO₂, 10% of all Li⁺-sites are unoccupied and, due to the large amount of vacancies, the formation of double vacancies is expected to occur. Further Li⁺-removal shows a plateau between $x \approx 0.8$ and $x \approx 0.7$. In fact a two-phase mixture in the composition range between Li_{0.93}CoO₂ and Li_{0.75}CoO₂ exists [14, 15, 18, 147]. In addition, a transformation from a rhombohedral insulating phase to a rhombohedral conducting phase at Li⁺-contents ≤ 0.8 is reported [39]. The insulator-metal transition and, therefore, the increased electron–positron screening in the metallic regime may reduce the positron lifetime [148, 149] and counteract any size increase of the positron traps upon further Li⁺-extraction within this Li⁺-concentration regime. Further Li⁺-removal beyond $x = 0.7$ up to $x = 0.6$ shows an increase of the positron lifetime τ_1 and the S-parameter. This reveals an increase of the open volumes sensed by the positrons due to the formation of larger open volumes. Since the lithium-ions are forming (001)-oriented layers [14, 37], Li⁺-vacancies are confined within these layers and have to form two-dimensional vacancy-cluster (Figure 4.37 (b)). The positron lifetime τ_1 of 230ps (Table 4.12) can, therefore, be attributed to double-vacancies, while the positron lifetime τ_1 of 247ps should be attributed to larger two-dimensional open volumes.

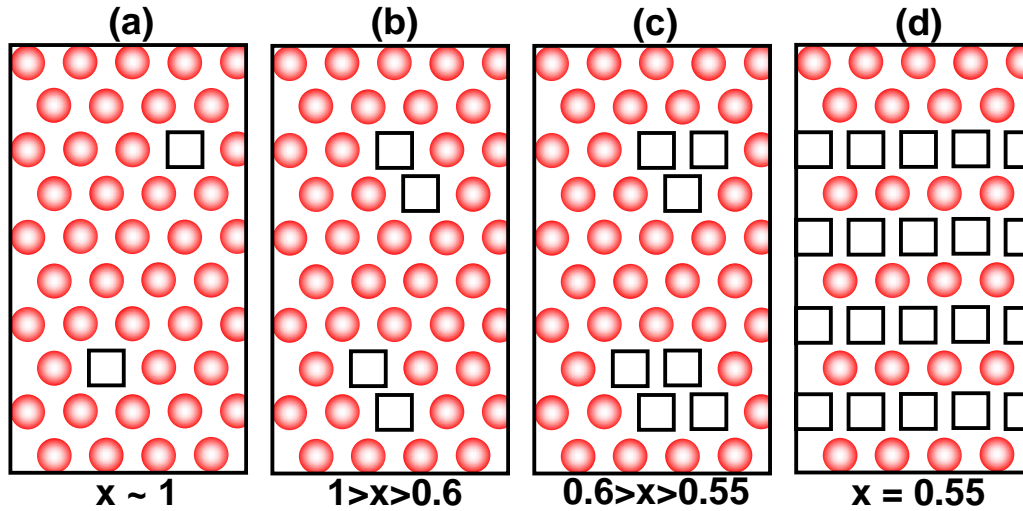


Figure 4.37: Sketches of the (001) Li^+ -layer in Li_xCoO_2 for various Li^+ -concentrations x . (a) Li^+ -layer at $x=1$. (b) At the beginning of Li^+ -removal single Li^+ -vacancies are introduced ($1 \geq x \geq 0.6$). (c) Upon further Li^+ -extraction ($0.6 \geq x \geq 0.55$) 2-dimensional vacancy cluster are formed. (d) At a Li^+ -concentration of $x \approx 0.55$ a re-ordering of the lithium-ions takes place (vacancy-cluster \rightarrow vacancy-chains [38, 150, 151]).

LiCoO_2 concentration range: $0.6 \geq x \geq 0.55$

Upon further removal of Li^+ from the electrode material a steep decrease of the S-parameter and the positron lifetime in this region (region II, Figures 4.35 and 4.36) can be observed. This is remarkable, because in this regime of saturation trapping of positrons this reduction of the positron lifetime (see Table 4.12) and the S-parameter cannot be attributed to a variation of the vacancy concentration, since upon further Li^+ -extraction the vacancy concentration increases. Therefore, the character of the open volumes in this regime has to change. A decrease of the mean size of the open volumes is indicated by the S-parameter and by the decrease of the positron lifetime τ_1 from 247ps to 228ps (region II, Figure 4.36). The mean size of the open volume becomes smaller, similar to the stage of $\text{Li}_{0.7}\text{CoO}_2$ which was attributed to double-vacancies. This indicates that a re-ordering of the Li^+ -vacancies from two-dimensional arrays to one-dimensional vacancy-chains takes place decreasing the effective size of the open volume accessible to positrons. Figure 4.37 (d) sketches this re-ordering pro-

cess. In fact a Li^+ -re-ordering process is reported in literature [14, 15, 17, 18, 37] to occur at $\text{Li}_{0.5}\text{CoO}_2$, which is well known as the reversibility limit of LiCoO_2 electrode material. This re-ordering was indirectly deduced from a monoclinic distortion of the rhombohedral lattice observed by X-ray diffraction within this Li^+ -concentration regime [14, 15, 17, 18]. The method of positron annihilation, which is sensitive to open volume, is a direct evidence for this vacancy-ordering process. Numerical simulations by Van der Ven et al. [38] showed, that Li^+ -vacancies are randomly distributed at Li^+ -concentrations larger than 0.6 whereas at Li^+ -concentrations of 0.5 one-dimensional chains of vacancies within the Li^+ -layers are found. The present study, utilising the open-volume-sensitivity of the positron annihilation techniques, indicates that Li^+ -vacancy re-ordering arises already at a Li^+ -concentration of $\text{Li}_{0.55}\text{CoO}_2$.

LiCoO₂ concentration range: $x < 0.55$

Further removal of lithium-ions from the electrode material leads to an increase in the S-parameter (region III, Figure 4.35) and the positron lifetime τ_1 up to 251ps (region III, Figure 4.36). This indicates an increase in the size of the open volumes in the electrode material. The strong increase of positron lifetime τ_1 to 250-272ps, which is in fact comparable to the positron lifetime of a metal-oxygen vacancy (Schottky pair) [11, 152] indicates the formation of CoO_2 -vacancies. At this high Li^+ -extraction stages, the lattice parameter c of the crystal structure does not increase further, but starts to decrease (see Figure 4.36) as already reported in literature [15, 18]. This decrease is accompanied by the electrochemical dissolution of Co [15], and supports the interpretation that despite the on-going formation of larger Li^+ -vacancy-cluster, CoO_2 -groups are removed as well.

Consequences on Li^+ -diffusion

The current densities in lithium-ion batteries are limited by the Li^+ -diffusion. Li^+ -diffusion in layered intercalation compounds, especially in LiCoO_2 , has been considered in first-principle calculations by Van der Ven et al. [43, 153]. Two qualitatively different Li^+ -diffusion pathways were found, as sketched in Figure 4.38. For a direct hop of a lithium-ion into a Li^+ -vacancy, the minimum energy path involves moving past a

dumbbell of oxygen-ions by the Li-ion (Figure 4.38 (a)), whereas when the Li-ion jumps into a vacancy which is part of a di-vacancy, the minimum energy path passes through a tetrahedral site, centred between the two vacancies [43, 153] (Figure 4.38 (b)).

The simulations show, that the activation barrier for the tetrahedral site hop is significantly lower than for the oxygen dumbbell hop. The authors [43, 153], therefore, propose the tetrahedral site hop as the dominating Li^+ -diffusion mechanism. Figure 4.39 shows a reproduction of the reported Li^+ -diffusion-coefficient in correlation to the Li^+ -concentration.

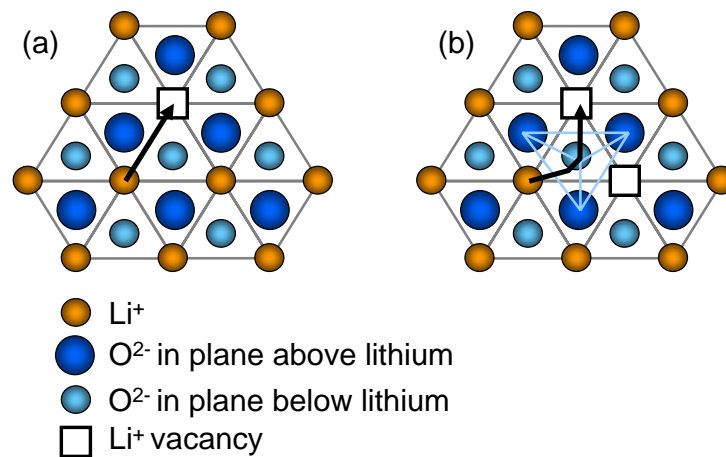


Figure 4.38: Sketch of Li^+ -diffusion pathways according to Van der Ven et al. [43, 153].

(a) Li^+ -diffusion past an oxygen dumbbell (b) Li^+ -diffusion through a tetrahedral site. Redrawn after [153].

At high Li^+ -concentrations, the calculated Li^+ -diffusion-coefficient could not be reliably calculated. With decreasing Li^+ -concentration, an increase in the diffusivity of several orders of magnitude can be observed, which is attributed to the increased concentration of divacancies and larger vacancy-cluster. A local minimum of the Li^+ -diffusion-coefficient is found at a Li^+ -concentration of $x = 0.5$, due to the re-ordering of the Li^+ -vacancies into two-dimensional vacancy chains. Further Li^+ -extraction leads to a re-increase in the diffusivity which is followed by a decrease at very low Li^+ -concentrations.

These results are very well supported by the positron-annihilation experiments. The

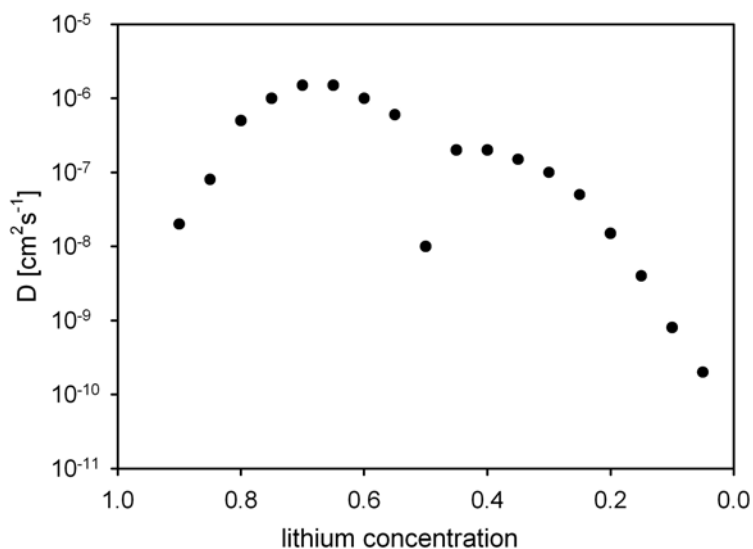


Figure 4.39: Calculated Li^+ -diffusion-coefficient in dependence of the Li^+ -concentration, redrawn after [43].

introduction of larger open volumes, such as di-vacancies and vacancy-cluster are found within a Li^+ -concentration range $1 \geq x \geq 0.6$, leading to an increase in the Li^+ -diffusion. This is followed by a decrease of the open volume around $x = 0.55$, due to the vacancy re-ordering. This is attributed to reduce the Li^+ -diffusion coefficient. Also in accordance is the further vacancy-clustering observed for $x = 0.55$ with the re-increase of the Li^+ -diffusivity. At very low Li^+ -concentrations ($x \leq 0.3$), the introduction of additional metal-oxygen vacancies obscures any decrease of the open volumes due to the decrease of the lattice constant c . This decrease of the lattice parameter is assumed to lead to a decrease of the Li^+ -diffusion coefficient [43, 153].

4.2.3 LiMn₂O₄

LiMn₂O₄ is a spinel type Li⁺-intercalation electrode material and is written as Li[Mn₂]O₄ in typical spinel notation. The main benefits of this material, compared to the previous presented LiCoO₂ are a) the complete removability of Li⁺ without any structural change of the host material [154] and the usability of the cheap (price Mn about 1% of price Co) and less harmful manganese instead of the much more expensive and environmental harmful cobalt. A major drawback of this material is the lower energy density, making it less attractive for volume sensitive applications. The spinel structure is a cubic closed-packed oxygen lattice, where manganese occupies $\frac{1}{2}$ of the octahedral sites while the Li⁺ occupies $\frac{1}{4}$ of the tetrahedral sites (see Figure 4.40). The mean oxidation state of the manganese atoms in the fully lithiated electrode is +3,5. In the spinel host structure [Mn₂]O₄ a three-dimensional network of face-shared tetrahedra and octahedra (8a-16c-8a-16c-etc.) allows unrestricted diffusion of lithium-ions. This is a major difference to the two-dimensional Li⁺-diffusion in the layered LiCoO₂ structure (see Figure 4.40). In literature [79], three reasons for capacity fading in LiMn₂O₄ are supposed:

- (1) Dissolution of the spinel framework at the end of discharge (Li⁺-introduction).
- (2) A phase transition from cubic to tetragonal symmetry at the end of discharge (Li⁺-introduction), due to the onset of the Jahn-Teller distortion.
- (3) An instability of the highly delithiated spinel particles in the organic electrolyte at the end of charge (Li⁺-extraction).

Results

The electrode preparation of LiMn₂O₄ was similar to the preparation of the LiCoO₂-electrodes (see section 4.2.1 and Table 4.10). Therefore, and due to a thickness of the electrode of about 170 μm the measurement setup D (see section 3, page 26) was chosen. The electrochemical Li⁺-extraction was performed as described in section 3.2.2.

A two-term lifetime analysis of the fully lithiated electrode material reveals a dominant lifetime of 195ps with an intensity of 95.3% and a second lifetime of 628 ps with a

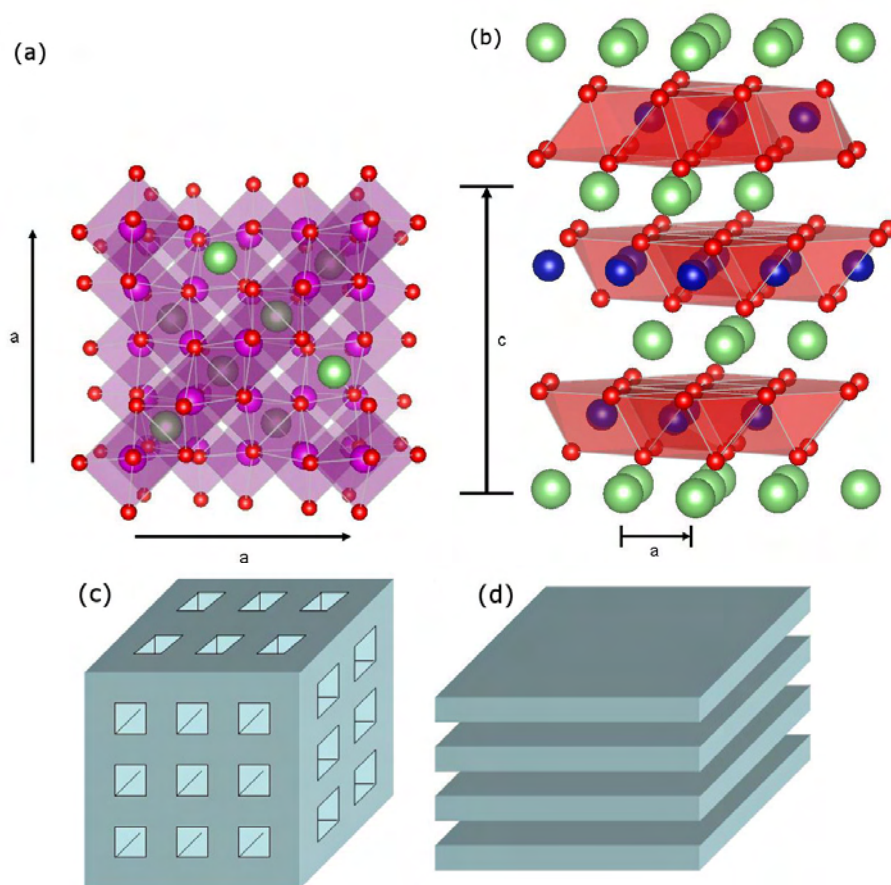


Figure 4.40: Comparison of the structures of (a) LiMn_2O_4 and (b) LiCoO_2 . The (a) LiMn_2O_4 spinel host structure offers (c) 3-dimensional Li^+ -diffusion pathways, while in (b) LiCoO_2 Li^+ -diffusion is restricted to (d) 2-dimensional layers. Structures drawn with VESTA [158], red: oxygen, green: lithium, blue: cobalt, magenta: manganese

Table 4.13: Comparison of positron lifetimes and relative intensities of a LiMn_2O_4 -powder sample and the LiMn_2O_4 -electrode.

sample	τ_1 [ps]	τ_2 [ps]	I_1	I_2
LiMn_2O_4 -electrode	195 (± 3)	628 (± 6)	95.3	4.7
LiMn_2O_4 -powder	189 (± 3)	440 (± 6)	94.3	5.7

relative intensity of 4.7%. The longer second lifetime can be attributed to annihilations on LiMn_2O_4 particle surfaces and to annihilations within the polymer binder between

the particles. This longer second lifetime from annihilation on particle surfaces is a typical feature found in compressed powder samples [144]. The dominant lifetime component τ_1 is attributed to positron annihilation within the LiMn_2O_4 particles. This interpretation is supported by the dominant positron lifetime τ_1 of 189 ps, measured on a compressed pure powder sample (see Table 4.15). The slightly increased positron lifetime τ_1 of the electrode sample compared to the pure powder sample may be caused by additional annihilation within the added carbon particles.

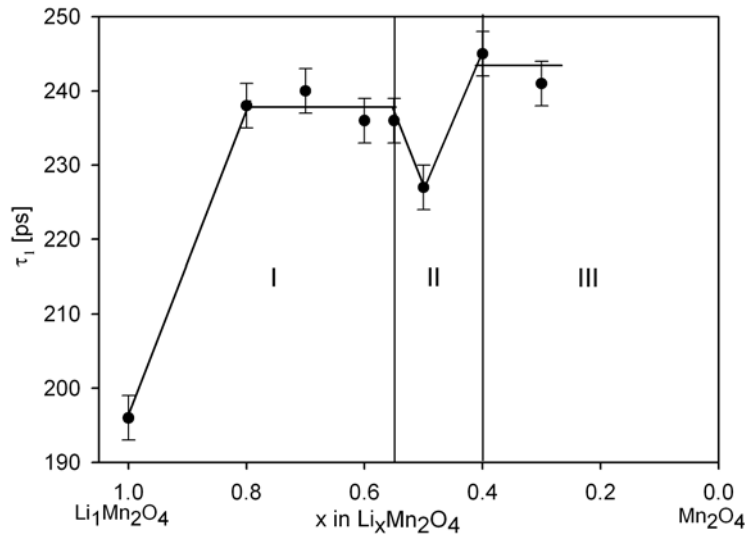


Figure 4.41: Evolution of the positron lifetime τ_1 as function of Li^+ -content.

Table 4.14: Positron lifetimes τ_1 ($\pm 3\text{ps}$) of $\text{Li}_x\text{Mn}_2\text{O}_4$ -electrodes in dependence of Li^+ -content x .

Li^+ -concentration x	1	0.8	0.7	0.6	0.55	0.5	0.4	0.3
τ_1 [ps]	196	238	240	236	236	227	245	241

Figure 4.41 and Table 4.14 show the positron lifetime τ_1 of the LiMn_2O_4 electrode with decreasing Li^+ -content. From Figures 4.41 and 4.42 three distinct stages can be found upon lithium-ion extraction. First, an increase of the positron lifetime and S-parameter with decreasing lithium content and the formation of a plateau, down to $x = 0.55$ (stage I), is observed. Second, a decrease of the positron lifetime and the S-parameter at an intermediate Li^+ -concentration of about 0.5 (stage II), followed by a re-increase of the

S-parameter and the positron lifetime at $x < 0.5$ is found (stage III).

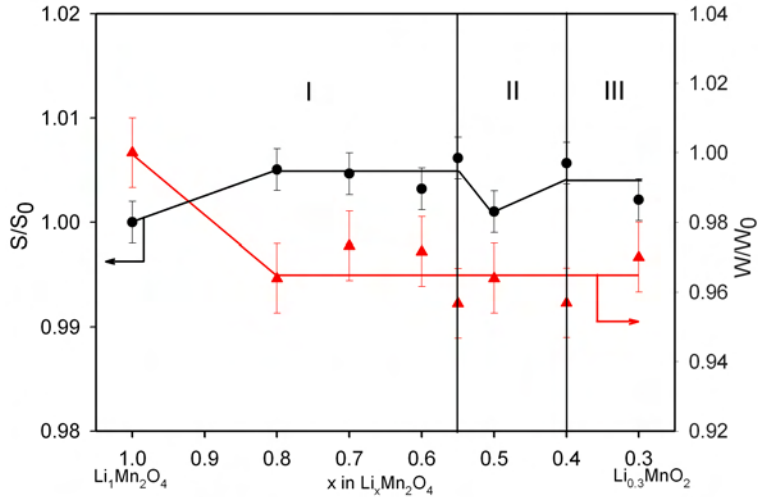


Figure 4.42: Normalized S&W parameter plots of Doppler broadening in dependence of Li^+ -extraction, with respect to S_0 and W_0 of fully lithiated LiMn_2O_4 .

$\text{Li}_x\text{Mn}_2\text{O}_4$ concentration range $1 \geq x \geq 0.55$:

The positron lifetime of $\text{Li}_x\text{Mn}_2\text{O}_4$ shows a substantial increase from $\tau_1 = 195\text{ps}$ to $\tau_1 = 238\text{ps}$ upon starting Li^+ -extraction. This increase of the positron lifetime is attributed to the charging induced formation of vacancies within the LiMn_2O_4 . The large amount of open volumes at these stage of Li^+ -extraction (at $\text{Li}_{0.8}\text{Mn}_2\text{O}_4$, 20% of all Li^+ -sites are unoccupied) is sufficient to provide saturation trapping at open volume defects, which means that all positrons are trapped at these defects. Further Li^+ -removal does not significantly change the positron lifetime down to an electrode composition of $\text{Li}_{0.55}\text{Mn}_2\text{O}_4$. A similar trend upon Li^+ -removal, as observed by the positron lifetime, can be deduced from the S-parameter (Figure 4.42). At first, a significant increase of the S-parameter indicates the formation of additional open volumes. Further Li^+ -removal down to $\text{Li}_{0.55}\text{Mn}_2\text{O}_4$ does not lead to any significant change of the S-parameter, indicating saturation trapping at open volumes.

$\text{Li}_x\text{Mn}_2\text{O}_4$ concentration range $0.55 \geq x > 0.4$:

At a composition of $\text{Li}_{0.5}\text{Mn}_2\text{O}_4$ a decrease of the positron lifetime τ_1 , emerges. This

decrease of the positron lifetime indicates a decrease of the free volume size of the positron trap, as upon further Li^+ -extraction the concentration of open volumes increases further. In addition a decrease of the S-parameter at $\text{Li}_{0.5}\text{Mn}_2\text{O}_4$ is observed and indicates a decrease in the open volume accessible for the positron. Due to the fact, that no structural changes of the Mn_2O_4 host material are monitored [156, 157], a subtle change, similar to the Li^+ -vacancy ordering process discussed in section 4.2.2 is supposed. Both, τ_1 and S-parameter indicate, that a Li^+ -vacancy ordering process occurs. In fact, an ordering of the remaining lithium-ions on one half of the 8a tetrahedral sites is reported in literature for a Li^+ -concentration of 0.5 [78, 79, 155, 157]. According to calculations of Van der Ven et al. [155], the Li^+ segregate to the 8a tetrahedral sites, as they exhibit a lower energy state. An ordering of lithium-ions and vacancies on the tetrahedral sites is reported to be similar to that of Zn in zinc blende (ZnS) [155]. This ordering process does not damage the structural integrity of the Mn_2O_4 host material, proven by the good stability of this material for repeated intercalation and deintercalation of Li^+ [156, 157].

$\text{Li}_x\text{Mn}_2\text{O}_4$ concentration range $x < 0.5$:

Continued removal of the lithium-ions from the Mn_2O_4 framework leads to a re-increase of the positron lifetime to $\tau_1 = 245\text{ps}$ and to a re-increase of the S-parameter. The constancy of this positron lifetime clearly shows, that no dissolution of the host structure occurs. The stability of the host structure of $\text{Li}_x\text{Mn}_2\text{O}_4$ up to Li^+ -extraction as high as 70% has repeatedly been reported in literature [16, 78, 154] and is one of the reasons, despite the abundance of manganese and its low price, that LiMn_2O_4 is considered to be used in lithium-ion batteries as cathode material.

The presented results indicate that at least down to a composition of $\text{Li}_{0.3}\text{Mn}_2\text{O}_4$ the spinel particles are stable in the organic electrolyte. Therefore, an instability of the highly delithiated spinel particles in the organic electrolyte at the end of charge (Li^+ -extraction) can be ruled out as degradation mechanism when cycling the $\text{Li}_x\text{Mn}_2\text{O}_4$ down to a Li^+ -content of 0.3.

4.2.4 $\text{Li}(\text{Co}_{1/3}\text{Mn}_{1/3}\text{Ni}_{1/3})\text{O}_2$

$\text{Li}(\text{Co}_{1/3}\text{Mn}_{1/3}\text{Ni}_{1/3})\text{O}_2$ is a solid solution of Ni^{2+} , Mn^{4+} and Co^{3+} , which is isostructural to LiCoO_2 . This material exhibits an increased structural [159, 160] and thermal stability compared to LiCoO_2 [161] and contains less of the expensive and toxic cobalt. Due to a similar size of Li^+ and Ni^{2+} , some of the lithium-ions within the Li^+ -layers are substituted by nickel ions and vice versa. These nickel ions on the Li^+ -sublayer lead to an increased structural stability at the expense of charge capacity, as Li^+ located at the nickel layers can not be extracted.

Results

The measurement setup for the $\text{Li}(\text{Co}_{1/3}\text{Mn}_{1/3}\text{Ni}_{1/3})\text{O}_2$ -electrode material was chosen similar to the measurement setup reported for the LiCoO_2 -electrodes (setup D, see section 3, page 26). The electrochemical Li^+ -extraction was performed as described in section 3.2.2.

In Table 4.15, a comparison of the positron lifetimes obtained for measurements on a fully lithiated $\text{Li}(\text{Co}_{1/3}\text{Mn}_{1/3}\text{Ni}_{1/3})\text{O}_2$ -electrode and a fully lithiated $\text{Li}(\text{Co}_{1/3}\text{Mn}_{1/3}\text{Ni}_{1/3})\text{O}_2$ -powder sample is presented. A two-term lifetime analysis of the fully lithiated electrode material reveals a dominant lifetime of 223ps with an intensity of 94.3% and a second lifetime of 702ps with a relative intensity of 5.7%. The longer second lifetime can be attributed to annihilations on $\text{Li}(\text{Co}_{1/3}\text{Mn}_{1/3}\text{Ni}_{1/3})\text{O}_2$ particle surfaces and to annihilations within the polymer binder between the particles. This longer second lifetime from annihilation on particle surfaces is a typical feature

Table 4.15: Comparison of positron lifetimes and relative intensities of a $\text{Li}(\text{Co}_{1/3}\text{Mn}_{1/3}\text{Ni}_{1/3})\text{O}_2$ -powder sample and the $\text{Li}(\text{Co}_{1/3}\text{Mn}_{1/3}\text{Ni}_{1/3})\text{O}_2$ -electrode.

sample	τ_1 [ps]	τ_2 [ps]	I_1	I_2
$\text{Li}(\text{Co}_{1/3}\text{Mn}_{1/3}\text{Ni}_{1/3})\text{O}_2$ -electrode	223 (± 2)	702 (± 6)	94.3	5.7
$\text{Li}(\text{Co}_{1/3}\text{Mn}_{1/3}\text{Ni}_{1/3})\text{O}_2$ -powder	207 (± 2)	562 (± 6)	96.7	3.3

Table 4.16: Positron lifetimes τ_1 (± 2 ps) of $\text{Li}(\text{Co}_{1/3}\text{Mn}_{1/3}\text{Ni}_{1/3})\text{O}_2$ -electrodes in dependence of Li^+ -content x .

Li^+ -concentration x	1	0.8	0.7	0.6	0.55	0.5	0.4
τ_1 [ps]	223	232	237	250	246	242	248

found in compressed powder samples [144]. The dominant lifetime component τ_1 is attributed to positron annihilation within the $\text{Li}(\text{Co}_{1/3}\text{Mn}_{1/3}\text{Ni}_{1/3})\text{O}_2$ particles. This interpretation is supported by the dominant positron lifetime τ_1 of 207ps, measured on a compressed pure powder sample (see Table 4.15). The increased positron lifetime τ_1 of the electrode sample may be caused by an additional, unresolved positron lifetime from the added carbon particles.

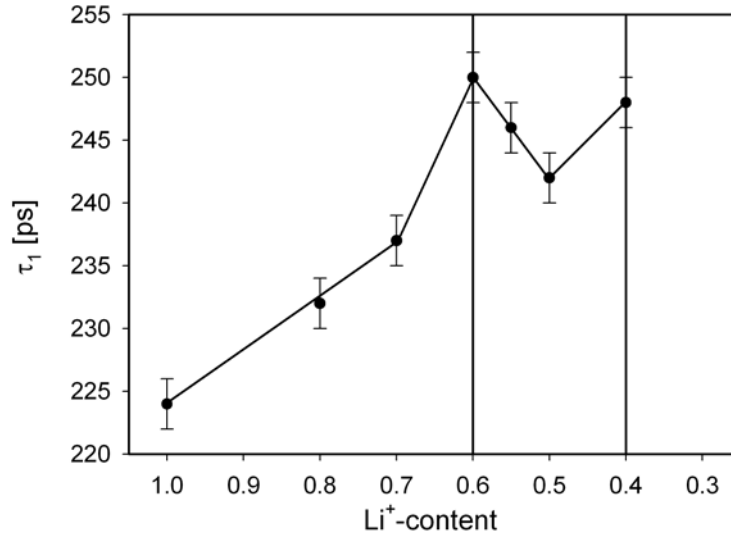


Figure 4.43: Evolution of positron lifetime τ_1 as function of Li^+ -content.

Figure 4.43 and Table 4.16 show the evolution of the positron lifetime τ_1 in dependence of the Li^+ -content. Upon Li^+ -extraction, three distinct features can be observed. At first, a clear increase of the positron lifetime, due to the introduction of Li^+ -vacancies takes place within a Li^+ -concentration range of $1 \geq x \geq 0.6$. Between a Li^+ -concentration of $0.6 \geq x \geq 0.5$ a decrease of the positron lifetime appears. At a lower Li^+ -content of $x < 0.5$ a re-increase of the positron lifetime is visible.

Li_x(Co_{1/3}Mn_{1/3}Ni_{1/3})O₂ concentration range $1 \geq x \geq 0.6$:

Upon Li⁺-extraction, an increase of the positron lifetime τ_1 from 223ps to 232ps at a Li⁺-content of $x = 0.8$ can be observed. This may be attributed to the introduction of Li⁺-vacancies upon battery charging. Upon continued Li⁺-extraction, a positron lifetime value of 250ps is reached at a composition of Li_{0.6}(Co_{1/3}Mn_{1/3}Ni_{1/3})O₂. Due to the occurrence of saturation trapping, this increase is attributed to an increase in the size of the open volumes and, therefore, to vacancy-clustering. As Li(Co_{1/3}Mn_{1/3}Ni_{1/3})O₂ crystallises in a to LiCoO₂ isostructural layered structure (Figure 4.40), the positron lifetimes of Li(Co_{1/3}Mn_{1/3}Ni_{1/3})O₂ and LiCoO₂ should be comparable. At a low Li⁺-extraction stage, a positron lifetime of 232ps, which is similar to the positron lifetime of LiCoO₂ (231ps) at the same Li⁺-extraction stage, is found. The increase of the positron lifetime to 250ps upon further Li⁺-extraction up to a composition of Li_{0.6}(Co_{1/3}Mn_{1/3}Ni_{1/3})O₂ is similar to the behaviour of Li_{0.6}CoO₂ (247ps). As Li(Co_{1/3}Mn_{1/3}Ni_{1/3})O₂ does not show an insulator-metallic conductor transition upon Li⁺-extraction, no formation of a positron lifetime plateau is observed in contrast to LiCoO₂.

Li_x(Co_{1/3}Mn_{1/3}Ni_{1/3})O₂ concentration range $0.6 \geq x \geq 0.5$:

Further Li⁺-extraction reveals a decrease of the positron lifetime down to 242ps after extracting half of the Li⁺. The decrease of the positron lifetime of about 8ps is smaller than the lifetime decrease observed in LiCoO₂ (about 20ps). As upon Li⁺-extraction the vacancy concentration increases, the character of the open volumes in this regime changes. A decrease of the mean size of the open volumes is indicated by the decrease of the positron lifetime τ_1 from 250 ps to 242ps (Figure 4.43). The decrease of the positron lifetime may, therefore, be ascribed to a Li⁺-vacancy ordering processes, similar to the vacancy-ordering processes observed in LiCoO₂.

Obviously, a Li⁺-vacancy reordering is taking place in the composite material as well, but not as pronounced as in the single component electrode material and over a wider range of Li⁺-concentration. This extended re-ordering, compared to LiCoO₂, may be caused by the addition of nickel to this system. In fact, in LiNiO₂ a different vacancy-ordering is proposed from first principle calculations [162], compared to the vacancy-chain formation in LiCoO₂. It was found that in LiNiO₂ the lithium-ions may

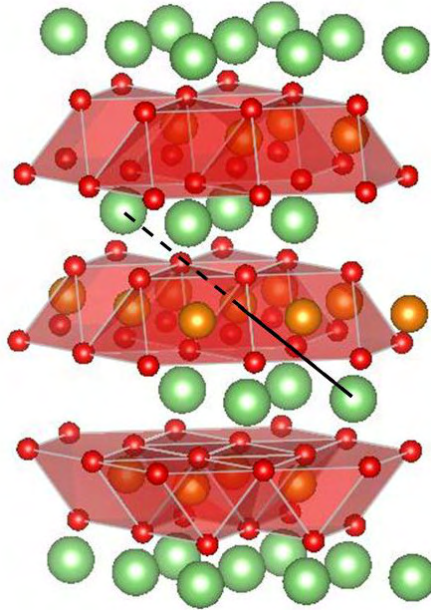


Figure 4.44: Interplane correlation of Li^+ O-Ni-O Li^+ according to M. E. Arroyo y de Dompablo et al. [162]. Structures drawn with VESTA [158], red: oxygen, green: lithium, orange: nickel

experience interplane interaction [162] (see Figure 4.44), which has an effect on the vacancy-ordering. In addition, vacancy-ordering in LiNiO_2 is proposed to occur at Li^+ -concentrations of $x = \frac{5}{6}, \frac{3}{4}, \frac{3}{5}, \frac{1}{2}, \frac{2}{5}, \frac{1}{3}$ and $\frac{1}{4}$ [162]. In addition it is known from literature [162, 163], that a minor fraction of nickel-ions tends to move into the Li^+ -layers and may alter the re-ordering of the Li^+ -vacancies. In fact, the existence of Ni-ions in the Li^+ -layers of $\text{Li}_x(\text{Co}_{1/3}\text{Mn}_{1/3}\text{Ni}_{1/3})\text{O}_2$ is reported [160]. Rosciano et al. [160] found, that the Ni-ions within the Li^+ -layers are not mobile and act as pillars, increasing the structural stability in the deintercalated state. In Figure 4.45 a sketch of the by Delmas et al. [164] reported effects of Ni-ions within the Li^+ -layers on Li^+ -re-intercalation and vacancy-ordering is shown. The Ni-ions decrease locally the inter-plane distance between NiO_2 -layers, which hampers Li^+ -ordering and re-introduction. The Li^+ interplane interaction [162] and the effects of Ni-ions within the Li^+ -layers [160, 164] reduce the vacancy-ordering. The less pronounced decrease of the positron lifetime τ_1 indicates this reduced vacancy ordering.

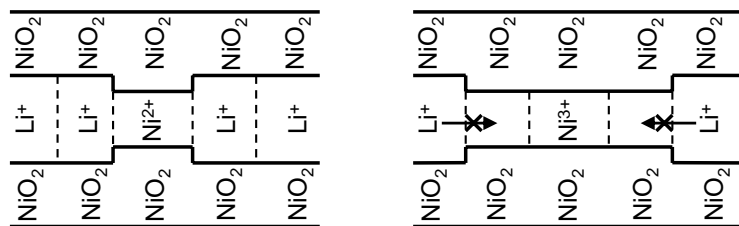


Figure 4.45: Sketch of the effects of Ni^{3+} within the Li^+ -layer on the vacancy-ordering, redrawn after C. Delmas et al. [164].

$\text{Li}_x(\text{Co}_{1/3}\text{Mn}_{1/3}\text{Ni}_{1/3})\text{O}_2$ concentration range $x < 0.5$

Following the positron lifetime decrease around a Li^+ -concentration of 0.5, is a re-increase of τ_1 to 248ps. This increase may be attributed to the formation of larger open volumes, due to the continued formation of additional Li^+ -vacancies.

4.2.5 Comparison and Summary

For the first time, positron annihilation techniques have been utilised to investigate the atomistic processes of Li^+ -extraction from commercially established lithium-ion cathode materials. It was shown, that positron annihilation spectroscopy is a valuable tool to investigate charging induced atomic processes in electrode materials of lithium-ion rechargeable batteries.

Remarkably, all of the investigated Li-ion cathode materials show similar trends upon Li^+ -extraction. Starting Li^+ -extraction from the host materials leads to an increase of the positron lifetime and the S-parameter. This increase can be attributed to the introduction of Li^+ -vacancies and the formation of double vacancies and larger vacancy-cluster. Further Li^+ -extraction leads to a decrease of the positron annihilation parameter (τ_1 and S-parameter) at a Li^+ -concentration around 0.55 to 0.5. This decrease, which emerges in all three investigated materials, is attributed to a Li^+ -vacancy ordering process, due to Li^+ - Li^+ interaction. Li^+ -extraction beyond this level, leads to a re-increase of the positron lifetime and the S-parameter due to the introduction of additional open volumes and a perturbation of the ordered regime.

- In Li_xCoO_2 an increase of the positron lifetime and Doppler broadening S-parameter with increasing Li^+ -extraction can be observed. As a consequence of the high vacancy concentrations this increase originates from the formation of larger open volumes, rather than from an increase in the concentration. Upon further Li^+ -removal, an expected increase of the positron lifetime due to the increasing size of open volumes, is counteracted by an electronic transition from insulating to conducting. In the metallic state, an increased electron-positron screening counteracts any increase in the open volume. After passing this transition regime between Li^+ -contents of 90% to 70% an increase of the positron lifetime due to the increasing size of the vacancy-cluster is observed. A decrease of τ_1 and the S-parameter at an intermediate Li^+ -concentration of $x = 0.55$ indicates a transformation from two-dimensional vacancy-arrays to one-dimensional vacancy-chains, which occurs in the course of Li^+ -re-ordering. At higher degrees of Li^+ -extraction the dissolution of Co could be monitored by a steep increase in the positron lifetime τ_1 and the S-parameter causing severe degradation of the electrode

material. The results at high and intermediate lithium-ion concentrations support the simulation results of Van der Ven et al. [43, 153], that Li^+ -diffusion is mediated by a divacancy-mechanism.

- $\text{Li}_x\text{Mn}_2\text{O}_4$ crystallises in a spinel structure and does in contrast to Li_xCoO_2 not exhibit a layered structure. At first, a strong increase of the positron lifetime upon Li^+ -extraction from $\text{Li}_x\text{Mn}_2\text{O}_4$ can be observed, similar to Li_xCoO_2 , which indicates the introduction of Li^+ -vacancies and the formation of larger vacancy-cluster. After this first increase, the positron lifetime and S-parameter stay constant upon further lithium extraction, down to a Li-ion content of 0.55. This is different, than the behaviour of Li_xCoO_2 in this concentration regime and can be attribute to structural and electronical differences of the two materials. First, $\text{Li}_x\text{Mn}_2\text{O}_4$ does not exhibit a layered structure, such as Li_xCoO_2 , but has a spinel structure with three dimensional pathways for Li^+ -diffusion (see Figure 4.40). Second, in $\text{Li}_x\text{Mn}_2\text{O}_4$ no insulator–metallic conductor phase transition takes place. Due to the increased Li^+ -diffusion, the absent insulator–conductor transition and the structural difference, $\text{Li}_x\text{Mn}_2\text{O}_4$ shows a positron lifetime plateau upon Li^+ -extraction. At a composition of $\text{Li}_{0.5}\text{Mn}_2\text{O}_4$ the decrease of the positron lifetime indicates a Li^+ -vacancy ordering onto the 8a tetrahedral sites. This Li^+ -vacancy ordering leads to a reduction of the open volumes within the $\text{Li}_x\text{Mn}_2\text{O}_4$ -particles.

Upon further Li^+ -extraction a re-increase of both, the positron lifetime and the S-parameter is observed, which leads to a second plateau. In contrast to the previously presented studies of Li_xCoO_2 , the host structure of $\text{Li}_x\text{Mn}_2\text{O}_4$ is stable to Li^+ -extraction and no dissolution of Mn_2O_4 takes place. Tube like vacancy chains are supposed to be formed upon Li^+ -extraction and, therefore, the obtained positron lifetime τ_1 of about 243 ps seems to be the limiting positron lifetime in $\text{Li}_x\text{Mn}_2\text{O}_4$.

- The third electrode material is $\text{Li}(\text{Co}_{1/3}\text{Mn}_{1/3}\text{Ni}_{1/3})\text{O}_2$, which is isostructural to Li_xCoO_2 . Upon Li^+ -extraction a linear increase of the positron lifetime, due to the continuous introduction of vacancies is observed. No indication for the formation of a plateau is found in contrast to Li_xCoO_2 and $\text{Li}_x\text{Mn}_2\text{O}_4$. This different behaviour may be attributed to the structural and electronical differences of the materials. First, $\text{Li}(\text{Co}_{1/3}\text{Mn}_{1/3}\text{Ni}_{1/3})\text{O}_2$ does exhibit a layered structure (see Figure 4.40) and not a

spinel structure as LiMn_2O_4 , therefore larger vacancy-arrays may form.

Second, $\text{Li}(\text{Co}_{1/3}\text{Mn}_{1/3}\text{Ni}_{1/3})\text{O}_2$ does not show an insulator–metallic conductor phase-transition as LiCoO_2 , which counteracts an increasing positron lifetime of larger vacancy-cluster due to increased electron-positron screening, as observed in LiCoO_2 . Therefore, a continuous increase of τ_1 with decreasing Li^+ -concentration is observed.

A positron lifetime decrease, at a Li^+ -concentration around $x = 0.55$ to $x = 0.5$ is observed in this material as well. This decrease is attributed to a vacancy-ordering phenomenon, similar to the vacancy ordering in LiCoO_2 . This ordering takes place over a wider range of Li^+ -concentration compared to the vacancy-ordering observed in LiCoO_2 and LiMn_2O_4 and may be attributed to the addition of nickel to the system. Nickel-ions are known to be of similar size as lithium-ions and may, therefore, move into the Li^+ -layers and may disturb the vacancy-ordering. In addition, in LiNiO_2 a significant different Li^+ -vacancy-ordering behaviour is reported in literature [162, 163]. Lithium-ions may interact between different lithium layers in LiNiO_2 via the nickel-ions and this interaction seems to alter the vacancy ordering. The decrease of positron lifetime due to the vacancy-ordering is followed by a re-increase of the positron lifetime. Further Li^+ -extraction, therefore, leads to re-increasing vacancy-cluster.

The presented results encourage future investigations of Lithium-ion battery systems with methods of positron annihilation spectroscopy. The utilisation of positron beams with variable positron energy could be used for depth-profiling of discharged electrodes to identify anisotropies within the electrodes upon battery charging and discharging. Another promising concept for further investigations would be in-situ investigations of batteries upon lithium-ion extraction as well as ex-situ investigations after multiple charge/discharge cycles.

CHAPTER 5

Summary and Conclusion

In this work vacancy-type and interface related defects in alloys and oxides were investigated. These defects may significantly alter materials properties and influence the structural stability. Various new and unique insights into vacancy and interface correlated phenomena could be revealed, due to the sensitive and defect specific methods of the positron annihilation, which cannot be matched by other methods. On the one hand, the size of vacancy-cluster can be identified by the positron lifetime, while by the Doppler broadening of the annihilation radiation the chemical environment of the open volume defects may be identified. In addition absolute vacancy concentrations between 10^{-7} to 10^{-3} can be resolved. A fundamental and comprehensive analysis of the defect characteristics and defect processes were obtained, as summarised in the following:

For the defect formation upon HPT-deformation and the stability upon annealing of metal and alloy samples a strong correlation to the sample purity could be determined.

- The defect formation due to high pressure torsion in metals is significantly affected by the concentration of impurities (see section 4.1.1). A finer grain structure (150nm) is stabilised by impurity atoms in contrast to the pure sample

(340nm), while the defect annealing and recrystallisation is shifted to higher temperatures by about 100°C. Further, in pure iron larger vacancy-cluster, consisting of 6 vacancies, are formed, while impurities lead to smaller vacancy-impurity complexes in ARMCO-iron.

- After HPT-deformation of a solution treated and quenched Al-Cu alloy (see section 4.1.2), the formation of small grains with a size of about 100nm is observed, which are stabilised by the equilibrium Θ -precipitates, which are dynamically formed upon deformation. Further, a copper stabilised vacancy-concentration in the range of 10^{-4} is found, which is in the order of vacancy-concentrations introduced by HPT reported in literature [4, 129, 130]. Upon annealing, the typical formation of semi-coherent Θ' -precipitates upon low temperature treatment is skipped, while the Θ -precipitates and aluminium grains are subject to further growth. At temperatures of about 400°C dissolution of the Θ -precipitates begins and leads to the formation of Guinier-Preston zones. Within a temperature range of 400°C to 550°C, no significant differences in the open volume defects between the HPT-deformed and an undeformed reference sample can be observed. From the undeformed reference sample, an increased trapping at copper-decorated misfit-dislocations could be observed and a positron lifetime of 177ps could be attributed to this type of defect, while it was found, that the incoherent Θ -precipitates do not act as positron traps.
- It was found that, within metals even minor impurities significantly affect the formation and stabilisation of vacancy-type and interface related open volume defects.

Even materials in perfect thermal equilibrium, such as a very slow cooled meteorite sample, were found to exhibit a complex composition of defects.

- An iron-nickel meteorite revealed (see section 4.1.3), that, even though in perfect thermal equilibrium after a cooling rate of $35 \times 10^{-6} \text{Ka}^{-1}$, two types of defects are present. First, upon those low cooling rates, carbon precipitates are formed within the meteorite sample. These precipitates were found to dissolve at about 660°C. Second, nickel rich precipitates with a mean size of about 200nm were found within the nickel poor Kamacite regions. These precipitates were found

to dissolve at temperatures higher than 450°C, as the solubility of nickel within iron shows a strong increase and diffusivity is sufficiently high.

In the investigated oxide materials, which are used as cathode materials in lithium-ion batteries (see section 4.2), three significant characteristic processes could be identified for all three investigated materials:

- Upon Li⁺-extraction the formation of vacancy-cluster is observed. In the materials with a layered structure (LiCoO₂ and LiNi_{1/3}Mn_{1/3}Co_{1/3}O₂), the formation of two-dimensional vacancy-agglomerates is found, while in LiMn₂O₄ which crystallises in the spinel structure tube like vacancy-cluster are formed.
- After removal of about 50% of the Li⁺ from the cathode materials (Li₁CoO₂ → Li_{0.55}CoO₂, Li₁Mn₂O₄ → Li_{0.5}Mn₂O₄ and Li₁Ni_{1/3}Mn_{1/3}Co_{1/3}O₂ → Li_{0.55}Ni_{1/3}Mn_{1/3}Co_{1/3}O₂ or Li_{0.5}Ni_{1/3}Mn_{1/3}Co_{1/3}O₂) a vacancy ordering phenomenon is clearly identified by a strong decrease of the positron lifetimes in all three materials.
- Further extraction of Li⁺ leads to the formation of larger Li⁺-vacancy-cluster in LiMn₂O₄ and LiNi_{1/3}Mn_{1/3}Co_{1/3}O₂, whereas in LiCoO₂ the dissolution of CoO₂ can be monitored. This shows clearly, that the host structure of LiCoO₂ is subject to severe degradation upon Li⁺-extraction beyond 50%, whereas the host structures of LiMn₂O₄ and LiNi_{1/3}Mn_{1/3}Co_{1/3}O₂ are stable within the investigated Li⁺-extraction ranges.

Overall it could be demonstrated for the first time, that positron annihilation techniques are capable to give new and unique insights into the processes of lithium extraction in lithium-ion cathode materials. Positron lifetime and Doppler broadening experiments could extend the understanding of fundamental processes within this aspiring field in materials physics.

Bibliography

- [1] M. Krystian, D. Setman, B. Mingler, G. Krexner, and M.J. Zehetbauer, *Scripta Mater.* **62**, 49, (2010)
- [2] D. Setman, E. Schafner, E. Korznikova, and M.J. Zehetbauer, *Mat. Sci. Eng. A* **493**, 116, (2008)
- [3] C. Mangler, C. Gammer, H.P. Karthaler, and C. Rentenberger, *Acta Mater.* **58**, 5631, (2010)
- [4] B. Oberdorfer, B. Lorenzoni, K. Unger, W. Sprengel, M.J. Zehetbauer, R. Pippan, and R. Würschum, *Scripta Mater.* **63**, 452, (2010)
- [5] B. Oberdorfer, E.-M. Steyskal, W. Sprengel, R. Pippan, M.J. Zehetbauer, W. Puff, and R. Würschum, *J. Alloys Comp.* **509S**, 309, (2011)
- [6] C. Gammer, C. Mangler, H.P. Karthaler, and C. Rentenberger, *Scripta Mater.* **65**, 57, (2011)
- [7] M. Lewandowska and K. J. Kurzydowski, *Materials Characterization* **55**, 395, (2005)
- [8] M. Lewandowska, *J. of Microscopy* **224**, 34, (2006)
- [9] W. Lechner, W. Puff, B. Mingler, M.J. Zehetbauer, and R. Würschum, *Scr. Mater.* **61**, 383, (2009)
- [10] R. Würschum, B. Oberdorfer, E.-M. Steyskal, W. Sprengel, W. Puff, P. Pikart, C. Hugenschmidt, and R. Pippan, *Physica B* **407**, 2670, (2012)

- [11] G. Brauer, J. Kuriplach, J. Cizek, W. Anwand, O. Melikohva, I. Prochazka, and W. Skorupa, *Vacuum* **81**, 1314, (2007)
- [12] A. Somoza, M.P. Petkov, K. G. Lynn, and A. Dupasquier, *Phys. Rev. B* **65**, 094107, (2002)
- [13] P. Asoka-Kumar, M. Alatalo, V.J. Ghosh, A.C. Kruseman, B. Nielsen, and K.G. Lynn, *Phys. Rev. Lett.* **77**, 2097, (1996)
- [14] J.N. Reimers and J.R. Dahn, *J. Electrochem. Soc.* **139**, 2091, (1992)
- [15] G.G. Amatucci, J.M. Tarascon, and L.C. Klein, *J. Electrochem. Soc.* **143**, 1114, (1996)
- [16] M.M. Thackeray, *Prog. Solid St. Chem.* **25**, 1, (1997)
- [17] Y. Shao-Horn, L. Croguennec, C. Delmas, E.C. Nelson, and M.A. O'Keefe, *Nature Materials* **2**, 464, (2003)
- [18] N. Sharma, V.K. Peterson, M.M. Elcombe, M. Adeev, A.J. Studer, N. Blagojevic, R. Yussoff, and N. Kamaruzlaman, *J. Power Sources* **195**, 8258, (2010)
- [19] R.O. Simmons and R.W. Baluffi, *Phys. Rev.* **117**, 52, (1960)
- [20] A. Dubravina, M.J. Zehetbauer, E. Schafner, and I.V. Alexandrov, *Mat. Sci. Eng. A* **387-389**, 817, (2004)
- [21] E. Schafner and M. Zehetbauer, *Rev. Adv. Mater. Sci.* **10**, 28, (2005)
- [22] H.-E. Schaefer and R. Würschum, *Phys. Lett. A* **119**, 370, 1987
- [23] U. Brossmann, W. Puff, and R. Würschum, in: E. Kaufmann (Ed.), *Characterization of Materials*, John Wiley, NJ, USA, on-line publication. Available from: <http://onlinelibrary.wiley.com/doi/10.1002/0471266965.com110/abstract>
- [24] R. Würschum, M. Rollinger, H. Kisker, A. Raichle, B. Damson, and H.-E. Schaefer, *Nanostruct. Mater.* **6**, 377, (1995)
- [25] P.P. Chattopadhyay, P.M.G. Nambissan, S.K. Pabi, and I. Manna, *Phys. Rev. B* **63**, 05107, (2001)
- [26] D. Sanyal, T. K. Roy, M. Chakrabarti, S. Dechoudhury, D. Bhowmick, and A. Chakrabarti, *J. Phys.: Condens. Matter* **20**, 045217, (2008)

-
- [27] J. Cizek, I. Prochazka, M. Cieslar, R. Kuzel, J. Kuriplach, F. Chmelik, I. Stulikova, F. Becvar, O. Melikhova, and R.K. Islamgaliev, *Phys. Rev. B* **65**, 094106, (2002)
- [28] J. Cizek, I. Prochazka, M. Cieslar, F. Chmelik, I. Stulikova, and R.K. Islamgaliev, *Phys. Stat. Sol.* **191**, 391, (2002)
- [29] S. Van Petegem, F. Dalla Torre, D. Seegers, and H. van Swygenhoven, *Scripta Mater.* **48**, 17, (2003)
- [30] R. Krause-Rehberg, V. Bondarenko, E. Thiele, R. Klemm, and N. Schell, *Nucl. Instr. Meth. Phys. Res. B* **240**, 719, (2005)
- [31] I. Prochazka, J. Cizek, R. Kuzel, Z. Matei, M. Cieslar, G. Brauer, W. Anwand, and R.K. Islamgaliev, in: *NANOCON 2009 Conference Proceedings*, 45, (2009)
- [32] M. Murayama, Z. Horita, and K. Hono, *Acta Mater.* **49**, 21, (2001)
- [33] H. Wang, Y.-I. Jang, B. Huang, D.R. Sadoway, and Y.-M. Chiang, *J. Electrochem. Soc.* **146**, 473, (1999)
- [34] H. Gabrisch, R. Yazami, and B. Fultz, *J. Electrochem. Soc.* **151**, A891, (2004)
- [35] J.R. Wilson, J.S. Cronin, S.A. Barnett, and S.J. Harris, *J. Power Sources* **196**, 3443, (2011)
- [36] Y. Shao-Horn, L. Croguennec, C. Delmas, E.C. Nelson, and M.A. O'Keefe, *Nature Materials* **2**, 464, (2003)
- [37] C. Wolverton and A. Zunger, *Phys. Rev. B* **57**, 2242, (1998)
- [38] A. Van der Ven, M.K. Aydinol, and G. Ceder, *Phys. Rev. B* **58**, 2975, (1998)
- [39] J. Molenda, A. Stoklosa, and T. Bak, *Solid State Ionics* **36**, 53, (1989)
- [40] M. Shibuya, T. Nishina, T. Matsue, and I. Uchida, *J. Electrochem. Soc.* **143**, 3157, (1996)
- [41] N. Balke, S. Jesse, A.N. Morozovska, E. Eliseev, D.W. Chung, Y. Kim, L. Adamczyk, R.E. Garcia, N. Dudney, and S.V. Kalinin, *Nature Nanotechnology* **5**, 749, (2010)
- [42] K. Nakamura, H. Ohno, K. Okamura, Y. Michihiro, I. Nakabayashi, T. Kanashiro, *Solid State Ionics* **135**, 143, (2000)

- [43] A. Van der Ven, G. Ceder, *J. Power Sources* **97-98**, 529, (2001)
- [44] Z. Chen and J.R. Dahn, *Electrochimica Acta* **49**, 1079, (2004)
- [45] J. Cho, Y.J. Kim, and B. Park, *J. Electrochem. Soc.* **146**, A1110, (2001)
- [46] Y.J. Kim, J. Cho, T.-J. Kim, and B. Park, *J. Electrochem. Soc.* **150**, A1723, (2003)
- [47] Y.I. Jang, B. Huang, H. Wang, D.R. Sadoway, G. Ceder, Y.-M. Chiang, H. Liu, and H. Tanamura, *J. Electrochem. Soc.* **146**, 862, (1999)
- [48] A. Rougier, I. Saadoune, P. Gravereau, P. Willmann, and C. Delmas, *Solid State Ionics* **90**, 63, (1996)
- [49] I.K. MacKenzie, T.L. Khoo, A.B. McDonald, and B.T.A. McKee, *Phys. Rev. Lett.* **19**, 946, (1967)
- [50] P. Hautojärvi and A. Vehanen, in: *Topics in Current Physics: Positrons in Solids*, Editor: P. Hautojärvi, Springer-Verlag, Berlin, (1979)
- [51] P.J. Schultz and K.G. Lynn, *Rev. Mod. Phys.* **60**, 701, (1988)
- [52] M.J. Puska and R.M. Nieminen, *Rev. Mod. Phys.* **66**, 841, (1994)
- [53] W. Brandt and R. Paulin, *Phys. Rev. B* **15**, 2511, (1977)
- [54] R.N. West, *Adv. Phys.* **22**, 263, (1973)
- [55] M.J. Puska and R.M. Nieminen, *J. Phys. F: Met. Phys.* **13**, 333, (1983)
- [56] A. Seeger in: *Positron annihilation*, Editors: L. Dorikens-Vanpraet, M. Dorikens and D. Seegers, World Scientific Publishing Co. Pte. Ltd., p.275, (1988)
- [57] G.P. Karwasz, A. Zecca, R. S. Brusa, and D. Pliszka, *J. Alloys and Compounds* **382**, 244, (2004)
- [58] A. Seeger, *J. Phys. F: Metal Phys.* **3**, 248, (1973)
- [59] A. Seeger, *Appl. Phys.* **4**, 183, (1974)
- [60] R.N. West, in: *Positron in solids*, Ed. P. Hautojärvi, p.89, Springer, Berlin, (1979)
- [61] H.-E. Schaefer, *phys. stat. sol. (a)* **102**, 47, (1987)
- [62] B. Oberdorfer and R. Würschum, *Phys. Rev. B* **79**, 184103, (2009)

-
- [63] R. Würschum, Struktur und Diffusionseigenschaften nanokristalliner Metalle, Habilitaionsschrift, Fakultät Physik, Universität Stuttgart, (1997)
- [64] W. Puff, Comput. Phys. Commun. **30**, 359, (1983)
- [65] J.M. Campillo Robles and F. Plazaola, Defect and Diffusion Forum **213-215**, 141, (2003)
- [66] N. Djourellov and M. Misheva, J. Phys.: Condens. Matter **8**, 2081, (1996)
- [67] S. McGuire and D.J. Keeble, J. Appl. Phys. **100**, 103504, (2006)
- [68] W. Puff, P. Mascher, P. Kindl, and H. Sormann, phys. stat. sol. (b) **118**, 799, (1983)
- [69] C. Hidalgo, G. Gonzalez-Doncel, S. Linderoth, and J. San Juan, Phys. Rev. B **45**, 7017, (1992)
- [70] O. Melikhova, J. Kuriplach, J. Cizek, and I. Prochazka, Appl. Surf. Sci. **252**, 3285, (2006)
- [71] K.G. Lynn, J.R. MacDonald, and E. Bonderup, Phys. Rev. Lett. **38**, 241, (1977)
- [72] A. Somoza, M. P. Petkov, K. G. Lynn and A. Dupasquier, Phys. Rev. B **65**, 094107, (2002)
- [73] A. Calloni, A. Dupasquier, R. Ferragut, P. Folegatti, M.M. Iglesias, I. Makkonen, and M.J. Puska, Phys. Rev. B **72**, 054112 (2005)
- [74] R.Z. Valiev, M.J. Zehetbauer, Y. Estrin, H.W. Hüpel, Y. Ivanisenko, H. Hahn, G. Wilde, H.J. Roven, X. Sauvage, and T.G. Langdon, Adv. Eng. Mater. **9**, 527, (2007)
- [75] M.J. Zehetbauer and Y.T. Zhu, Bulk Nanostructured Materials, Wiley-VCH, Weinheim, 2009
- [76] R.Z. Valiev, R.K. Islamgaliev, and I.V. Alexandrov, Prog. in Mater. Sci. **45**, 103, (2000)
- [77] A. Bachmaier and R. Pippan, Materials Science and Engeneering A, **528**, 7589, (2011)
- [78] J.B. Goodenough, M.M. Thackeray, W. David, and P.G. Bruce, Rev. Chim. Miner.

- 231**, 435, (1984)
- [79] Handbook of Battery Materials, Ed.: J.O. Besenhard, Wiley-VCH, Weinheim, (1999)
- [80] J. Rodriguez-Carval, Physica B 192, **55**, (1992)
- [81] J. Rodriguez-Carval, recent Developements of the Program FULLPROF, in Comission on Powder Diffraction (IUCr), Newsletter **26**, 12, (2001)
- [82] C.C. Koch, Nanostructured Materials: Processing, Properties and Applications (New York: Andrews Appl. Sci. Publ.), (2007)
- [83] M.J. Zehetbauer, R.Z. Valiev (Eds.), Nanomaterials by Severe Plastic Deformation, Wiley-VCH, Weinheim, (2004)
- [84] R. Pippan, F. Wetscher, M. Hafok, A. Vorhauer, and I. Sabirov, Adv. Eng. Mater. **8**, 1046, (2006)
- [85] A.P. Zhilyaev, B.K. Kim, J.A. Szpunar, M.D. Baro, and T.G. Langdon, Mater. Sci. Eng. A **391**, 377, (2005)
- [86] B. Oberdorfer, PhD. Thesis, Graz University of Technology, 2012
- [87] B. Scherwitzl, Diploma Thesis, Graz University of Technology, 2012
- [88] X. Zhou, Diploma Thesis, Graz University of Technology, 2011
- [89] W. Puff, X. Zhou, B. Oberdorfer, B. Scherwitzl, P. Parz, W. Sprengel, and R. Würschum, Physics Procedia, (accepted)
- [90] P. Hautojärvi, J. Johansson, A. Vehanen, and J. Yli-Kaupilla, Phys. Rev. Lett. **44**, 1326, (1980)
- [91] A. Vehanen, P. Hautojärvi, J. Johansson, J. Yli-Kaupilla, and P. Moser, Phys. Rev. B **25**, 762, (1982)
- [92] H.-E. Schaefer and R. Würschum, Phys. Lett. A **119**, 370, (1987)
- [93] H.F.M. Mohamed, J. Kwon, Y.-M. Kim, and W. Kim, Nucl. Inst. and Meth. in Physics Research B **258**, 429, (2007)
- [94] M. Eldrup and B.N. Singh, J. Nuc. Mater. **276**, 269, (2000)

-
- [95] J. Kuriplach, O. Melikhova, M. Hou, S. Van Petegem, E. Zhurkin, and M. Sob, *phys. stat. sol. (c)* **4**, 3461, (2007)
- [96] J. Kuriplach, O. Melikhova, M. Hou, S. Van Petegem, E. Zhurkin, and M. Sob, *Appl. Surf. Sci.* **255**, 128, (2008)
- [97] A. Hohenwarter, C. Kammerhofer, and R. Pippan, *J. Mater. Sci.* **45**, 4805, (2010)
- [98] R.M. Nieminen and J. Laakkonen, *Appl. Phys.* **20**, 181, (1979)
- [99] F. Wetscher, A. Vorhauer, and R. Pippan, *Mater. Sci. Eng. A* **410-411**, 213, (2005)
- [100] H.E. Schaefer, R. Würschum, R. Birringer and H. Gleiter, *Phys. Rev. B* **38**, 9545, (1988)
- [101] Y. Kamimura, T. Tsutsumi, and E. Kuramoto, *Phys. Rev. B* **52**, 879, (1995)
- [102] R. Würschum, A. Seeger, *Phil. Mag. A* **73**, 1489, (1996)
- [103] A. Dupasquier, R. Romero and A. Somoza, *Phys. Rev. B* **48**, 9235, (1993)
- [104] P. Parz, M.Faller, R. Pippan, W. Puff, and R. Würschum, *Physics Procedia* **35**, 10, (2012)
- [105] P. Parz, M.Faller, R. Pippan, H. Reingruber, W. Puff, and R. Würschum, *J. Appl. Phys.* **112**, 103506, (2012)
- [106] G. Gottstein, *Physikalische Grundlagen der Materialkunde*, Springer Verlag Berlin-Heidelberg
- [107] A. Vorhauer and R. Pippan, *Metallurgical and materials transactions A* **39A**, 417, (2008)
- [108] M. Faller, *Diploma Thesis, Montanuniversitaet Leoben, Leoben*, (2010)
- [109] R.W. Cahn and P. Haasen, *Physical Metallurgy Vol. 2*, North-Holland, Amsterdam, (1996)
- [110] P. Folegati, M. J. Puska, and T. E. M. Staab, *J. of Physics: Conference Series* **265**, 021017, (2011)
- [111] A. Somoza, and A. Dupasquier, *J. Materials Processing Technology* 135, **83**,

- (2003)
- [112] H.-E. Schaefer, R. Gugelmeier, M. Schmolz, and A. Seeger, *Mater. Sci. Forum* **15-18**, 111, (1987)
- [113] J.A. Jackman, G.M. Hood, and R.J. Schultz, *J. Phys. F: Met. Phys.* **17**, 1817, (1987)
- [114] R.K.W. Marceau, G. Sha, R. Ferragut, A. Dupasquier, and S.P. Ringer, *Acta Mater.* **58**, 4923, (2010)
- [115] R.M.J. Cotterill, K. Petersen, G. Trumpy and J. Träff, *J. Phys. F: Metal Phys.* **2**, 459, (1972)
- [116] T.E.M. Staab, B. Klobes, I. Kohlbach, B. Korff, M. Haaks, E. Dudzik, and K. Maier, *J. Physics: Conference series* **265**, 012018, (2011)
- [117] U.H. Gläser, G. Dlubek, and R. Krause, *phys. stat. sol. (b)* **163**, 337, (1991)
- [118] P. Folegati, I. Makkonen, R. Ferragut, and M. J. Puska, *Phys. Rev. B* **75**, 054201 (2007)
- [119] R. Ferragut, G. Ferro, M. Biasini, A. Dupasquier, and A. Somoza, *Mater. Sci. Forum* **445-446**, 75, (2004)
- [120] G. Dlubek, P. Lademann, H. Krause, S. Krause and R. Unger, *Scr. Mater.* **39**, 893, (1998)
- [121] O. Melikhova, J. Cizek, I. Prochazka, J. Kuriplach, I. Stulikova and J. Faltus, *Materials Structure* **8**, 61, (2001)
- [122] W. Lechner, PhD Thesis, Graz University of Technology, (2009)
- [123] H. Häkkinen, S. Mäkinen, and M. Manninen, *Phys. Rev. B* **41**, 12441, (1990)
- [124] R. Ferragut, G. Ferro, and M. Biasini, *Materials Forum* **28**, 1022, (2004)
- [125] K. Petersen, I.A. Repin, and G. Trumpy, *J. Phys.: Condens. Matter* **8**, 2815, (1996)
- [126] Y. Nagai, M. Murayama, Z. Tang, T. Nonaka, K. Hono, and M. Hasegawa, *Acta Mater.* **49**, 913, (2001)

-
- [127] R. Krause-Rehberg, H.S. Leipner, A. Kupsch, A. Polity, and Th. Drost, *Phys. Rev. B* **49**, 2358, (1994)
- [128] M.J. Puska, P. Lanki, and R.M. Nieminen, *J. Phys.: Condens. Matter* **1**, 6081,(1989)
- [129] L.H. Su, C. Lu, L.Z. He, L.C. Zhang, P. Guagliardo, A.K. Tieu, S.N. Samarin, J.F. Williams, and H.J. Li, *Acta Mater.* **60**, 4218, (2012)
- [130] J. Cizek, M. Janeck, O. Srba, R. Kuzel, Z. Barnovska, I. Prochazka, and S. Dobatkin, *Acta Mater.* **59**, 2322, (2011)
- [131] M. Weller and U.G.K. Wegst, *Mat. Sci. And Eng. A* **41**, 521, (2009)
- [132] P. Parz, M. Leitner, W. Sprengel, H. Reingruber, and W. Puff, *Physics Procedia*, (accepted, February 2013)
- [133] M. Leitner, Bakkelauriatsarbeit, Graz University of Technology, (2012)
- [134] A.E. Moren and J.I. Goldstein, *Earth and Planetary Science Letters* **40**, 151, (1978)
- [135] Y. He, S. Godet, P.J. Jacques, and J.J. Jonas, *Acta Mater.* **54**, 1323, (2006)
- [136] R.S.Jr. Clarke and E.R.D. Scott, *Am. Mineral.* **65**, 624, (1980)
- [137] L.J. Swartzendruber, V.P. Itkin and C.B. Alcock, in: "Phase Diagrams of Binary Iron Alloys", Okamoto H (ed.), Materials Information Soc., Materials Park, Ohio, (1993)
- [138] J. Cermak, M. L bbhusen and M. Mehrer, *Z. Metallkde.* **880**, 213, (1989)
- [139] M.M. Nowell and O. Carpenter, *Microscopy Today*, p.6-10, Sept. 2007
- [140] Y. Shirai, H.-E. Schaefer, A. Seeger, in: *Positron Annihilation*, World Scientific Publ. Co., Singapore, p.419, (1988)
- [141] P. Parz, B. Fuchsbichler, S. Koller, B. Bitschnau, F.A. Mautner, W. Puff, and R. W rschum, *Appl. Phys. Lett.* **102**, 151901,(2013)
- [142] H.F. Gibbard, *J. Power Sources* **26**, 81, (1989)
- [143] A. Senyshyn, M.J. M hlbauer, K. Nikolowski, T. Pirling, and H. Ehrenberg,

- J. Power Sources **203**, 126, (2012)
- [144] T.E.M. Staab, R. Krause-Rehberg, and B. Kieback, J. Materials Science **34**, 3833, (1999)
- [145] M. Forster, J.N. Mundy, and H.-E Schaefer, in: Positron Annihilation, Editors: L. Dorikens-Vanpraet, M. Dorikens and D. Seegers, World Scientific Publishing Co. Pte. Ltd., p.833, (1988)
- [146] A.A. Valeeva, A.A. Rempel, W. Sprengel, and H.-E. Schaefer, Phys. Rev. B **75**, 094107, (2007)
- [147] Q. Zhang and R.E. White, J. Electrochem. Soc. **154**, A587, (2007)
- [148] M.J. Puska, in: Positron annihilation, Editors: L. Dorikens-Vanpraet, M. Dorikens and D. Seegers, World Scientific Publishing Co. Pte. Ltd., p.101, (1988)
- [149] J. Mäkinen, C. Corbel, P. Hautojärvi, P. Moser, and F. Pierre, Phys. Rev. B **39**, 10162, (1989)
- [150] Y. Shao-Horn, S. Levasseur, F. Weill, and C. Delmas, J. Electrochem. Soc. **150**, A366, (2003)
- [151] J.N. Reimers, J.R. Dahn, and U. von Sacken, J. Electrochem. Soc. **140**, 2752, (1993)
- [152] S. Brunner, W. Puff, A.G. Balogh, and P. Mascher, Mater. Sci. Forum **141**, 363, (2001)
- [153] A. Van der Ven and G. Ceder, Electrochem. and Solid-State Letters **3**, 301, (2000)
- [154] D. Guyomard and J.M. Tarascon, J. Electrochem. Soc. **139**, 937, (1992)
- [155] A. Van der Ven, C. Marianetti, D. Morgan, and G. Ceder, Solid State Ionics **135**, 21, (2000)
- [156] J.B. Goodenough, M.M. Thackeray, W.I.F. David, and P. G. Bruce, Revue de Chimie Minerale **21**, 435, (1984)
- [157] M.M. Thackeray, Prog. Solid St. Chem. **25**, 1-71, (1997)
- [158] K. Momma and F. Izumi, J. Appl. Crystallogr. **44**, 1272, (2011)

- [159] J.W. Fergus, *J. Power Sources* **195**, 939, (2010)
- [160] F. Rosciano, J.-F. Colin, F. La Mantia, N. Tran, and P. Novak, *Electrochem. and Solid-State Lett.* **12**, A140, (2009)
- [161] D.D. MacNeil, Z. Lu, and J.R. Dahn, *J. Electrochem. Soc.* **149**, A1332, (2002)
- [162] M.E. Arroyo y de Dompablo, C. Marianetti, A. Van der Ven, and G. Ceder, *Phys. Rev. B* **63**, 144107, (2001)
- [163] J. Li, Z. R. Zhang, X. J. Guo, and Y. Yang, *Solid State Ionics* **177**, 1509, (2006)
- [164] C. Delmas, J.P. Peres, A. Rougier, A. Demourgues, F. Will, A. Chadwick, M. Broussley, F. Peron, Ph. Biensan, and P. Willmann, *J. Power Sources* **68**, 120, (1997)

Danksagung

Die vorliegende Arbeit entstand in den Jahren 2009-2013 während meiner Tätigkeit als Universitäts Assistent am Institut für Materialphysik der Technischen Universität Graz. Sie wäre nicht möglich gewesen ohne die Unterstützung der folgenden Personen:

An erster Stelle möchte ich mich bei meinem Doktorvater, Herrn Ao. Univ.-Prof. Dr. Werner Puff, für die Vergabe und Betreuung der Dissertation, sowie für das entgegengebrachte Vertrauen in meine Arbeit bedanken.

Des Weiteren möchte ich mich bei Ao. Univ.-Prof. Dr. Michael Zehetbauer für die Begutachtung meiner Dissertation bedanken.

Besonderer Dank gilt Herrn Univ.-Prof. Dr. Roland Würschum, für die anregenden Diskussionen und die Schaffung der Möglichkeit zur Dissertation am Institut für Materialphysik.

Für die vielschichtigen Diskussionen, Hinweise und Tipps, sowohl in fachlichen als auch nicht fachlichen Dingen möchte ich mich herzlich bei Herrn Dr. Wolfgang Sprengel bedanken.

Mein Dank gilt auch der Arbeitsgruppe von Herrn Prof. Dr. Reinhard Pippan vom Erich Schmid Institut für Materialwissenschaften in Leoben, für die Herstellung der stark plastisch verformten Proben.

Bei der Arbeitsgruppe von Herrn Dr. Stefan Koller von VARTA Microinnovations, sowie Herrn Dr. Bernd Fuchsbichler und Herrn Christian Baumann möchte ich mich für die unbürokratische Herstellung und Delithierung der Lithium-Ionen-Elektroden bedanken.

Für das angenehme Arbeitsklima am Institut, die anregenden Diskussionen und erfrischenden Kaffeepausen möchte ich mich bei Herrn Dr. Ulrich Brossmann, Herrn Dipl.-Ing. Stefan Topolovec, Frau Dipl.-Ing. Eva-Maria Steyskal, Herrn Dr. Bernd Oberdorfer, Herrn Dipl.-Ing. Martin Luckabauer sowie den Herrn Jaromir Kozurek und Bernhard Nell bedanken.

Außerordentlicher Dank für die Unterstützung in Verwaltungsbelangen gilt Frau Regina Steingasser und Frau Eva Kniewasser für die unermüdliche Unterstützung in Werkstatt und Labor.

Bedanken möchte ich mich auch bei Herrn Dipl.-Ing. Xiang Zhou für die gute wissenschaftliche Arbeit während seiner Diplomarbeit sowie für die gute Zusammenarbeit im Rahmen ihrer Bakkalaureatsarbeiten bei Frau Katrin Koren und Herrn Matthias Leitner.

Zum Schluss möchte ich mich noch bei allen Personen bedanken, die mich unterstützt und aufgebaut haben als ich selbst am Gelingen dieser Arbeit gezweifelt habe.